ABSTRACT

Title of thesis: SIZING TOOL
FOR QUADROTOR BIPLANE TAILSITTER UAS

Eric Strom, Master of Science, 2017

Thesis directed by: Dr. James D. Baeder
Department of Aerospace Engineering

The Quadrotor-Biplane-Tailsitter (QBT) configuration is the basis for a mechanically simplistic rotorcraft capable of both long-range, high-speed cruise as well as hovering flight. This work presents the development and validation of a set of preliminary design tools built specifically for this aircraft to enable its further development, including: a QBT weight model, preliminary sizing framework, and vehicle analysis tools. The preliminary sizing tool presented here shows the advantage afforded by QBT designs in missions with aggressive cruise requirements, such as offshore wind turbine inspections, wherein transition from a quadcopter configuration to a QBT allows for a 5:1 trade of battery weight for wing weight. A 3D, unsteady panel method utilizing a nonlinear implementation of the Kutta-Joukowsky condition is also presented as a means of computing aerodynamic interference effects and, through the implementation of rotor, body, and wing geometry generators, is prepared for coupling with a comprehensive rotor analysis package.

PERFORMANCE AND SIZING TOOL FOR QUADROTOR BIPLANE TAILSITTER UAS

by

Eric Strom

Thesis submitted to the Faculty of the Graduate School of the
University of Maryland, College Park in partial fulfillment
of the requirements for the degree of
Master of Science
2017

Advisory Committee:
Dr. James Baeder, Chair/Advisor
Dr. Inderjit Chopra
Dr. Anubhav Datta

Dedication

To Jesus Christ and the work of making His Name known and loved.

Acknowledgments

I would be remiss if I did not pause at the start of this thesis to thank those without whom it would either be left unfinished, or finished at the expense of my own well-being.

First, I would like to thank my Franciscan community, the friars of the Third Order Regular of St. Francis of Assisi of Penance, Province of the Most Sacred Heart of Jesus: particularly those who have lived with me these past few years at St. Louis Friary. Thank you for your continual reminders that it is not a bad thing to take breaks, that it is nice to do things with me, for the encouragement to persevere in prayer, and the reminders to unite my studies and my prayer. I cannot thank you enough.

Similarly, to my parents and grandparents. Thank you for your encouragement (baked as well as verbal), phone conversations during the commute to and from school, passing along greetings from Nessie, and, especially from my father, last-minute help with debugging. It means more to me than I can express.

Also, to those who have worked with me at the University of Maryland, especially those who have been in Dr. Baeder's lab these past few years: Nishan, Steven, Dylan, Bumsoek, Atif, Andrew, Kaney, Vera, Yong Su, Seung Joon, Alex, Matthew, Jonathan, Kilian, Camli, and, last but definitely not least, Bharath. Thank you for the technical help, the conversations that kept me a (little) more sane, and the humor that you bring to the lab. My one regret from my time here is that I did not spend more time with you all. This would also be lacking if I failed to note the

same of all the students I have met over the last few years, but especially those I met during Helicopter Design. To date, that is the hardest class I have ever taken, but I daresay the most fruitful in terms of technical skills as well as relationships. It is been a blessing to know you all, even if it did cost us too many nights without sleep.

Finally, a thank you to Dr. James Baeder who single-handedly enabled this endeavor through his generosity and insight. I was not sure where grad school would take me, and it has turned out better than I could have dreamed. Thank you for enlisting me for this project, and I hope and pray that I have the chance to work with you again.

Table of Contents

List of Tables

List of Figures

List of Abbreviations

CTV	Crew Transfer Vehicle
EO	Electro-Optical
EW	Empty Weight
FAA	Federal Aviation Administration
GTOW	Gross Takeoff Weight
IR	Infrared
ISA	International Standard Atmosphere
LIDAR	Light Detection and Ranging
LiPo	Lithium Polymer
MAC	Mean Aerodynamic Chord
Metocean	Meteorological and oceanic
NREL	National Renewable Energy Laboratory
O&M	Operations and Maintenance
PrasadUM	Parallelized Rotorcraft Analysis for Simulation and Design University of Maryland
QBT	Quadrotor-Biplane-Tailsitter
SODAR	Sonic Detection and Ranging
UAS	Unmanned Aircraft System
UMD	University of Maryland
TURNS2D	Transonic Unsteady Rotor Navier-Stokes 2D

Chapter 1: Introduction

1.1 Motivation: Needs of the Offshore Wind Energy Industry

As of September of 2015 the offshore wind industry has installed 8,990 MW of energy production capacity and over 1,600 turbines worldwide, and its demonstrated efficacy has placed offshore wind farms in the spotlight for many nations as they seek to grow their renewable energy portfolios. While countries like Denmark and the United Kingdom are at the forefront of offshore wind development in the West, the Asian market is significant, seeing aggressive development of offshore wind resources by countries such as China and Japan. In the United States, the Department of Energy set a goal in 2015 for the nation to derive 35% of its electricity from wind power by 2050, a vision that requires 86 GW of installed offshore wind power generation capacity. As the time of writing, the US has completed a total of a 30 MW of installed offshore wind power production capacity (0.03% of the goal) in the form of a 5 turbine farm off the coast of Rhode Island. However, as shown in Figure 1.1, this is only the beginning of the offshore wind industry in the US as there is over 20 GW of additional capacity in various levels of planning. This mammoth industrial expansion requires support from a variety of industries and their nascent (or non-existent) supply chains, including: large-scale offshore construction, shipbuilding,

large-scale steel fabrication, large-scale composites manufacturing, and others.

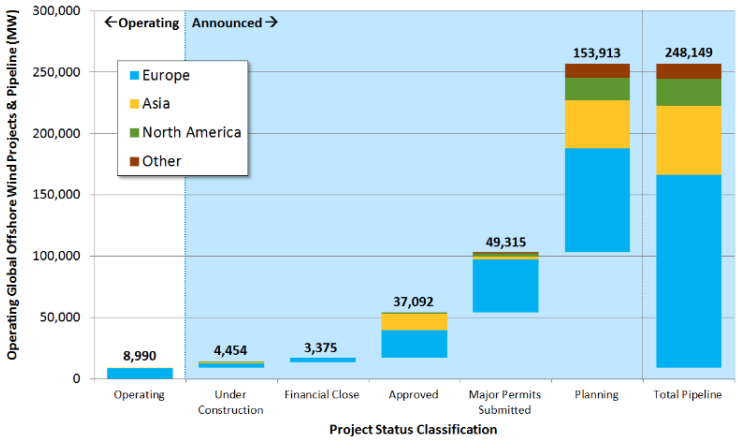

Figure 1.1: Worldwide offshore wind development pipeline [1]

Furthermore, there is the issue of cost. For example, the United States Energy Information Administration [14] estimates that, when considering the levelized cost of energy for powerplants entering service in the United States by 2022, offshore wind power will cost \$145.90/MWh (including levelized tax credit). This is over 2 times that of onshore wind plants entering service in a comparable time frame (\$63.70/MWh, not including levelized tax credit of \$11.60/MWh) or conventional combined cycle gas-fired plants (\$56.50/MWh, with no applicable tax credits). To aid wind plants in becoming competitive, state and national governments both at home and abroad have typically offered wind developers various subsidies in an effort to enable the industry's growth where it might not be competitive. In addition, the American, English, and Danish governments have adopted various policies that both encourage competition between wind project developers and de-risk the project planning process. These include the practices of developing detailed meteorological predictions and histories for potential project locations as well as opening

competitive auctions of power generation subsidies as discussed by Smith et. al. [1]. However, while these policies do impact various capital and operational expenditures, they do not address the underlying issues that contribute to them.

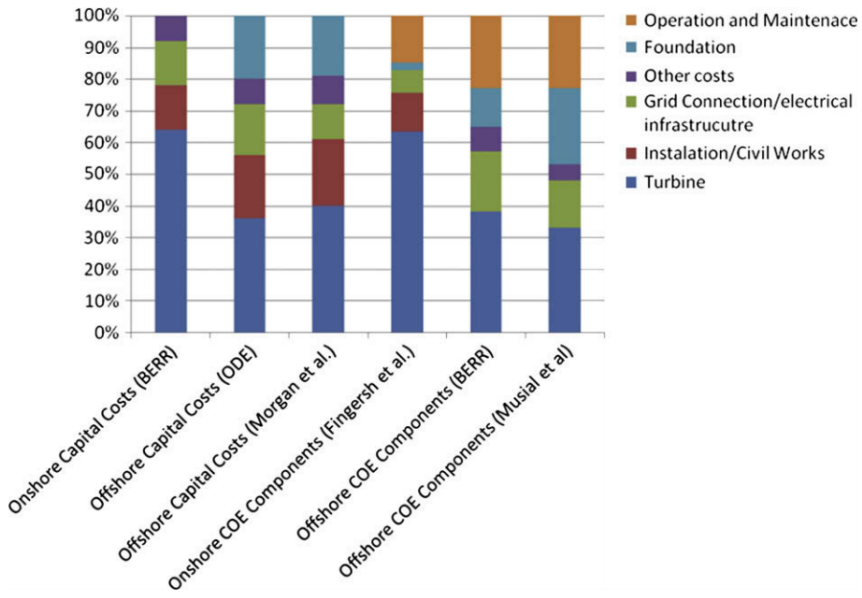

Figure 1.2: Offshore wing cost of energy breakdown [1]

As part of an effort to better describe these issues, the National Renewable Energy Laboratory (NREL) [15] published an assessment of the opportunities for and barriers to the development of offshore wind power in the United States. In this report, Musial and Ram note that costs related to operations and maintenance (O&M) account for 20-33% of an offshore wind project's total expenses. As seen in Figure 1.2, this has not been the case for onshore wind power, where O&M-related expenses are nearly 10% less than those for offshore projects. Whereas component failure rates, failure costs, and required turbine downtime during repairs exacerbate these costs, as detailed by Carroll et. al. [2] and Shafiee et. al. [16], Dinwoodie and McMillan [17] also demonstrate how turbine accessibility, and thus meteorological

and oceanic (henceforth referred to collectively as "metocean") conditions, can also have a significant impact on expenses related to turbine O&M. Since turbines are naturally sited in locations conducive to power generation, locations which are associated with extreme metocean conditions, thus restricting regular surface travel to available "weather windows," this places a premium on component reliability and maintenance strategy. This has been demonstrated in studies by Lei et. al. [18] as well as Sarker and Fiaz [19].

This question of accessibility is the subject of a variety of studies on the relative costs of preventive and corrective maintenance strategies. An opportunistic strategy, such as developed by Sarker and Fiaz [19], capitalizes on turbine accessibility windows typically used to perform necessary corrective maintenance in order to perform preventative maintenance instead. However, other models focus on developing failure predictions and opportunistic maintenance schedules that leverage the same windows more specifically and effectively. These predictive maintenance strategies, such as those being developed by Lei et. al. [18] and Shafiee et. al. [16], capitalize on condition-based monitoring techniques, such as those described by Kandukuri et. al. [20] and Takoutsing et. al. [21], in order to predict the remaining useful life of the turbine or turbine component such that maintenance missions can be planned before a failure occurs. However, both Takoutsing et. al. and Kanukuri et. al. note that, despite the significant advantages of these various condition-based monitoring (CBM) techniques, they are still under development and require a significant investment to implement.

1.1.1 Maintenance Drivers and Inspection Methodology

In addition to accessibility issues, there are also certain components that, in particular, drive these expenses. As noted in a study of about 350 offshore wind turbines by Carroll et. al. [2], rotor blades require the most technicians per repair, the highest cost per repair, and boast the 5th highest failure rate of all of turbine components surveyed (as shown in Figure 1.3). The defects responsible for these failures are typically found by inspectors performing visual inspections. However, as previously noted, these inspections are frequently hampered by metocean conditions and the inability to access turbines on a consistent basis.

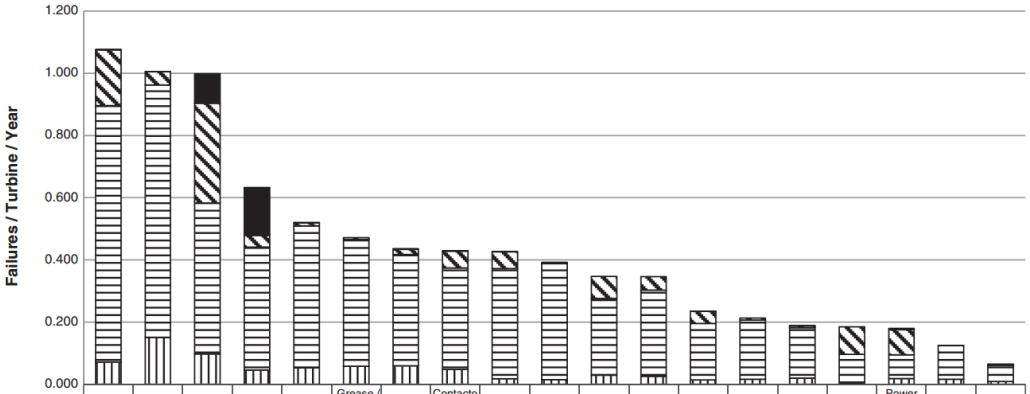

	Pitch / Hyd	Other Components	Generator	Gearbox	Blades	Grease / Oil / Cooling Liq.	Electrical Components	Contactor / Circuit Breaker / Relay	Controls	Safety	Sensors	Pumps/ Motors	Hub	Heaters / Coolers	Yaw System	Tower / Foundation	Power Supply / Converter	Service Items	Transformer
Major Replacement	0.001	0.001	0.095	0.154	0.001	0.000	0.002	0.002	0.001	0.000	0.000	0.000	0.001	0.000	0.001	0.000	0.005	0.000	0.001
Major Repair	0.179	0.042	0.321	0.038	0.010	0.006	0.016	0.054	0.054	0.004	0.070	0.043	0.038	0.007	0.006	0.089	0.081	0.001	0.003
Minor Repair	0.824	0.812	0.485	0.395	0.456	0.407	0.358	0.326	0.355	0.373	0.247	0.278	0.182	0.190	0.162	0.092	0.076	0.108	0.052
No Cost Data	0.072	0.150	0.098	0.046	0.053	0.058	0.059	0.048	0.018	0.015	0.029	0.025	0.014	0.016	0.020	0.004	0.018	0.016	0.009

Figure 1.3: Pareto chart of average component failure rate [2]

At present, methods of performing a rotor blade inspection (that are considered in this work) include manned access to each blade via (1) a roped descent from the turbine nacelle or (2) remote inspections facilitated by various short-range unmanned multicopters that can be carried within range of individual turbines by

boat. Other methods of inspection, such as an inspection from personnel on a CTV utilizing telephoto lenses or inspections from manned aircraft are also options, but cannot give the same perspective as a roped inspector on a blade or a UAS in close proximity to a blade, making these latter two methods the primary options for on-demand inspections. The operational paradigm reflected by each of methods considered in this work are depicted in Figure 1.4, where travel distances and weather requirements are drawn from an existing wind farm layout [22] and metocean conditions in the Maryland offshore wind energy area. These inspection methodologies

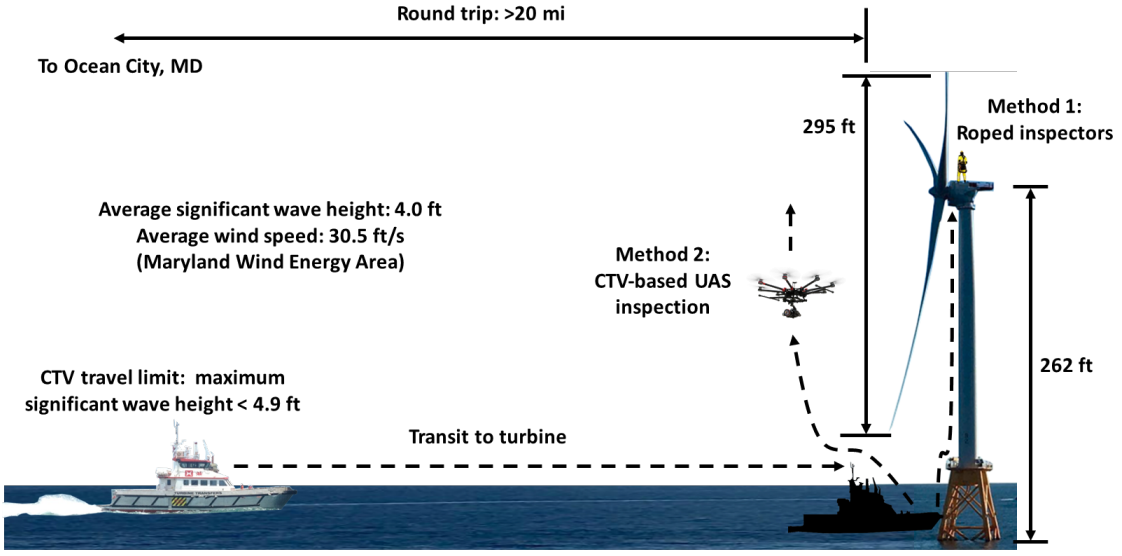

Figure 1.4: Inspection mission concepts requiring manned transportation to the turbine

are limited by their respective tolerances for metocean conditions. A representative value for these limitations has been drawn from publicly available specifications for various Unmanned Aerial Systems (UAS) used for turbine inspections or, in the case of the Crew Transfer Vehicles (CTVs) utilized for oversea transport, from Maples et. al. [23]. A summary of this is compiled in Table 1.1. These methods are dis-

cussed in more detail by Navigant Research [24], and various companies, including SkyProff [25], and DJI [26].

Table 1.1: Summary of inspection methods and limitations

Method	Inspection Time	Weather Limits
Roped inspector	3 hr	Waves < 4.9 ft
CTV-borne UAS	20 min	Waves < 4.9 ft Wind < 50 ft/s

It is worth noting that all of these methods carry with them significant costs, be they in terms of financial investment, risk to personnel, the time necessary to carry out the inspection, or the necessity for ample weather windows to actually be able to access the turbine. These weather windows, while predictable in the short term, are a significant limitation to turbine servicing due to seasonal variation in weather patterns. As shown in Figure 1.5, these seasonal variations can result in nearly 100% increases in average wind speed as well as dramatic variation in the direction of the prevailing wind. Wave height exhibits a similar trend, though it should be recognized that both trends will vary depending on the particular farm's location with respect to the local topography (e.g., islands, underwater obstacles, etc.) and weather patterns. Hence, predicting weather patterns and scheduling tasks for the available windows is key to any maintenance strategy.

Hence, to best take advantage of these windows, inspection missions should be expedited, insofar as is advisable, and decoupled, insofar as it is possible, from metocean conditions: a difficulty for manned, up-tower inspections. As noted by the owner of one inspection company [26], these missions require 3-4 hours per turbine

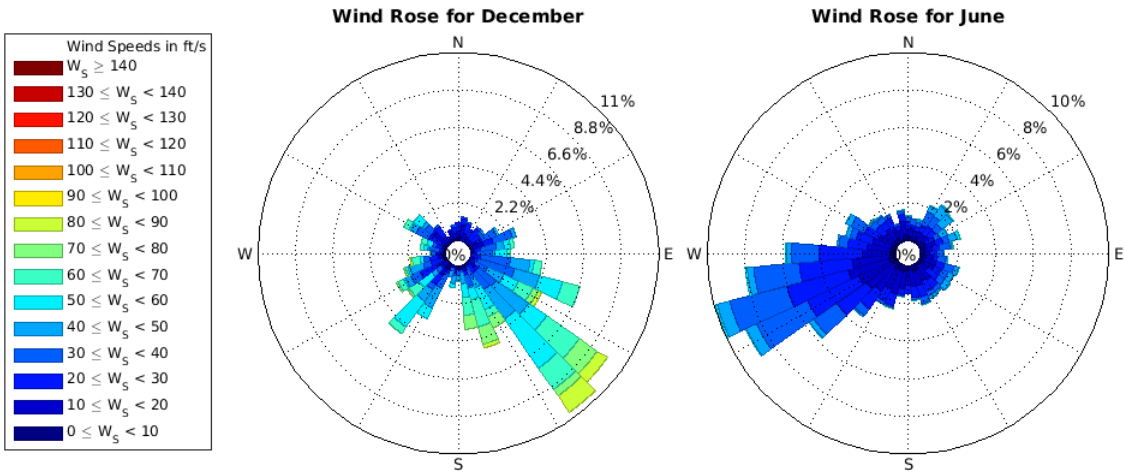

Figure 1.5: Probability distributions of wind speed and direction in the Maryland offshore wind energy area [3]

inspection, not including transport to the turbine by aircraft or water vessel. Hence, while the range and endurance of current UAS still requires them to use support vehicles for inter-farm transport, application of these aircraft to this mission has been shown to reduce the inspection time per turbine by over 75%. Also of significance is that, while a manned inspection incurs some amount of risk to persons in their transport to the turbine as well as during the roped inspection itself, these unmanned methods inherently reduce that risk. While it is true that UAS are not without risk, the hazard to human beings is substantially reduced by removing workers from hazardous environments and by operating the UAS in areas, such as a wind farm, that are inherently deserted.

(a) AscTec Falcon 8 [27]

(b) DJI inspire 1 [28]

(c) Aibot X6 [29]

(d) DJI S1000 [28]

Figure 1.6: Typical UAS currently used for on- and offshore wind turbine inspections

1.1.2 Offshore Wind Maintenance Inspections: Current UAS

UAS are currently employed to inspect wind turbines by various companies, including: Aibotix, Aeolus Energy Servicing, and Cyberhawk. A selection of the UAS employed by these companies are shown in Figure 1.6. These vehicles all share certain characteristics, including their use of distributed electric propulsion, a payload of electro-optical/infrared (EO/IR) sensors on a stabilized gimbal, hovering flight capabilities, and a simple control system, utilizing only differential thrust and torque to maneuver. Some basic specifications for these aircraft can be found in Table 1.2. While these are only a small sampling of the existing aircraft developed for this industry, it could be considered a representative sample of the UAS that have been adapted to or developed specifically for this role.

As quoted by Aibotix [29] and DJI [26], a UAS-driven inspection could require

Table 1.2: Selected multicopter UAS currently servicing wind turbines

Aircraft	GTOW	Payload	Max. Speed	Max. Endurance
AscTec Falcon 8 [30]	5.0 lbf	1.7 lbf	48.4 ft/s	22 min
DJI Inspire 1 [31]	7.7 lbf	1.4 lbf	71.8 ft/s	18 min
Aibot X6 [29]	14.5 lbf	4.4 lbf	36.6 ft/s	20 min
DJI S1000 [32]	22.2 lbf	15 lbf	52.5 ft/s	15 min

15-45 minutes of flight time, depending on the turbine: a reduction of over 75% from the time typically allotted for a roped inspector. However, while relatively fast in terms of inspection time, aircraft of this configuration also share some similar limitations. While each of the multicopter UAS shown can complete a typical inspection mission, they does not have the ability to prolong that mission and are inherently limited by the high winds typically found at offshore sites. As the inspection mission represents the majority, if not all, of the aircraft's flight endurance, these aircraft do not have the ability to fly directly to a turbine. Hence, for missions away from fixed operating bases, a manned support vehicle is necessary, which still ties the aircraft's use to oceanic conditions.

In addition to fulfilling the primary mission of turbine inspections (of blades, foundations [33], or other components), such it is also desirable to use an aerial platform for other missions of importance to the wind farm. For example, the ability to characterize turbine wakes (and thus the flow field within a farm) is vital to the wind farm operator as the turbulent wake trailed by turbines negatively impacts both the structural life and power production of downwind turbines. At present, this field is characterized by meteorological masts with fixed sensing elements, SODAR, or LIDAR. However, these methods are expensive and are limited in appli-

cation. However, in an effort to place similar or complementary capabilities onto a relatively inexpensive aerial platform the University of Bergen has undertaken to develop a fixed-wing UAS, also known as the Small Unmanned Meterological Observer (SUMO) [4, 34–36].

In particular, Båserud et. al. [35] characterized a sensor for measuring turbulence that could be transported by the SUMO, and, studies by Reuder et. al. [36], demonstrated the aircraft's ability to measure the turbulent kinetic energy and reduction in mean wind speed behind a row of onshore turbines operating above their rated wind speed (49-65 ft/s). When comparing this wind speed to the maximum speeds given in Table 1.2, this mission would not be possible for many multicopters currently available to the industry. An image of the SUMO, developed from a commercially available airframe and later modified with additional sensors, can be seen in Figure 1.7 (installed sensors are absent from this image).

Figure 1.7: SUMO aircraft developed by the University of Bergen and accompanying ground station [4]

1.1.3 A Novel UAS for Offshore Wind Turbine Inspection

Hence, to provide a long-range, high-speed, high-endurance UAS for offshore wind maintenance support missions, this study proposes the use of a vehicle configuration that has been independently developed at the University of Maryland (UMD): a quadrotor-biplane-tailsitter (QBT). This is a hover-capable UAS that far surpasses most, if not all, typical multirotor UAS designs in terms of range, endurance, and payload capacity while still retaining the simple control scheme and construction shared by typical multicopter UAS. Early wind tunnel experiments by Hrishikeshavan et. al. [37], considering a wing-propeller system in trimmed flight, indicated that this aircraft could enter high-speed cruising flight while utilizing only 1/3 of the power that is required for hovering flight. Further experimentation led the development of the aircraft shown in Figure 1.8.

(a) Proof of Concept (0.52 lbf) [38] (b) Prototype vehicle (7.98 lbf) [5]

Figure 1.8: Current examples of QBT aircraft designed at UMD

The lighter of the two aircraft, shown in Figure 1.8(a), was a proof of concept vehicle utilized by Hrishikeshavan et. al. [38]. The latter vehicle, shown in Figure 1.8(b), is an 8 lbf testbed developed by Phillips et. al. [5] and, at the time of writing,

is being used to further characterize the QBT configuration on a larger scale. An extract of the data from preliminary flight tests of this aircraft, given in Figure 1.9, shows the power required for sustained, level flight by the vehicle decreasing by 68% following transition from hovering to fixed-wing forward flight. While the full results of this test are preliminary in nature, this result indicates a first confirmation of hypotheses concerning the aircraft's potential for long-range, high-speed flight. This potential has also been demonstrated in two concepts designed at UMD for recent design competitions, including a package delivery UAS designed by Sidle et. al. [9] and a larger disaster relief aircraft designed by Trollinger et. al. [39].

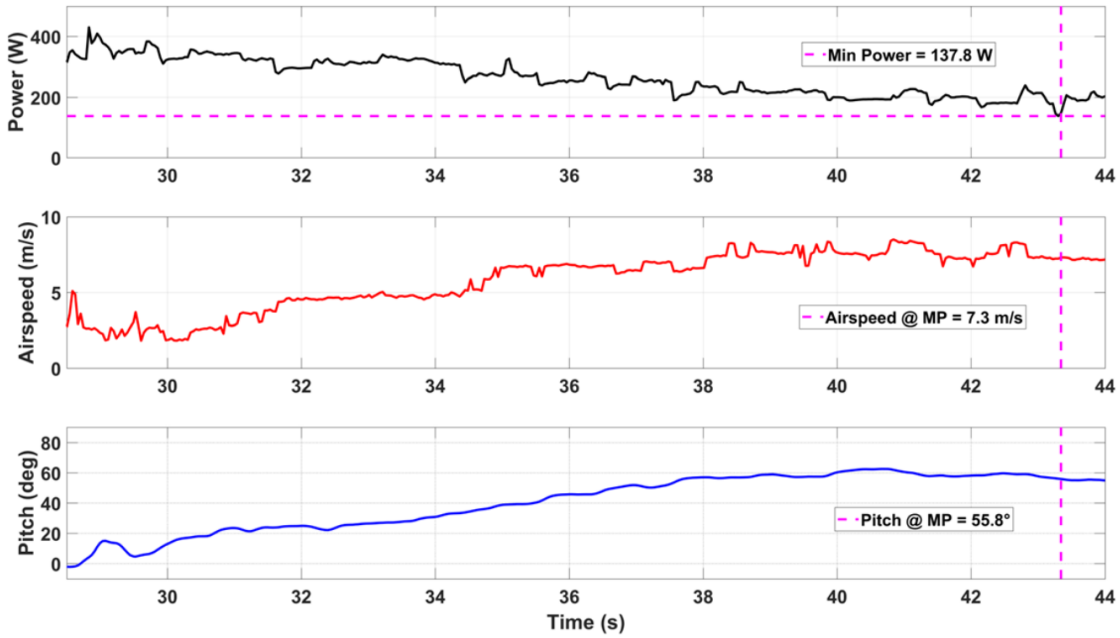

Figure 1.9: Detailed view of first transition to fixed wing flight with power, airspeed, and pitch indicated at time of minimum power [5]

However, the mission contemplated for this aircraft in an offshore wind farm would be more aggressive than that proposed for any QBT yet contemplated by design studies at UMD. This mission would require prolonged hovering and cruising

flight in high winds in excess of 75 ft/s in order to obviate the need for manned support vehicles. This concept of operations is illustrated in more detail in Figure 1.10 for the same metocean conditions and farm layout given in the previous operational concept for manned inspection missions, as illustrated in Figure 1.4. However, as the aircraft would not require human intervention to reach a given turbine, it could be stationed on the wind farm itself, providing a means for rapid, on-demand turbine inspections without incurring risk to human life.

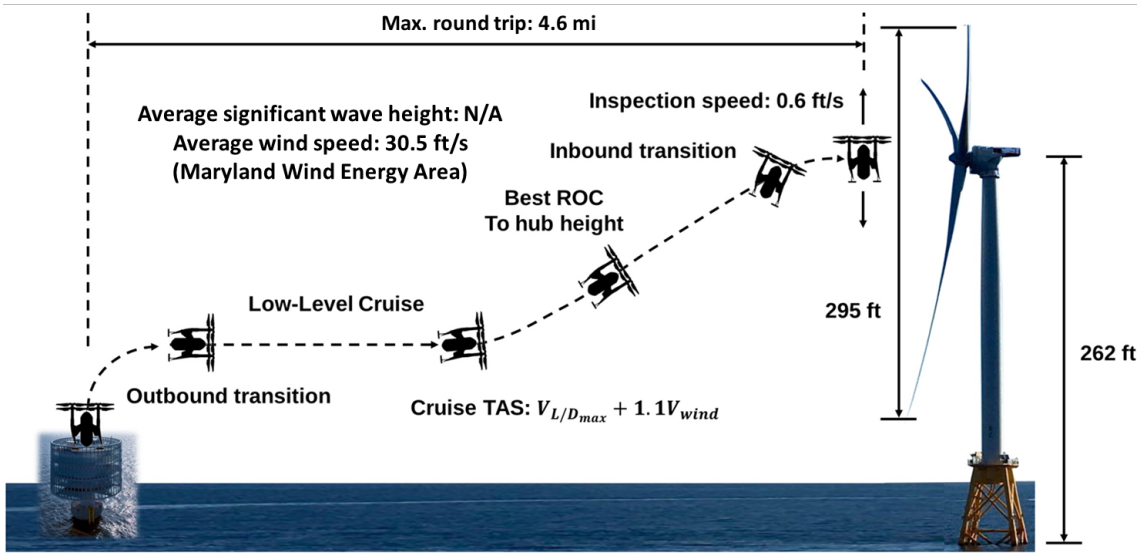

Figure 1.10: QBT inspection mission concept

1.2 QBT Design Considerations

In pursuing the design of a QBT, the primary consideration is how to model the levels of aerodynamic interaction between the vehicle's various components. Current QBT performance analysis and sizing studies at the University of Maryland are limited in that the theories employed are only capable of considering the

various components in isolation. As the aircraft's proprotors, wings, and body are all necessarily in close proximity with the rotor wake impinging on the aircraft in all normal operating modes, the extent of the mutual aerodynamic interactions of these bodies should be taken into account when sizing the aircraft. The following sections attempt to explicate the nature and extent of these interactions. Similarly, as this configuration is relatively new, a weight model appropriate to the configuration will need to be devised.

1.2.1 Proprotor/Proprotor Interactions

Beginning with the proprotors, it is demonstrated by Ramasamy [6] that, while the negative rotor to rotor interference effects can be dramatic, but also easily avoided for hovering, tandem rotors. In an experimental study concerning such rotor systems, he first presents a comparison of each rotors figure of merit as compared to the isolated case for a variety of radial separation distances. In this comparison, shown in Figure 1.11, rotors are vertically spaced by 0.07 rotor diameters to allow for complete overlap between the two rotor systems and are adjusted to remain at a constant thrust coefficient and in torque balance for all test points. As shown, hovering performance degrades rapidly as the two rotors are overlapped with one another and enter into a coaxial configuration.

While the author provides a more detailed discussion of coaxial arrangements, it can be summarized that the coaxial configuration required an increased power consumption of over 23% to meet the thrust production requirements for each rotor.

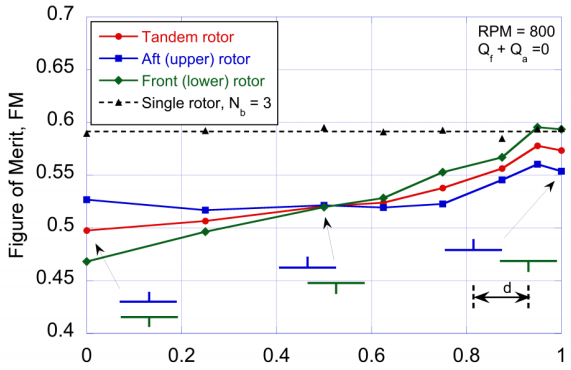

Figure 1.11: Overlapping tandem rotor performance comparison [6]

Similarly, the author also remarks on how the relative efficiency of the two rotors varies with radial separation, but ultimately notes that a full flow-field analysis is required to determine the physical mechanism behind the trends shown. For the sake of simplicity, however, a different case with no overlap will provide more guidance to this present study by mirroring current QBT designs.

As shown in Figure 1.12, where there is a radial gap of 1.1 rotor diameters between rotor axes and no vertical spacing between rotor discs, both rotors of the tandem configuration do not suffer from any performance penalties and show good agreement with the measured figure of merit for an isolated rotor. As noted, the rotors tested here required only minimal tip clearance to obviate rotor/rotor interference.

However, this is only a hover result, and computational results from Luo et. al. [7] note that it does not necessarily hold in the forward flight case. Utilizing a generic quadrotor configuration, as shown in Figure 1.13, Luo et. al. demonstrates that the convecting tip vortices from the front rotor negatively impact the performance of rotors directly downstream when the aircraft is in a level forward flight mode (akin

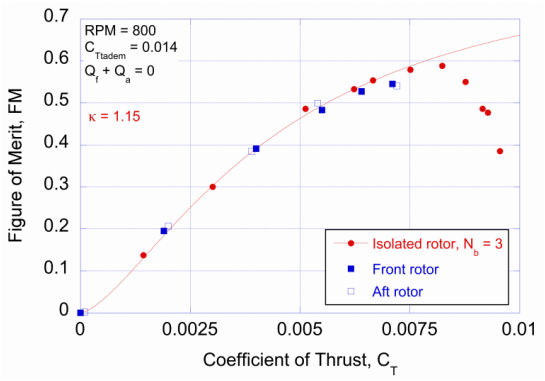

Figure 1.12: In-plane tandem rotor performance comparison for a radial separation of 1.1 rotor diameters [6]

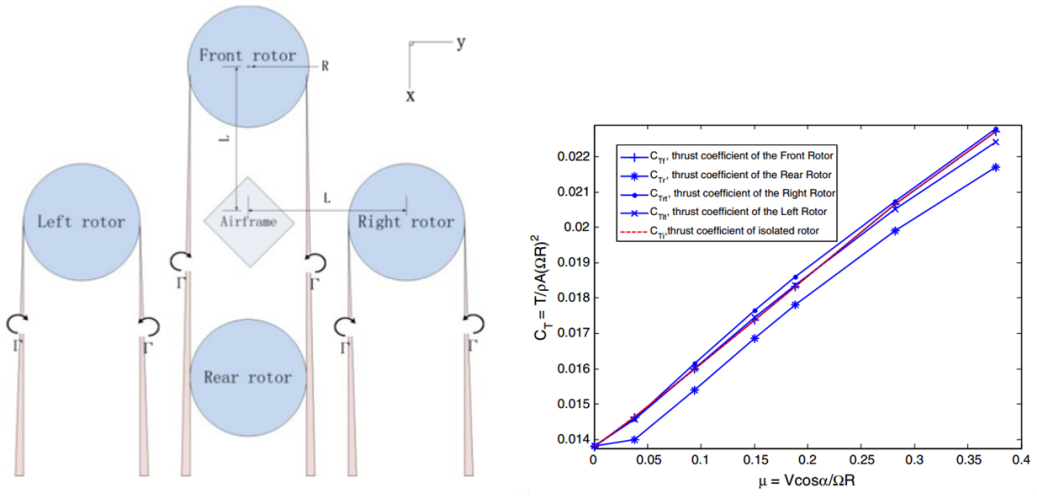

(a) Generic quadrotor configuration (b) Rotor/rotor interference

Figure 1.13: Rotor/rotor interference for a generic quadrotor in a crosswind [7]

to a sudden crosswind in hover). However, in the QBT case, this effect is unlikely to occur as envisioned by Luo et. al. as the aircraft (and thus the rotors) will likely be tilted into the relative wind for station-keeping when in a flight mode where these effects would be the most significant. Via this body tilt angle, the rotors discs will be brought out of plane with the relative wind, further distancing the downstream rotor from the convecting wake of the upstream rotors and negating significant effects of this interference, as discussed by the authors.

To date, the need for predicting these effects in a design-oriented framework has been met, to some extent, at the University of Maryland, by a comprehensive rotorcraft analysis tool based on an inviscid, incompressible, time-accurate Lagrangian free-vortex method. This methodology has been implemented in the Parallelized Rotorcraft Analysis for Simulation and Design (PrasadUM) tool developed by Rubenstein et. al. [40]. This tool has been validated against flight test data for an aircraft in both trimmed and maneuvering flight, including the UH-60A. At present, however, this tool lacks the ability to incorporate feedback effects from lifting surfaces, relying on aerodynamic lookup tables to define aerodynamic forces and moments acting on the airframe. The underlying methodology of this method will be discussed in a later part as it pertains to the present work.

1.2.2 Proprotor/Wing Interactions

With respect to proprotor/wing interactions, studies such as performed by Witkowski et. al. [41], Veldhuis [8], and Ananda et. al. [42] attest to the positive impact of a tractor propeller positioned in front of a wing. Veldhuis and Witkowski et. al. cite the effect of the propeller induced swirl on the wing as the primary mechanism for this. As the swirling air convects over the wing, it varies the local angle of attack and, depending on the rotational direction of the propeller (as shown in Figure 1.14), can favorably alter the wing's lift distribution so as to decrease the induced drag.

Take, for example, the swirl introduced by the propeller on the inboard side

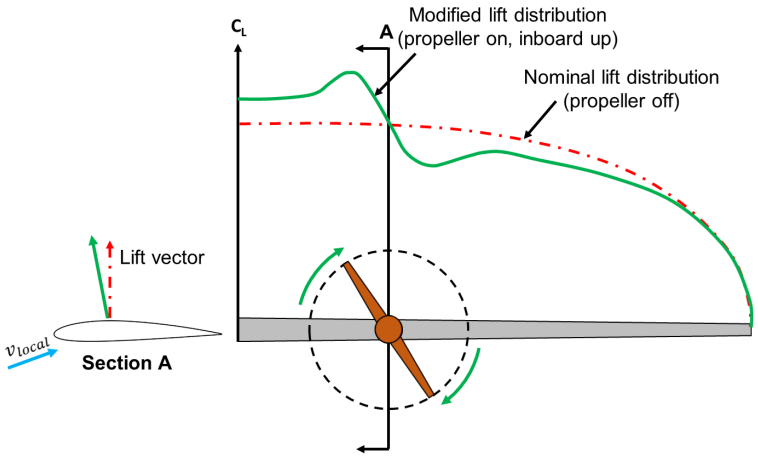

Figure 1.14: Lift distribution over a hypothetical wing as altered by a propeller's wake [8]

of the proprotor in Figure 1.14, which increases the local angle of attack aft of the rotor for an inboard up propeller rotation. Not only is the lift locally increased, but, relative to the rest of the wing, the force is directed in the upstream direction, decreasing drag. While the opposite is true on the outboard side of the propeller, the effects are lessened through the influence of spanwise flow closer to the wingtip. Hence, as the net pressure force is greater on the inboard side of the propeller, this results in an overall reduction in induced drag via a kind of "swirl recovery" mechanism analogous to the action of a stator vane.

Witkowski et. al. [41] cites a potential increase in the wing's lift to drag ratio by up to 40% (depending on propeller advance ratio) due to this effect. In addition, it is mentioned by both Witkowsky et. al. [41] and Leonardus [8] that as the propeller (in this case a proprotor) is moved closer to the wingtip, the favorable performance effects increase due to the effect of the propeller wake on the wingtip vortex. As seen, these effects are quite significant with respect to the aircraft's cruising performance.

Both authors also note favorable effects from this configuration on laminar-turbulent transition.

In its hovering flight mode, however, another investigation into propeller/wing interference effects by Hrishikeshavan et. al. [37] suggests that, when there is a purely edgewise freestream, the interference effects are diminished with respect to lift and drag production. Hence, in this particular sizing study, the proprotor/wing interference effects in hovering flight will be ignored by the preliminary design module. These effects will be captured in the final design module upon integration with a more realistic aerodynamic model.

With respect to higher-fidelity aerodynamic models, both Witkowski et. al. [41] and Leonardus [8] demonstrate the effectiveness of computational techniques that can be of use in predicting the interference effects previously described. While Leonardus's [8] work focuses on solving the Euler equations in the vicinity of a wing/propeller system, he also points out the possibility of implementing several lower order schemes; in particular a surface singularity method that results in a potential flow solution for an inflow prescribed by blade element momentum theory with swirl correction. This panel-based method, which utilizes source and doublet distributions across an arbitrary geometric surface, is of particular interest to this study as the required inputs could be prepared at a relatively early stage in the design process. It could also be coupled with inviscid free-vortex codes, such as developed by Rubenstein et. al. [40], to predict feed-forward and feed-back effects of the proprotor/wing/body interactions. Similarly, this could also begin to predict wing/wing and wing/body interference effects, although, given the spacing required

to provide adequate separation for a wing-mounted rotor system, it is not anticipated that these effects will be large.

However, while the an implementation of the computational methods described above will be useful in quantifying interference effects of a sized vehicle, the design process must also enable exploration of the available design space at lower levels of definition. For this, a lower-order aerodynamic model, such as momentum theory, will be required.

1.2.3 Wing/Wing Interactions

In an 1924 study, Prandtl [10] remarks on how a biplane wing system will generate less induced drag than a monoplane with equal span and loading. This is not to say that the biplane system is inherently superior to the monowing, however, but is a simple statement that the biplane configuration is more efficient for compact aircraft. This is a significant motivation to pursue the biplane concept; especially for UAS that will be stored and launched in areas with space restrictions, which is presumably the case for a wind turbine inspection aircraft where the vehicle will likely be stored at an on-farm facility. Similar motivation has driven a number of empirical studies in recent years, including a 2012 study by Maqsood et. al. [43] and a 2007 study by Moschetta and Thipyopas [44]. These works are primarily concerned with the development of a compact wing systems for use on micro aerial vehicles (vehicles in both studies weigh <0.44 lbf), and specifically investigate the potential of the biplane configuration for this application.

Both authors demonstrate that significant performance gains are possible through the conversion of a monowing configuration to a biplane configuration. Careful selection of the biplane planform is necessary, however, as the induced drag benefits afforded by such a configuration are balanced by a simultaneous increase in parasitic drag. Furthermore, to accommodate the gap to span ratio required to negate decreases in the lift to drag ratio caused by two lifting surfaces operating in close proximity (as noted by Hrishikeshavan et. al. [37], Munk [45], and Prandtl [10]), excess structural weight may also be required. To compute biplane wing performance in this study, semi-empirical corrections derived by Munk [45] and Prandtl [10] are utilized. Both sources give formulate correction factors to compute the drag of the biplane wing system from lifting-line results for isolated wings.

1.2.4 Weight Modeling

As this aircraft is still quite new and of a size not considered by traditional full-scale rotorcraft weight models, such as those developed by Tishchenko, Boeing-Vertol, and the Research and Technology Labs of the US Army Aviation R&D Command [46], the ability to correctly model component weight variations with respect to performance parameters requires significant development. Other models, such as developed by Winslow [47], are designed for aircraft in too light of a weight class and of a different configuration. Furthermore, as only two examples of this aircraft exist (to the author's knowledge) near to the desired scale, alternatives to historical weight trends must be considered. One alternative, as demonstrated by

Chambers et. al. [48], utilizes an assumed structural layout and known load paths to generate a structure from which a weight can be inferred. This methodology would prove invaluable for configuration specific components of the aircraft, particularly the wings, rotors, wing struts, and fuselage. As this project has been conducted in cooperation with a local injection molding firm, a candidate material has already been selected by the firm for the manufacture of the aircraft utilizing their processes.

For other components, such as the electronic speed controllers, batteries, and motors, a plethora of examples presently exist on the market and can be utilized to develop a weight model. As is the practice for model aircraft of this size, brushless direct current (BLDC) motors will be used for this aircraft. Winslow [47] notes that these motors operate at peak efficiency at high torques, making them the motor of choice for larger (over 0.22 lbf) aircraft such as will be contemplated here.

Similarly, as preliminary studies indicate that this aircraft will be energy-limited and not power-limited in terms of battery sizing, lithium polymer (LiPo) batteries will be considered as the power source as opposed to more power dense (albeit less energy dense) lithium iron phosphate batteries. As a variety of prepackaged LiPo batteries are sold for UAS, this also provides a significant database for a new weight model to draw from. Furthermore, due to the expected high current draw (in excess of 20 A), it is expected that the wiring connecting these batteries to the electronic speed controllers (ESCs) and motors will also contribute significantly to the weight buildup. As such, the wiring will be modeled using accepted standard practices used in the radio-controlled aircraft model building community. This method will be described in the following chapter.

The complete list of components to be considered in this work are listed below:

1. Wing
2. Fuselage
3. Wing/Fuselage struts
4. Landing gear
5. Rotors
6. Electronic speed controllers
7. Lithium polymer batteries
8. Brushless DC motors
9. Power transmission cables
10. Autonomous navigation systems

1.3 Objectives

To aid in filling the aforementioned needs found in offshore wind maintenance and the QBT design process, the objectives of this thesis are as follows:

1. Quantify the potential for applying the QBT configuration to offshore wind energy maintenance support missions.

2. Implement a weight model for QBT configured aircraft to enable sizing predictions.

3. Create a preliminary sizing framework to enable initial explorations of the design space for QBT aircraft, particularly for offshore wind inspection missions.

4. Develop an aerodynamic solver for lifting bodies that can be coupled with a rotor analysis code to predict interference effects caused by the proprotor/wing/body system.

1.4 Organization of the Thesis

The achievement of the aforementioned objectives is described in the following chapters. Beginning with Chapter 2, the motivation for use of a QBT configured aircraft for offshore wind maintenance inspections will be explicated with an eye towards use of the aircraft in the Maryland offshore wind energy area.

Chapter 3 will encompass the details pertaining to the preliminary sizing tool developed as part of this work, including: weight modeling, structural considerations, geometric considerations pertaining to the layout of major components, and aerodynamic modeling.

Chapter 4 will discuss vehicle analysis tools that follow on the results of the preliminary sizing tool. This begins with describing the methodology required to generate wing and body geometries as well as the rotor design. Following this will be a description of the aerodynamics of the panel method implementation developed for on-body aerodynamics, the inviscid free-vortex code adapted for use in this work, and the integration of these codes into the design sequence.

Chapter 5 will present results from the completed sizing tool for various cases of interest, including both off- and onshore inspection missions, and a discussion thereof.

Chapter 6 concludes the thesis with a brief summary of conclusions from the work as well as recommendations for future work.

Chapter 2: Offhore Wind Inspection Mission Concept

In order to further define a motivation for the use of a QBT in offshore wind inspection missions, this chapter contemplates the question of turbine accessibility as well as the efficacy of various inspection techniques in completing turbine inspections on the scale of a complete wind farm. The discussion begins, however, with a brief background of the QBT configuration itself.

2.1 The QBT: Motivation and Background

As has been the case in a variety of aircraft, be they tilt-rotor, tilt-fan, tilt-wing, and so on, the QBT configuration attempts to combine the vertical takeoff, landing, and hovering capabilities of a traditional rotorcraft with the forward flight efficiency of a fixed-wing aircraft. However, the trademark of this new configuration lies in its inherent simplicity. As shown in Figure **??**, the QBT is unique in that it requires no additional moving parts to facilitate transition between these two flight modes, thus decreasing the required mechanical complexity. Several studies concerning the new configuration's initial development [37], controls [49, 50], and flight testing [5, 38] have already been undertaken by the University and continue at the time of writing.

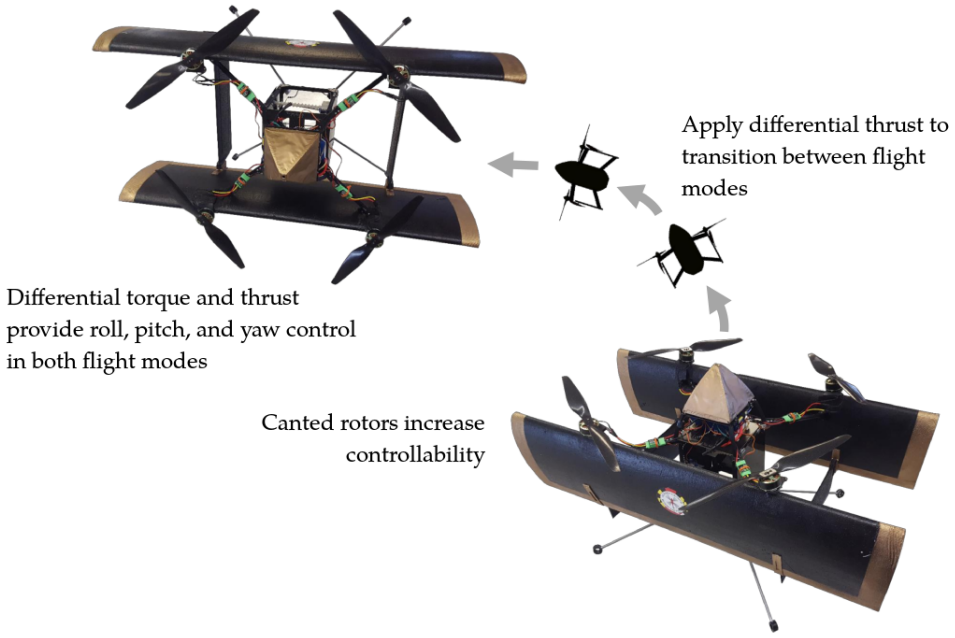

Figure 2.1: Tilt-body configuration

Similar aircraft to this concept have been demonstrated by 3 companies, to the author's knowledge: Parrot, Transition Robotics Inc, and Joby Energy. Transition Robotics has sold a variety of tilt-body vehicles, these have been monowing aircraft with proprotors offset both lateral and vertical directions in order to provide control. While this design retains a great simplicity, it may be difficult to scale to larger vehicles due to the prohibitive large wing that may be required. Furthermore, as noted by Prandtl [10], two wings of equal span and with sufficient clearance produce less induced drag as compared to a monowing producing the same total lift. A more recent development by the company, the Jumpship, appears to follow this logic. The Jumpship [51] is an octrotor biplane advertised to be capable of carrying an 11 lbf payload up to 50 mi. This aircraft most closely parallels the QBT design discussed previously, but is not yet available to the public and, at the time of writing, there has been no announcement of a successful flight test. The Swing, another example

produced by Parrot [52], is a X-winged quadrotor-biplane built for the consumer market. This latter aircraft is, presumably, a recreational vehicle not designed to carry a particular payload and is only rated for a maximum speed of 27.3 ft/s. Further specifications are not publicly available for this vehicle. For either vehicle, the design methodology has not been made available in the public domain. Both of the commercialized vehicles mentioned are shown in Figure 2.2.

(a) Parrot Swing [52] (b) Transition Robotics Jumpship [51]

Figure 2.2: Commercialized QBT aircraft marketed in the US

In academia, several examples of tailsitters exist, albeit with varied control systems. In works by Hogge [53], Stone et. al. [54], Kubo and Suzuki [55], and Bapst et. al. [56], a number of different tailsitter vehicles are proposed, built, and flown that utilize a monowing configuration. The aircraft in Figure 2.3(a), designed by [53] was built as a flying testbed for UAS research, utilizes only a single, electrically driven ducted proprotor for propulsion. The aircraft utilizes both a set of vanes and elevons for flight control. The vehicles developed by [55, 56] in 2.3(d) and 2.3(b) leverage a synergy of tandem rotors and elevons (or other traditional flight control surfaces) to maneuver and transition between hovering and forward flight modes. The T-Wing, developed by [54] and shown in 2.3(c), is of a more conventional design, utilizing gasoline engines and thus relying primarily on a conventional set of control surfaces

submerged in the proprotor slipstreams. The vehicles developed by [56] and [55] take advantage of the same principle, but, as they both use electric motors, also utilize differential torque inputs as a flight control. All four vehicles are pictured in Figure 2.3. These vehicles are largely the result of successful efforts to provide a proof of concept or technology demonstrator for a tailsitter UAS capable of providing both a high speed forward flight capability while enabling operation from a confined takeoff and landing zone.

(a) Single-rotor Tailsitter [53]

(b) Tandem-rotor tailsitter [56]

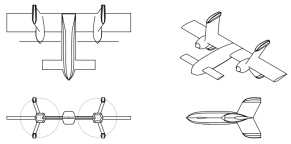

(c) "T-Wing" tailsitter [54]

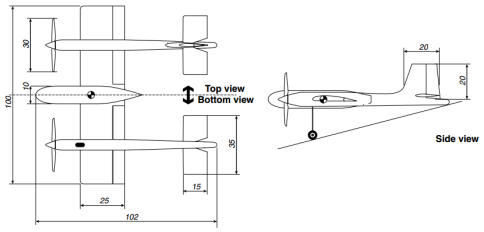

(d) Tailsitter with high lift devices [55]

Figure 2.3: Tailsitter UAS designs utilizing a various mixtures of conventional flight controls and motor torque for control

As seen, all of these vehicles require at least a minimal set of flight controls (e.g., elevators, vanes, etc.) as their single or tandem rotors can only be utilized to provide a response in roll and/or yaw. As previously noted, a quadrotor arrangement, as used by [5] and [38], enables control over all three axes through selectively varying each motor's speed, potentially allowing the designer to forgo any conventional control surfaces: greatly simplifying the mechanical design. Furthermore, as

is noted by Stone et. al. [54], transition from horizontal to vertical flight is impeded for these tandem designs by dynamic wing stall during the maneuver which results in a temporary loss of control surface effectiveness at low proprotor thrust settings. In contrast to this, as a quadcopter control scheme relies wholly on differential thrust and torque. Hence, for the transition described by Stone et. al., the entire transition is effected by application of proprotor thrust vectors, allowing the UAS to maintain control authority throughout the entire maneuver. Hence, in addition to a simplified control scheme, the quadrotor configuration also adds a degree of robustness to the tailsitter's flight controls over the aircraft's entire performance envelope. This is of great interest to a UAS in the wind turbine inspection mission as the aircraft will spend prolonged periods of time operating in close proximity to turbine structures and in high winds.

A survey of UAS that incorporate a quadrotor control concept into a tailsitter design is given in Figure 2.4. The aircraft shown here are purposely selected from aircraft not developed at the University of Maryland.

These vehicles represent a variety of missions, including: package delivery in Figure 2.4(a) [57], aerial mapping and surveying in Figure 2.4(d) [60], technology demonstration and development in Figure 2.4(c) [59] and Figure 2.4(b) [58], respectively, and high-altitude wind energy harvesting (albeit only proof of concept) in 2.4(e) [61]. Interestingly enough, the ATMOS vehicle [60] (shown in Figure 2.4d is specified to a very similar mission to that which is of interest, although it has seen use primarily for onshore applications. Unfortunately, details of this vehicle (e.g., manufacturing methodology, etc.) are not publicly available. However, it is speci-

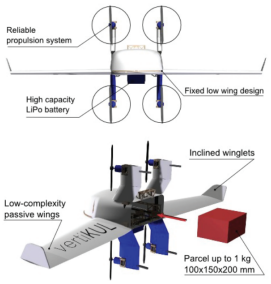

(a) VertiKUL [57]

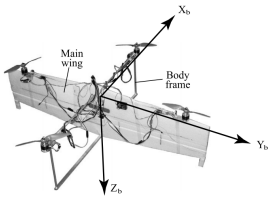

(b) Test Vehicle [58]

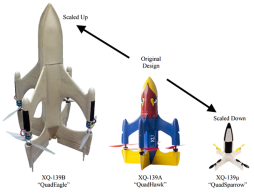

(c) XQ-139 family [59]

(d) ATMOS Drone [60]

(e) Mercury 9 [61]

(f) VertiKUL 2 [62]

Figure 2.4: Tailsitter UAS designs utilizing quadrotor propulsion and control

fied as a 9.9 lbf vehicle capable of carrying a 1.1 lbf payload with a maximum range and endurance of 37.2 mi and 60 minutes, respectively. These appear promising, although further detail is not given.

A significant note of interest from these comes from the discussion surrounding the redesign of the vehicle in Figure 2.4(a). The brief notes found concerning its successor, the VertiKUL 2, shown in Figure 2.4(f), remark on how the original aircraft was not sufficiently controllable in windy conditions. According to an interview with the lead researcher [63], the redesigned aircraft dramatically reduced its wing area in an effort to mitigate this. To compensate for the reduced size of the wing, the aircraft's fuselage was reshaped into a lifting body and the proprotors installed with a significant degree of shaft tilt such that, in cruising flight, the rotors would still generate a significant portion of the lifting force. While this design choice

may limit the vehicle's forward speed and wind penetration, it appears to have been effective at increasing stability in windy conditions.

Unfortunately, further discussion on this topic of gust mitigation by other designs, particularly the ATMOS and Mercury 9, is not forthcoming at the present time. Mercury 9 is of particular interest given that the mission of a full-scale prototype would be to harvest energy from high altitude winds, but no detail is given concerning this aircraft or any of its predecessors. However, as an effort towards this end, one should also consider the reduced projected wing area of the biplane configuration relative to the vehicle in Figure 2.4(a). Similarly, Yeo et. al. [49] have been active in designing a bio-inspired gust mitigation system for use on UAS. While neither of these constitute a panacea, gust mitigation will be an object of continued study with respect to the QBT configuration as research on the topic continues to advance and will no longer be considered in this thesis.

In the interest of establishing tools and motivation for applying this aircraft to offshore wind turbine inspection missions, then, this thesis will now concern itself with establishing a motivation for use of the QBT configuration to perform the inspection of offshore wind turbines.

2.2 Offshore Wind inspection Mission Analysis

As noted in Chapter 1, the question of turbine accessibility is significant to the implementation of predictive maintenance strategies. While this includes the ability to complete a routine turbine inspection, it also concerns itself with on-

demand inspections of potentially damaged components. Such inspections enable the ability to produce a useful life estimate and a maintenance mission scheduled around available weather windows.

Hence, the accessibility analysis solely considers the ability of a particular inspection method to inspect a turbine based on vehicle performance limitations, required inspection times, and real-world metocean conditions. Metocean conditions are drawn from the Maryland offshore wind energy area as provided by buoy 44009 of the National Oceanographic and Atmospheric Administration (NOAA) [3], and predicted seasonal variations in daylight hours given by the US Naval Observatory [64]. Estimated of inspection times and limitations were gathered from Maples et. al. [23] as well as various UAS manufacturers (as listed in Chapter 1). A summary of the various means of inspection considered here and their respective weather limitations are given in Table 2.1.

Table 2.1: Summary of inspection methods and limitations

Method	Inspection Time	Weather Limits
Roped inspector	3 hr	Waves < 4.9 ft
CTV-borne UAS	20 min	Waves < 4.9 ft Wind < 50 ft/s
QBT [9]	22 min	Wind < 67 ft/s

Specifically for this study, the inspection methods include roped inspectors utilizing CTV transport (CTV), unmanned inspections utilizing typical multicopter UAS transported by CTV to a turbine (CTV+UAS), an unmanned QBT aircraft flying only during daylight hours (QBT(D)), and an unmanned QBT aircraft carrying additional lighting equipment to allow for nighttime inspections (QBT(N)).

The mission profile for the missions employing either roped inspectors (CTV) or multicopter UAS (CTV+UAS) is shown in Figure 2.5.

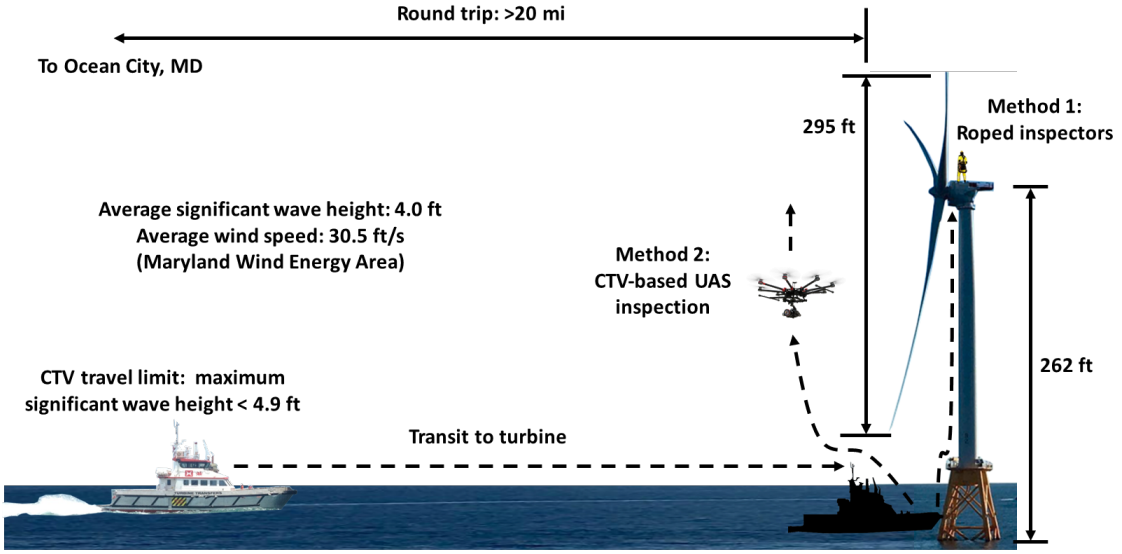

Figure 2.5: Inspection mission concepts requiring manned transportation to the turbine

The QBT aircraft model used here is the previously mentioned package delivery vehicle designed by Sidle et. al. [9]. While not optimized for the offshore wind arena, it does have several features of interest to an offshore wind inspection aircraft, including a 5 lbf payload capacity: sufficient to carry a gimbal, a high-definition EO camera, and a thermal imaging camera. The report also quotes a maximum range of 175 miles, a maximum endurance of up to 6 hours, and a maximum speed of 148 ft/s: more than sufficient to provide for the inspection of an offshore wind turbine, even from a remote location. Sacrificing range and endurance, its payload could be increased up to 15 lbf in the present configuration [9]. A rendering of the aircraft can be seen in Figure 2.6.

In contrast with the mission profile in Figure 2.5, this aircraft could take

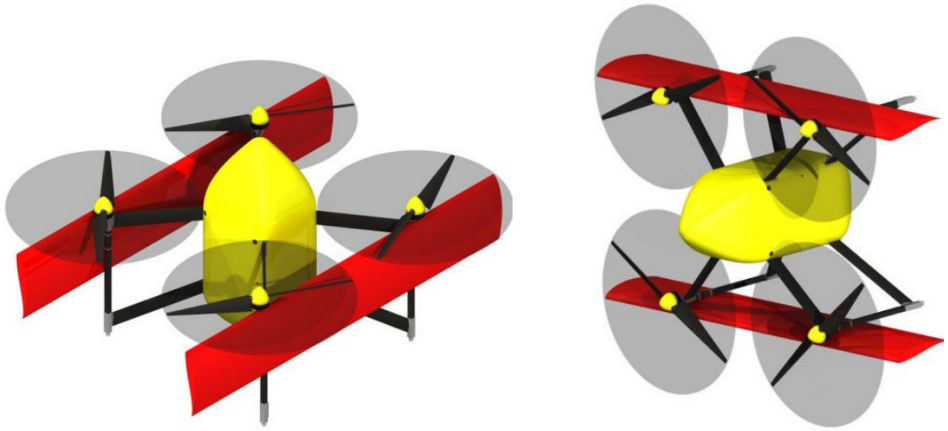

(a) Hovering flight mode (b) Forward flight mode

Figure 2.6: Package delivery QBT in its two primary flight modes [9]

advantage of its increased range and endurance to perform missions autonomously from within the wind farm without a support vehicle, effectively decoupling the inspection mission from wave conditions. This mission profile is shown in Figure 2.7. While any UAS could, conceivably, be equipped so as to fly autonomously, typical UAS do not have the range or endurance to leverage autonomous capabilities without a support vehicle for supplementary transport within the wind farm itself.

2.2.1 Turbine Accessibility Analysis Results

This section considers the question of turbine accessibility, comparing manned CTV inspections, CTV-borne UAS inspections, and QBT inspections, following the paradigm proposed in the previous section, on their ability to inspect a turbine given their various limitations, respective performance, and metocean conditions at the turbine (all as defined in the previous section). This results of this study can be

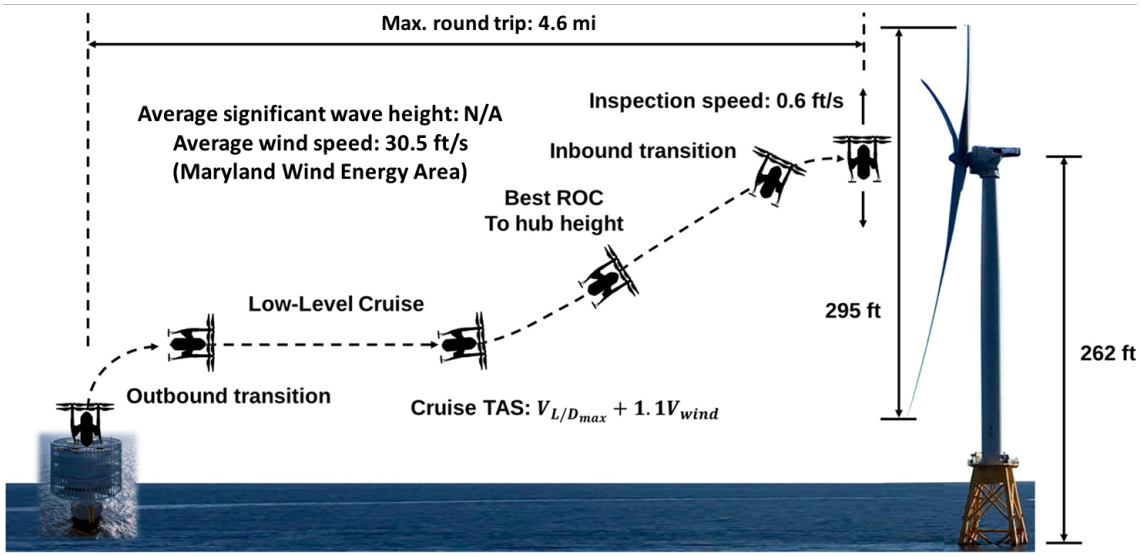

Figure 2.7: QBT inspection mission concept

seen in Figure 2.8.

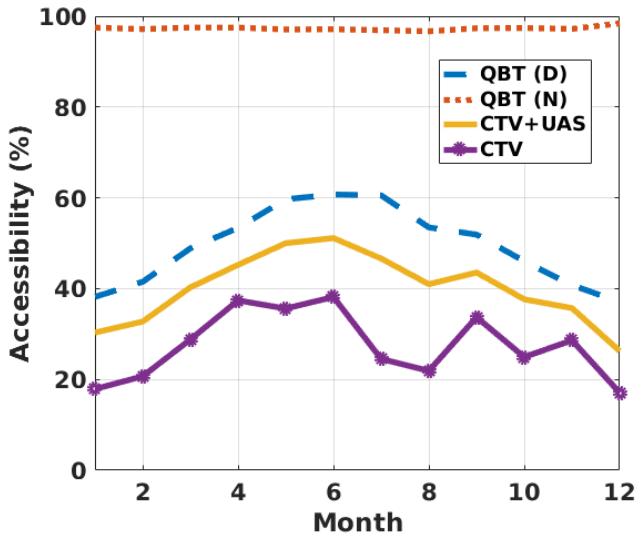

Figure 2.8: Wind turbine accessibility for inspection

As shown, the extended inspection times required by manned missions significantly decrease turbine accessibility rates to, on average, 27% for conventional CTV-based missions. While the use of UAS to accelerate the inspection process

increases that rate to 40%, it is still susceptible to wave states and more susceptible than QBT aircraft to wind speed. Hence, further decoupling of the inspection method from metocean conditions through the use of a QBT aircraft further increases the average accessibility rate to 49%, restricted almost entirely by daylight hours of operation. If an autonomous aircraft can be utilized, as in the case of the QBT(N) trace, inspections could be performed on a consistent basis year-round with over 95% accessibility to the turbine.

This capability could prove decisive in performing unscheduled maintenance missions, in addition to performing regular maintenance inspections: thus decreasing turbine downtime, liability, and maintenance costs. As shown by Lei et. al. [18] as well as Sarker and Fiaz [19], the ability to have a decisive and accurate end-of-life prediction for a critical turbine component can drive a strategic maintenance model that leverages available weather windows for turbine accessibility by boat. This aircraft could, in theory, conduct inspections year-round and in weather ordinarily not passable by manned vessels, thus enabling a wind project operator to more quickly identify potential problems and prepare to correct them even before a weather window opens for manned sea travel. Furthermore, though it depends on the regulatory environment, the QBT could be outfitted with sufficient lighting systems to operate even at night to further decrease turbine downtime.

2.2.2 Farm-Level Inspection Simulation Definition

The advantage of UAS in the blade inspection role becomes even more evident in a more detailed mission analysis considering the inspection of a complete wind farm. Instead of computing turbine accessibility purely as a function of inspection time and weather history, this analysis engages the aforementioned inspection methods to inspect all turbines of a hypothetical wind farm located in the Maryland offshore wind energy area, roughly 10 nm due East of Ocean City, Maryland (the "shore base" for this analysis). As no large scale offshore wind farms exist in the United States at the time of writing, this simulation adopts the layout of the Robin Rigg windfarm, a grid-style farm located in the Solway Firth in the United Kingdom [22]. This layout includes an array of 60 Vestas V90 3 MW [65] turbines, each with a rotor diameter of 90 m.

In the first scenario, a manned inspection, it is assumed that only one CTV is available and that it takes 3 hours for a traditional, roped inspector to survey an individual turbine after arriving at said turbine. In the second scenario, it is assumed that only a single multicopter and a single CTV is available and that a single turbine inspection requires 20 minutes to complete. A sufficient supply of charged batteries for these inspections is assumed to be held onboard the CTV at all times. Furthermore, the model assumes that both CTV+UAS inspections and manned inspections can only be performed during daylight hours. For both cases, it is assumed that the CTV is based on shore, has a transit speed of 49 ft/s [66], and can only travel when the maximum significant wave height is less than 4.9

ft [23]. CTV performance parameters have been derived from Dinwoodie et. al. [67] and Maples et. al. [23]. Similarly, the UAS in the second case is assumed to be operational only in winds under 50 ft/s, a value representative of current UAS used in wind turbine inspections as shown in Table 1.2, found at the beginning of this chapter.

In the final four scenarios, the inspection is carried out by the QBT package delivery vehicle described previously, albeit from difference base locations. Two cases consider the QBT to be flying directly to the turbines from the same shore location as the CTV supported missions. The latter two cases base the aircraft on a substation platform at the wind farm itself. These base locations are denoted by annotations of "shore" or "farm," respectively.

This latter base location accounts for the possibility of independent operation that is afforded by the QBT configuration. As the aircraft does not need a manned support vehicle (given sufficient autonomy), it would suffice to provide for recharging the aircraft's batteries between inspection missions, a duty that could be performed by an autonomous recharging platform. This capability would further enhance the readiness of the aircraft for on-demand inspections and provide greater value to the wind farm operator.

In order to inspect the turbines, the QBT transits the rotor radius twice per blade, imaging both sides of the blade as well as the leading edge. In these hypothetical missions, the QBT carries a UAV Vision CM160 gimbal [68] outfitted with a high-definition video camera and a FLIR Tau 640 thermal imaging camera. This latter camera, with a 30 Hz shutter speed and 640x512 thermally sensitive

pixels, requires a transit speed not greater than 0.653 ft/s in order to avoid blurring more than 2 pixels (roughly 0.5 in of the imaged rotor blade) during a shutter event. Given this limitation, a 3-bladed rotor can be imaged in about 22 minutes, a figure within the range of inspection times advertised by Aibotix GmbH [29] and Cyberhawk Innovations Ltd [27], two operators of UAS for offshore wind turbine inspections.

To model the metocean conditions at the turbines, a model was adopted from Feng and Shen that utilizes a joint probability density function (JPDF) to correlate wind direction and speed. To construct this, wind speeds are first sorted into 15°-wide directional bins, for a total of $N_s = 24$ bins. The information in these bins is then separated into 5 ft/s-wide speed bins, allowing a 2-parameter Weibull distribution to be constructed to model the wind speed in each directional bin. The joint probability density function is calculated using Equation 2.1, resulting in Figure 2.9. In the following expression, f_n is the proportion of the total information that is contained in the nth directional bin, and $p_{wind}(v, c_n, k_n)$ is the probability given by the Weibull distribution as a function of wind speed and Weibull parameters for the nth directional bin [69].

$$jpdf(v, \theta) = p_{wind}(v, c_n, k_n)\frac{f_n}{360/N_s} \tag{2.1}$$

This JPDF is sampled by first creating a marginal probability distribution with respect to wind direction, as shown in Equation 2.2.

$$m_{pdf}(\theta_n) = \sum_{x=1}^{i} jpdf(v_x, \theta_n) \tag{2.2}$$

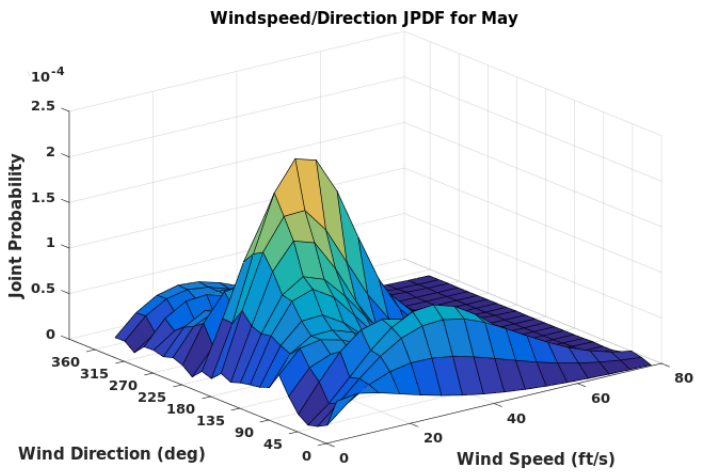

Figure 2.9: Joint probability density function(May)

These normalized marginal distributions are mapped onto a uniformly distributed random variable ranging from 0 to 1. $m_{pdf}(\theta_n)$ is formed by summing the joint probability associated with the ith windspeed in the nth directional bin of the JPDF. This is then normalized into $mnorm_{pdf}(\theta_n)$ by dividing $m_{pdf}(\theta)$ by its summation over the total number of directional bins, n_{dbin}, as in Equation 2.3.

$$mnorm_{pdf}(\theta) = \frac{m_{pdf}(\theta)}{\sum_{x=1}^{n_{dbin}} m_{pdf}(\theta_x)} \tag{2.3}$$

This normalized distribution is sampled by mapping a value from a uniform probability distribution onto the normalized marginal probability density function, allowing for a wind direction to be selected. The parameters for the Weibull distribution of wind speed are estimated via linear interpolation to better match the sampled wind direction and wind speed, respectively, instead of selecting the parameters from a piecewise function of wind direction and wind speed.

As metocean data is only available on an hour by hour basis in the available buoy data [3], each wind speed is assumed to persist in its given direction and speed

for n hours, where n is the number of consecutive data points in a particular wind speed bin that occur in the same directional bin. These values of wind persistence are also assumed to fit a 2-parameter Weibull distribution. Values for wind persistence are sampled according to the wind direction sampled from the aforementioned JPDF constructed for the present month. Seasonal effects are evident from the data (as can be seen in Figure 1.5), so a separate JPDF is constructed for each month and will be referenced accordingly.

Date changes are effected every 24 hours. Nighttime and daylight hours on a given day are based on predictions by the US Naval Observatory's Astronomical Applications Department [64]. Furthermore, weather predictions are renewed each "morning" if a daylight-only inspection method did not complete its mission by the end of the previous period of daylight. The intervening time of darkness, approximated by the subtraction of the total daylight time in that "day" from 24 hours, is added to its mission time. Methods that can operate at night as well as during the day are assumed to be in constant operation and the simulation continues to generate weather predictions without interruption. Furthermore, each mission is assumed to start on the 1st of the given month and continues from that date until it is complete. To account for the effect of seasonal weather variations, separate simulations are run for inspections are initiated at the beginning of each month.

As wave direction was not reported for all years of the NOAA buoy data, the effects of ocean currents as well as the effects of wind on CTV travel were not considered in this study. However, in order to capture wave height effects and their impact on CTV travel, a 2-parameter Weibull distribution was fit to the significant

wave height data for each month. Similar to the computation of wind persistence, the persistence of the binned significant wave heights were collected and fit with a 2-parameter Weibull distribution and sampled in a similar fashion.

Via numerical experimentation, it was found that 200 simulations of a full-farm inspection for each inspection method was sufficient to produce statistically significant results concerning mean mission time and the standard deviation of mission time during each month.

2.2.3 Farm Inspection Analysis: Results and Discussion

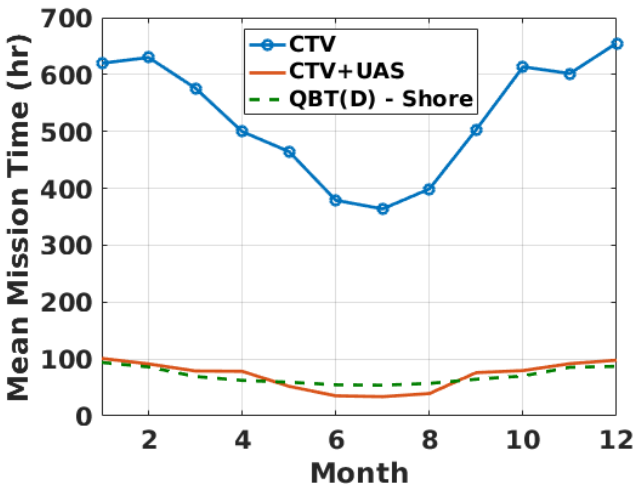

Figure 2.10: Mean inspection times - 1 CTV, 1 QBT

Considering the six cases previously discussed, an analysis of the average inspection time per month is shown in Figure 2.10 for three of the cases previously discussed. In this first set of results, it is assumed only 1 QBT and 1 CTV are utilized to conduct farm inspections. However, since the time required for a manned, CTV-based inspection of the wind farm is over 5 times greater than the other in-

spection methods examined (as seen in summary in Figure 2.11), it will be neglected in the following plots for greater emphasis on the data of interest. This also implies the significant costs associated with the manned inspection of offshore wind farms as compared with unmanned methods.

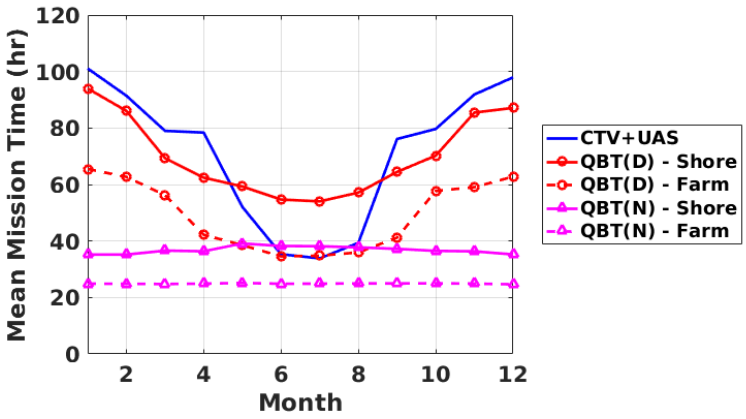

Figure 2.11: Mean inspection time - 1 CTV, 1 QBT

The mission times then shown in Figure 2.11 show the mean monthly mission times for the variety of UAS-based inspection methods of interest for this study. One can observe the effect of metocean weather in the dramatic seasonal variation of the results, particularly between the summer months and the remainder of the year. This variation is more dramatic in the wave modeling than the wind modeling, but this may be an artifact of the longer persistence times of given wave states as opposed to the persistence of meteorological conditions. The effects of daylight modeling can be observed in the differences between the QBT(D) and QBT(N) missions as the variation in mean mission time between the aforementioned missions roughly corresponds to multiples of 12 hours (the mean quantity of night-time). This underscores the potential for autonomous aircraft equipped with sufficient lighting

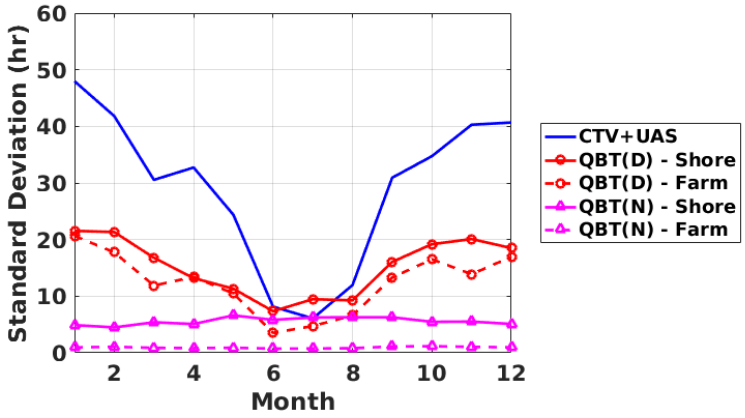

Figure 2.12: Standard deviation of inspection time - 1 CTV, 1 QBT

to enable nighttime missions.

The effect of metocean conditions within a given month can be observed via Figure 2.12, which plots the standard deviation in each month's 200 simulated mission times.

The effectiveness of utilizing a CTV-based UAS to perform inspections is immediately evident in its ability to complete an inspection of every turbine in the farm in under a week for the majority of the year, whereas, as previously mentioned, the yearly mean time for a manned mission transported via CTV is over 5 times that of any of the UAS-based method studied here. Similarly, due to the increased inspection times and thus increased susceptibility to metocean conditions, its seasonal variation is quite dramatic. This is captured both in the high variance of mean monthly mission times throughout the year and the standard deviation values plotted in Figure 2.12.

The values in this latter plot gives insight to the effect of metocean conditions and inspection rate within a given month and shows how much more of an

effect oceanic conditions can have on the two access methods studied as opposed to meteorological conditions. However, as can be noted by a comparison between the standard deviation in the CTV+UAS missions (σ = 29.1 hr, yearly average) and manned methods (σ = 106.4 hr, yearly average), this can be directly reduced by decreasing the amount of time required for an inspection. This reduction allows one to leverage a favorable weather window for more inspections, even if the CTV+UAS method requires a window of both favorable meteorological and oceanic conditions.

As noted, however, either of the CTV-based methods suffer from extreme seasonal effects and limited accessibility when compared to QBT methods. Whereas the QBT has a relatively high tolerance of meteorological conditions and is immune to oceanic conditions, it can access the turbines at a significantly higher rate than CTV-based methods. Hence, while the QBT concept also has some seasonal variation in inspection time, its maximum variation is about 2/3 as much as is observed by the CTV-based UAS during the majority of the year (this excludes inspections during the month of December).

The main difference between the QBT and CTV-based methods comes in the location of the QBT's operations center. If on shore, the extra travel time required of the QBT limits its effectiveness relative to the CTV+UAS method, particularly is it limited to daytime flight, and the annual mean mission time (i.e., the mean of the monthly mean mission times) for the two methods varies by only 1.4% relative to one another. However, if based on, for example, a substation platform, the aircraft performs a farm inspection in 69% of the time required by the CTV borne UAS with a significantly decreased seasonal variation in mission time. In the case of the

daytime limited QBT, the mission times vary from month to month by $\sigma = 12.3$ hr and, in the case of the night-time enabled QBT, this shrinks to only $\sigma = 0.12$ hr.

A tabulation of this results can been seen in Table 2.2. As discussed, the performance afforded by the QBT configuration, particularly enabled by equipment for nighttime missions and an on-farm base location, are emphasized not only by decreased mission times, but also greater mission consistency. This latter component, which enables on-demand turbine inspections, is crucial for the timely planning of maintenance missions to damaged turbines as well as in generating timely end-of-life predictions for operational turbine components.

Table 2.2: Summary of inspection mission results

Method	Base	Mean Mission Time (hr)	Annual σ (hr)
CTV+UAS	Shore	71.3	29.2
QBT (D)	Shore	70.3	15.3
QBT (D)	Farm	49.3	12.5
QBT (N)	Shore	36.8	5.6
QBT (N)	Farm	24.9	0.9

However, these simulations consider the use of what is, presently, a conceptual QBT design. As shown in a previous section, few, if any QBT designs have been physically realized, and none on the scale that is desired for the present application. The design methodologies for what designs presently exist have not been discussed in the public domain to the author's knowledge, save those designs formulated at the University of Maryland by Phillips et. al. [5], Hrishikeshavan et. al. [37, 38], Sidle et. al. [9], or Trollinger et. al. [39]. These methodologies, while providing a first look at some challenges and opportunities in QBT design, do not provide a robust

accounting for QBT-specific design challenges, if at all. Of foremost concern for this study are the interference effects that are anticipated in such a configuration.

Chapter 3: Preliminary Design Methodology

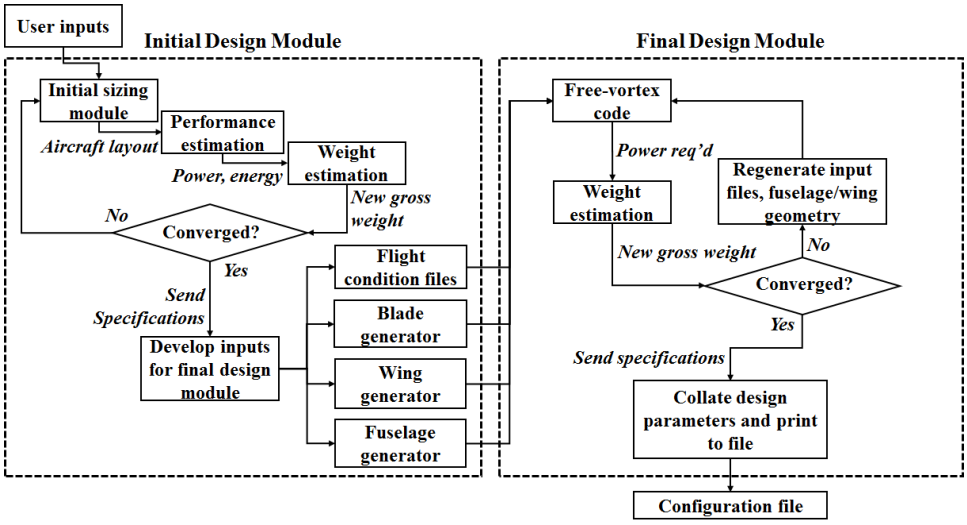

Figure 3.1: Flowchart for the integrated QBT design code

The preliminary design module discussed in the following parts corresponds to the initial design module diagram in Figure 3.1. This section concerns itself with the preliminary sizing of the aircraft and comprises two parts: a discussion of performance estimation techniques utilized in this design framework as well as the weight model built for this particular configuration.

3.1 Performance Estimation

In the preliminary design module, an aircraft is sized (as possible) for combinations of disc loading, wing loading, rotor solidity, and wing aspect ratio. This sizing utilizes a combination of momentum theory for rotor aerodynamics from Leishman [70], lifting line theory from Anderson [71], and parasite drag approximations from Raymer [72] and Hoerner [73]. In preliminary studies, the basic aerodynamic modeling afforded by these models has been validated against a similar lower-order methodology utilized by Sidle et. al. [9].

To make this code suitable for QBT design problems, however, an accounting for the aforementioned interference effects is implemented via the following methods. These methods are acknowledged to be preliminary in nature and are pending more detailed approximations to be derived from further research into the configuration and its aerodynamic characteristics. However, in the interim, they fill a gap in the QBT design framework by granting the designer some initial insights while considering the aerodynamic complexity of the QBT configuration. It is useful to keep in mind that the proposed aircraft is expected to have a GTOW of roughly 40 lbf, a wingspan of approximately 6 ft, a mean aerodynamic chord of roughly 1 ft, and rotor diameters of around 3 ft. Also, for purposes of simplicity, it is assumed that the aircraft has equal rectangular wings with no decalage or stagger.

3.1.1 Proprotor/Proprotor Interference Effects

As discussed in Chapter 1, the interference effects between two tandem rotors operating on the same plane is negligible, provided that the in-plane velocity component is small and the two rotors are not overlapping. Accordingly, the sizing module automatically places rotors such that their rotation axes are separated by at least 1.1 rotor diameters. Rotor placement is also varied by fuselage radius as the code enforces a minimum fuselage/rotor axis separation of 1.1 rotor radii. As the aircraft will constantly be oriented such that the in-plane velocity is relatively small, be it either in the cruising configuration (where axial flow dominates) or at an angle for station-keeping in hover, these interference effects will be neglected in the present analysis.

3.1.2 Proprotor/Wing Interference Effects

As a first approximation of these effects, data from the experimental investigations by Witkowski et. al. [41] into propeller/wing interference effects is utilized as a model. An extract of this, shown in Figure 3.2, shows the lift and drag coefficients for a semi-span wing operating at a Reynolds number of 470,000 at Mach 0.1 with a tractor propeller positioned one blade length from the wingtip.

While a QBT aircraft sized for an offshore wind mission is expected to have a similar operating Reynolds number to the wing in the study, it is also expected to have a much lower propeller advance ratio (on the order of 0.65) as well as a lower wing aspect ratio. However, as mentioned by both Witkowski et. al. [41] and

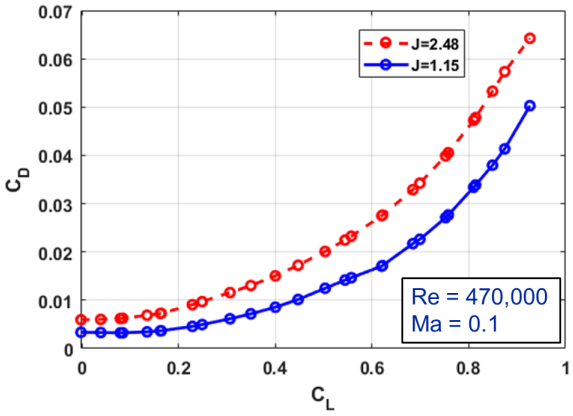

Figure 3.2: Drag polar for a semi-span wing/propeller combination at various power settings (wing aspect ratio is 8.25)

Veldhuis [8], this favorable induced drag effect is intensified at lower aspect ratios and propeller advance ratios. Hence, the lift to drag relationship (derived from the experiments of Witkowski et. al. [41]) given for the lowest advance ratio surveyed by Witkowski et. al. is taken as a "best-case" scenario and is fit with a nonlinear least-squares regression as shown in Equation 3.1. This fit is quite good, with a correlation coefficient of 0.998.

$$C_{dwing} = 0.056615(C_L^{3.0530}) + 0.0043454 \tag{3.1}$$

This expression will be used to express the total drag coefficient of both wings in conjunction with the wing/wing interference effects described in the following section.

3.1.3 Wing/Wing Interference Effects

Both Munk [45] and Prandtl [10] give expressions for induced drag for a biplane configuration. In an effort to preserve generality and for ease of computations, the

latter expression by Prandtl (given in Equation 3.2), derived by integrating the induced velocity in the downwash of each wing. In this expression, the subscripts 1 and 2 reference the upper and lower wings, respectively. L_1 and L_2 are determined by a comparison of the span of the lifting surfaces.

$$C_{Dinduced} = \frac{L_1^2}{q\pi b_1^2} + \frac{2L_1L_2\sigma}{q\pi b_1 b_2} + \frac{L_2^2}{q\pi b_2^2} \tag{3.2}$$

Values for σ can be obtained from an approximation given in Equation 3.3 given by [10] where *(G/b)* is the gap-to-span ratio.

$$\sigma = \frac{1 - 0.56(G/b)}{1.05 + 3.7(G/b)} \tag{3.3}$$

It is assumed that both wings are of the same span and aspect ratio (for simplicity), and hence the lift generated by each wing is similarly assumed to be equal. Hence, Equation 3.4 relation can be considered as an induced drag correction factor for an unstaggered biplane wing system with no decalage and similar spans and aspect ratios.

$$C_{Dbiplane} = \frac{L^2}{q\pi b^2}\left(\frac{1+\sigma}{2}\right) = \frac{L^2}{q\pi b^2}\kappa \tag{3.4}$$

Applying this expression, Prandtl [10] demonstrates that drag reductions of nearly 40% (as compared to a monowing of the same span and total loading) can be realized, albeit for a gap-to-span ratio of 0.5. The gap is not wholly unreasonable for the aircraft expected from this work, however, considering the relatively low wing loadings typical of aircraft (e.g., 2-4 lbf/ft^2, per common modeling experience) built at this scale, it does represent a more extreme case. The results of this expression are shown in Figure 3.3.

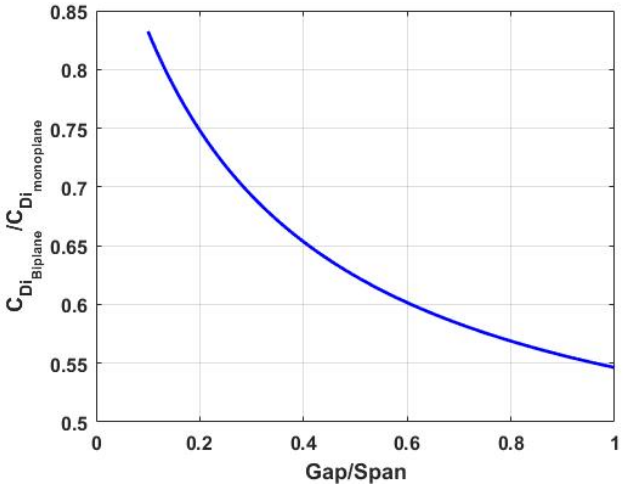

Figure 3.3: Induced drag comparison using Prandtl's correction [10]

Finally, it should be mentioned that Munk also provides an approximation for the mutual repulsion of the wings of a biplane system. The result of this expression is added to the expected wing airloads and is on the order of 10% of those loads [45].

3.2 Layout of Vehicle Components

In this framework, the aircraft was assumed to utilize 4 rotors that attach either to struts or wings, depending on the configuration (e.g., QBT or traditional quadcopter). For the QBT configurations, a set of 8 struts attach the wings to the fuselage in an "X" configuration. Four of these struts connect to the wing at the quarter chord, and the others attach to the trailing edge, where they also serve as landing gear. These struts are assumed to be slim, ellipsoidal prisms extending diagonally from the fuselage body to the wing surfaces. These struts attach to the fuselage in line with the fuselage center of gravity. A rudimentary model highlighting the various components considered in this model is shown in Figure 3.4.

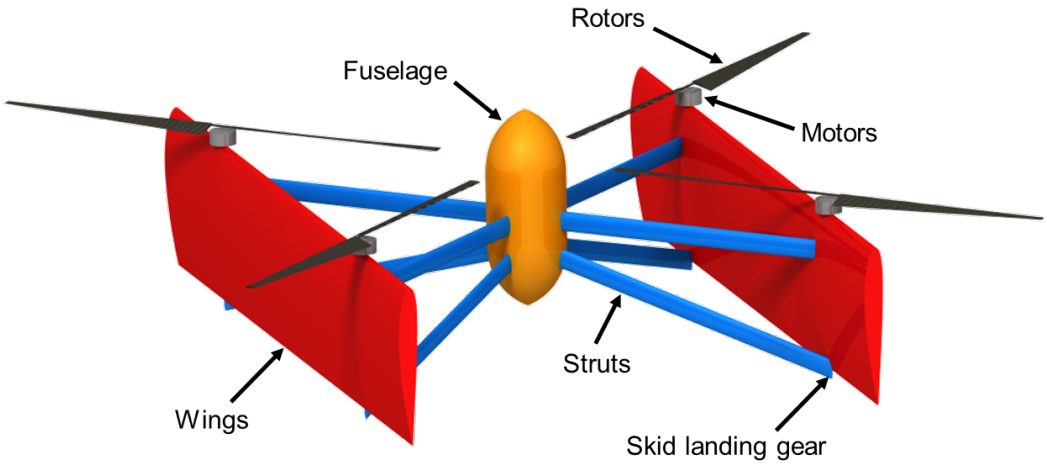

(a) External components

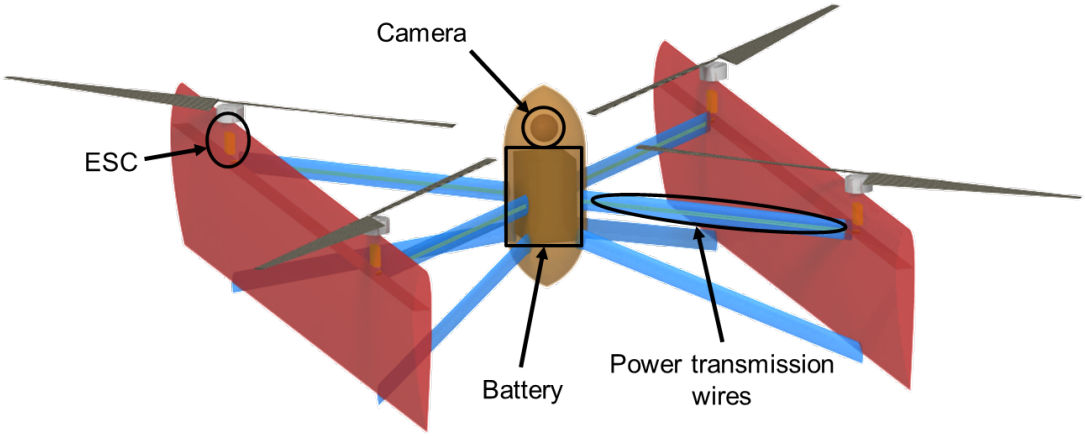

(b) Internal components

Figure 3.4: Design features of proposed aircraft

The fuselage is assumed to be an ellipsoid of a user-specified aspect ratio and is physically sized by both payload geometry, which is assumed to a be sphere, and the battery volume. Based on payload, an optics window will be provided in the fuselage. This is assumed to be of similar weight to the selected fuselage material.

Missing from this figure are various flight systems, such as autopilot and its associated sensor suite that facilitates navigation as well as sense-and-avoid capa-

bilities. The weight of these components has been estimated from the QBT design completed by Sidle et. al. [9] and includes both the sensors and computational capacity for flight in controlled and uncontrolled areas while in close proximity to obstacles.

An aside: in the initial sizing phase, it is still possible to return geometry to the user that is physically unfeasible (e.g., a blade incapable of carrying flight loads). This is particularly true of the rotors, whose blades are sized by disc loading and solidity. Hence, once a design has been run to convergence, the output designs are screened based on the feasibility of their rotor designs. Parameters considered in this screening include blade loading, aspect ratio, and root bending stress. Only those designs with a $C_T/\sigma \leq 0.14$ and an aspect ratio greater than 6 are retained from this preliminary sifting. Root bending loads are determined by assuming a triangular lift distribution on a rectangular, solid blade with a NACA 2412 cross section and a mean aerodynamic chord (MAC) determined by the blade span and aspect ratio. With this in hand, the von Mises equivalent stress is computed and compared to the material properties previously assumed.

Similarly, the initial design module imposes a constraint on the aircraft's maximum footprint. For purposes of this initial investigation, the maximum dimension of the vehicle must be less than 8 feet. Additional constraints can be added as desired. Following this screening, the basic rotor geometry and the most stringent power requirements in both edgewise and axial flight modes for these designs are then passed to the blade design module.

3.3 Component Weight Models

As this configuration is relatively new, little historical information exists from which to generate trends on the vehicle level. However, on the component level, more can be said. The radio-controlled aircraft market has produced a variety of motors, speed controllers, and batteries and a variety of manufacturers readily provide specifications for these items. Given this and the required work flow of the weight build up (as seen in Figure 3.5), the necessary relations for this study can be determined. This will be described in the following sections. For other commercially available components, such as power transmission wires, whose weight is dependent on both aircraft geometry and power requirements, best practices from the modeling community will be followed.

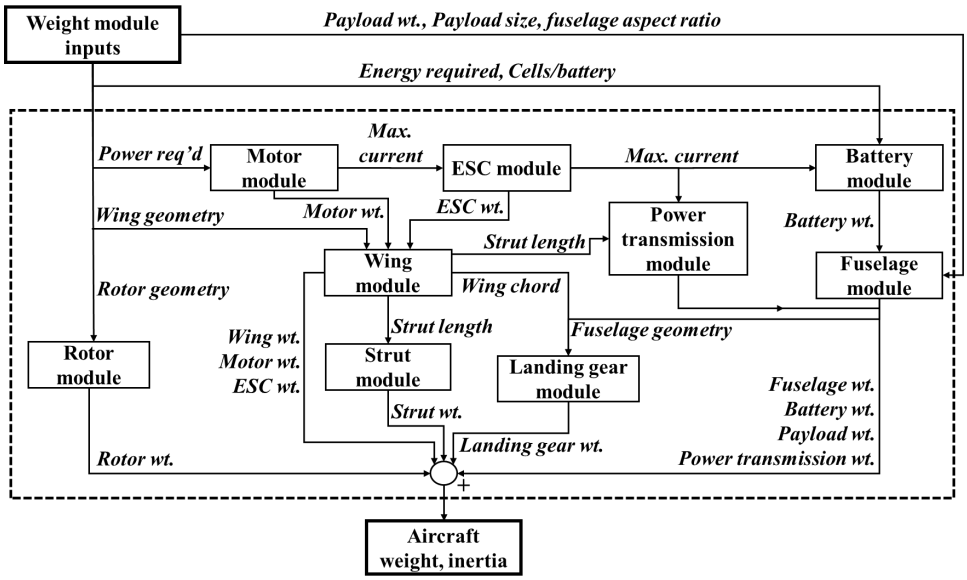

Figure 3.5: Weight module flowchart

However, there are a variety of components that are not so readily available.

For instance, rotors for model aircraft are also sold commercially, but the sizes required by this mission are likely to exceed those that are readily available. Similarly, as the rotor must be optimized for a combination of high speed edgewise inflow, axial inflow, and hovering flight, a custom rotor is desirable. Hence, the remaining components, being the wings, fuselage, struts, landing gear, and rotors, will utilize a method explicated by Chambers et. al. [48], wherein an assumed structural layout, material, and derived loads will be used to build up a weight estimate.

As a reference, the hovering and forward flight motor rotation rates specified for a given sizing iteration are also passed into this module. The whirl flutter avoidance criterion used requires all components to have a natural frequency $\omega > 1.1\omega_{motor}$ or $\omega < 0.9\omega_{motor}$ for 1/rev and 2/rev forcing frequencies.

3.3.1 Powerplant and Battery Weights

As empirical data is available for motors, ESCs, and batteries, those components will be sized utilizing nonlinear least-squares regressions fit to available component specifications. All regressions in this work were required to have a Pearson correlation coefficient greater than 0.85, though were typically 0.9 or higher. Details as to the specific expressions developed in this part can be found in Appendix A.1.

Given a power requirement, weight modeling begins by the selection of a motor capable of delivering said power. A rated maximum current is also predicted for this motor such that an appropriate ESC can be sized. The resulting models are applied in Figure 3.6 and compared against the database.

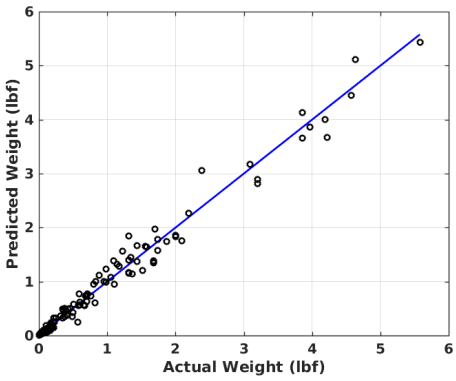

(a) Motor weight model

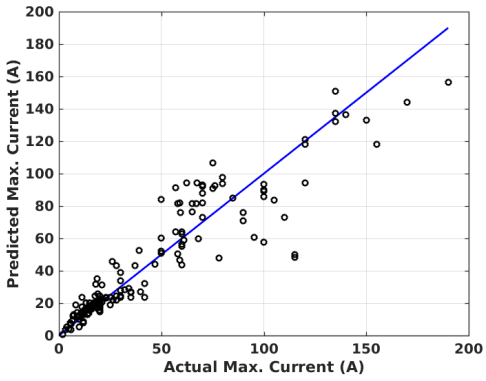

(b) Motor max. current model

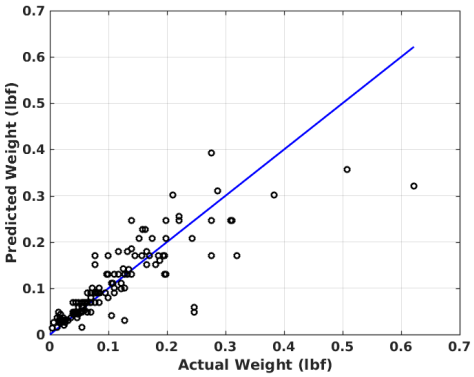

(c) ESC weight model

Figure 3.6: Model predictions for motor weight, motor maximum current, and ESC weight

Both the maximum current requirement and energy storage requirement (given as an input to the weight module) are passed to the battery sizing module. As LiPo batteries can be sensitive to high discharge rates (which are common to the propulsion systems of electric aircraft), a model incorporating both discharge rating and energy density must be formulated. To accomplish this, the battery weight is first predicted based on the energy storage requirement. Then, based on a relationship between energy capacity and discharge rating, the maximum current of the pack is predicted. If this is insufficient, the code utilizes the following logic.

As both energy capacity and discharge rating can be accommodated by adding additional batteries that are electrically in series, a particular quantity of packs will satisfy both requirements. However, it is desirable to increase battery weight only be the minimum amount required in order to meet both requirements. Hence, the first step is to compute the discharge rating of the lightest battery pack that will meet the requirement for total current output, or $W_{battery} = c_1(e_{reqd}/N_{reqdc})^{c_2}$, where c_1 and c_2 are empirical constants (given in Appendix A.1), $W_{battery}$ is the battery weight, e_{reqd} is the energy storage requirement, and N_{reqdc} is the number of packs required to meet the total current output requirement, given the discharge rating of the initially sized battery pack. This is computed using the models displayed in Figure 3.7 where it is compared against the battery database.

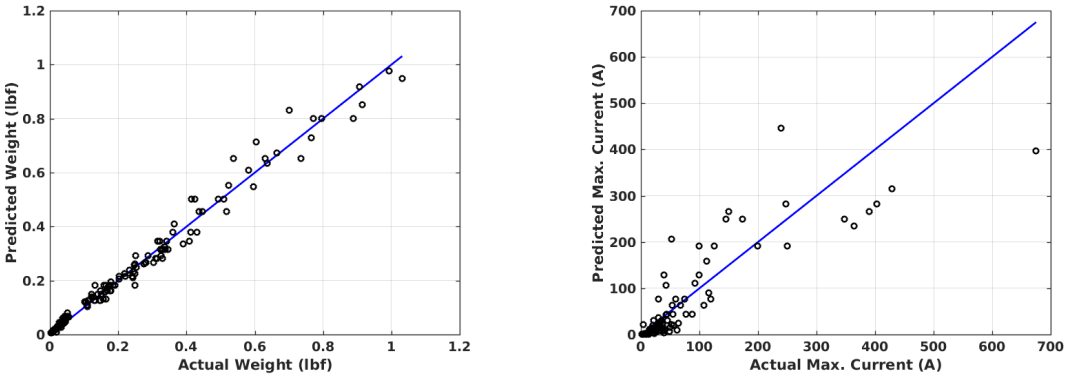

(a) Battery weight model

(b) Battery discharge model

Figure 3.7: Weight model predictions for battery weight and maximum battery discharge current

The discharge rating of this smaller pack is then predicted and compared to the requirement. If these new packs are found to have an insufficient current rating (or, in the aggregate, weigh in excess of the total required battery packs multiplied

by the originally estimated battery pack weight), then intermediate pack sizes are tested between the total packs required to meet the energy capacity requirement and the discharge requirement, respectively. The lightest pack that meets the discharge requirement is selected for use. Given the methodology used, any pack resulting from this sizing will automatically meet the energy storage criterion.

3.3.2 Power Transmission Weight

To compute the weight of the required power transmission wires, guidance is derived from the modeling community as the wire gauges specified for commercial use are well in excess of what is required for small-scale aircraft. This has led to an expression for wire thickness to be defined in terms of circular mils of wire per ampere of current, where a circular mil (or "cmil") is commonly defined as the area of a circle with a diameter of 1 mil (0.001 in). Based on standard practice, it is accepted that a wire cross section specified by 100 cmil/A will be sufficient. This also has been confirmed to comply with FAA Advisory Circular AC 43.13-1B [74].

Two conductors are required per ESC which run from the battery to the ESC. It is assumed that these will run from the centerline of the fuselage, up a given strut, and then out each motor along the quarter-chord of the wing and through its interior. In addition, to accommodate the proper phasing of power to the motor, three conductors are required to connect between each ESC/motor pair. This has been estimated as 10% of the rotor diameter to account of offsets motor mount location relative to the ESC due to blade flapping clearances.

3.3.3 Wing Weight

Data concerning structural elements is far more elusive, requiring a different methodology. This study utilizes a technique previously employed by Chambers et. al. [48], wherein the designer assumes a particular structural layout and material properties for a given component, such as a wing. As this aircraft is not only designed for a particular industry but is being developed in cooperation with a plastics injection molding firm, a candidate material has been independently selected: a carbon-filled polycarbonate. Material properties can be found in Appendix A.2.

In this tool, the wing is assumed to be a uniform, semi-monocoque structure, comprising of a single, vertical member at the quarter-chord and a thin, load-bearing skin. A representative image, for scale, is given in Figure 3.8.

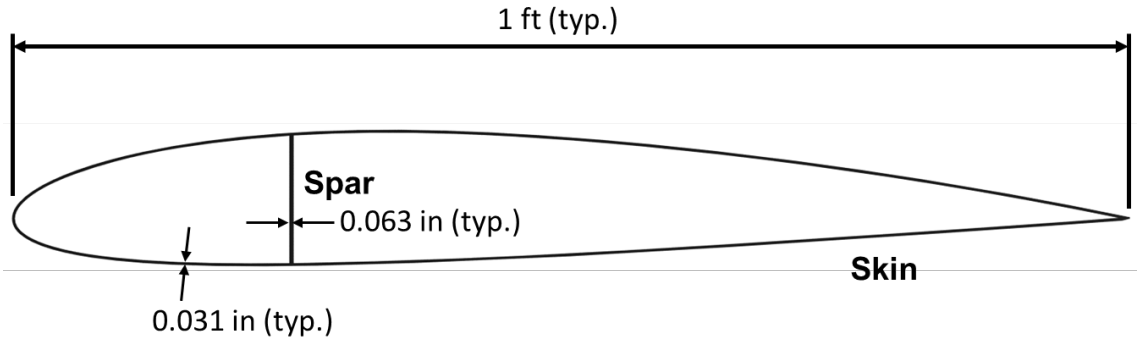

Figure 3.8: Scale representation of a typical wing cross section

Its sizing depends on 3 items: load capabilities, aeroelastic flutter, and whirl flutter. These can be counteracted by either modifying the mass distribution within the wing, strengthening the wing, or moving the wing's supports (the struts). For simplicity, this study only considers the latter two methods.

The aeroelastic flutter boundary is estimated utilizing the k-method as expli-

cated by Scanlan and Rosenbaum in [75] and solved by Hodges and Pierce in [76] with more modern techniques. This methodology solves a 2 degree of freedom system for the artificial structural damping in torsion and heaving, respectively. This damping results from the imaginary parts, ig_h and ig_θ for heaving and torsion, respectively, of Equations 3.5 and 3.6.

$$\left\{\mu\left[1-\left(\frac{\omega_h}{\omega}\right)^2(1+ig_h)\right]+\ell_h\right\}\frac{\bar{h}}{b}+(\mu x_\theta+\ell_\theta)\bar{\theta}=0 \tag{3.5}$$

$$(\mu x_\theta+m_h)\frac{\bar{h}}{b}+\left\{\mu r^2\left[1-\left(\frac{\omega_h}{\omega}\right)^2(1+ig_\theta)\right]+m_\theta\right\}\bar{\theta}=0 \tag{3.6}$$

Solving for the structural damping terms leads to the following expression, the so-called "flutter determinant," in which Z is substituted for the structural damping terms $(1+ig)$ in either expression, and σ is the ratio of the system's natural heaving frequency, ω_h, to the flutter frequency, ω. The aerodynamic forcing terms, ℓ_h and ℓ_θ, are determined via tabulated values of Theodorsen's lift deficiency function.

$$\begin{vmatrix}\mu(1-\sigma^2 Z)+\ell_h & \mu x_\theta+\ell_\theta \\ \mu x_\theta+m_h & \mu r^2(1-Z)+m_\theta\end{vmatrix}=0 \tag{3.7}$$

The solution of the complex cubic polynomial evolved from the flutter determinant yields complex roots for Z which are related to each of the heaving and torsional modes. The imaginary part of the solution represents the structural damping term, whereas the real part is related to the flutter frequency by the natural frequencies of the wing in heave and torsion. The flutter boundary is found by solving the equation for values of reduced frequency that correspond to tabulated values for Theodorsen's lift deficiency function. The boundary is found at the reduced frequency where the structural damping term vanishes. Due to the physical incon-

gruity of this problem, wherein mechanical dissipation and simple harmonic motion are proscribed simultaneously, the solution has little meaning at points above or below the flutter boundary. For purposes of this work, however, it is sufficient to define the flutter boundary for a proposed wing structure and ensure that it has not been violated. Hence, despite these limitations, Hodges and Pierce [76] as well as Mayuresh and Hodges [77] both note that the k-method is sufficient for this use, particularly in preliminary design. More detailed methods of determining aeroelastic flutter in biplane wings do exist, as discussed by McVicar et. al. [78] as well as Pons and Gutschmidt [79], and may be of interest to implement in future studies.

The wing's natural frequencies are computed utilizing a finite element formulation of the Rayleigh-Ritz method as shown by Bauchau and Craig [80]. These frequencies are also compared to the operating frequencies of the motors in both forward flight and hover to determine the wing's susceptibility to whirl flutter. In order to counter either eventuality (failure due to aeroelastic or whirl flutter), the wing strut connection points are moved to various test positions from 0.55 rotor diameters from the aircraft centerline to the wingtips. The struts attach to the wing at the quarter-chord and are assumed to not exert any pitching or heaving moments on the wing in this analysis. These attachment points are also assumed to be pinned in heaving and free in torsion. The motors, ESCs, and rotors are considered as "lumped" masses at the leading edge of the wing and are treated accordingly in the finite element formulation. Sectional properties are derived from an appropriate NACA x412 airfoil, where the camber is varied depending on the required lift coefficient in cruise.

Loads are computed by von Mises equivalent stress and the structure is thickened or thinned appropriately to allow for a suitable load factor. The minimum wall thickness is determined by the confluence of manufacturing limitations and the minimum thickness required to avoid flutter. In an effort to decrease weight, the skin thickness is varied at one half the rate of the spar thickness. The thickness of both elements are determined via the bisection method.

3.3.4 Strut and Landing Gear Weight

The struts, a set of ellipsoidal prisms extending from the fuselage to the wings, are sized similarly, although, for the sake of computational efficiency, they are considered to be stiff in torsion and so insusceptible to aeroelastic flutter. However, as an analytic shape, their natural frequencies are simple to generate and then compare against the operational frequencies of the motors to avoid whirl flutter. The struts are then sized accordingly so as to avoid coincidence with these forcing frequencies while resisting the anticipated loads.

The lower set of struts, those closest to the trailing edge of the wings, are utilized as skid landing gear. As previously shown in Figure 3.4a, these struts extend at least one inch (roughly 8% of the chord) beyond the trailing edge of the wings, allowing them to impact the ground prior to the aerodynamic surfaces. To accommodate landing loads, each strut is sized to withstand a 2g load with respect to the aircraft's maximum gross weight.

Given the location of these skids, the wing aspect ratios considered in this

study, and the wing/body separation necessitated by the rotor/rotor separation distances previously discussion in this part, rollover and tipover angles are inherently large: in excess of 45° for all configurations studied. Hence, they will not be considered by this sizing module.

3.3.5 Fuselage Weight

The fuselage is approximated as a hollow structure with a cylindrical midsection and conical ends. This structure is sized to accommodate the loads and physical size of both batteries and payload. The skin thickness is then varied to accommodate the resulting loads, using the bisection method to arrive at an optimal thickness. As this results in what is easily the stiffest structure on the aircraft, it is assumed to be insusceptible to flutter. The wing/fuselage struts are assumed to connect to the fuselage at its center of gravity and extend to the wing's quarter-chord at a spanwise location determined as previously described.

3.3.6 Rotor Weight

In comparison with these other models, the rotor model is left in a more simplistic form for the initial sizing. In this part, the module first computes cross sectional area of a NACA 2412 airfoil at the blade chord specified by specified rotor solidity, blade loading, and initialized GTOW. From this, the code computes the blade volume, given the rotor diameter. Given that the majority of blades on this scale are solid, the blade is assumed to be of uniform density and made from a

specified material, enabling its weight to be determined. Load characteristics of the blades are checked following design convergence as previously discussed, and, as the blade described here has very little definition (e.g., there is no specified chord or twist distribution at present), its vibration characteristics will be presently ignored.

3.4 Weight Model Validation

To validate this weight model, it is applied to the only existing QBT of significant scale: the prototype aircraft developed by Phillips et. al. [5]. While this aircraft was not developed for any particular mission, it is the only reasonable comparison possible at the time of writing.

As the weight modeling tool developed here has been implemented under a specific set of assumptions (such as structural layout, material, etc.), it is expected that the structural elements may not be able to be directly compared to the prototype aircraft. With this in mind, the following weight breakdown was computed utilizing the motor power specification, battery specifications, and geometry of the prototype aircraft given by Phillips et. al. [5]. Note that, due to categories in the weight breakdown given by Phillips et. al., the weight fractions listed here will not necessarily sum to unity. However, aggregated items can still be compared as has been done in Table 3.1.

As shown, the weight model developed here compares well with the prototype, save for the structural weight. This overpredicted structural weight is likely the result of (1) the use of a heavier material (a carbon-reinforced plastic) and (2)

Table 3.1: Weight breakdown comparison

Parameter	Phillips et. al. [5]	Weight Model Estimate
Takeoff weight	8.03 lbf	8.79 lbf
Structural weight	2.25 lbf	3.97 lbf
Powerplant weight	1.82 lbf	1.85 lbf
Battery weight	1.22 lbf	1.11 lbf

a different structural configuration that is more desirable for commercial aircraft in hostile environments. Whereas the prototype aircraft utilizes lightweight foam as well as fiber composites, these are not desirable for the offshore mission where the aircraft will be exposed to corrosive environments, nor for an aircraft that will be mass produced. This latter item is a concern in this study as a local plastic injection molding firm has shown interest in producing the aircraft as the design process, which is being advanced through this present work, continues.

Chapter 4: Vehicle Analysis Tools

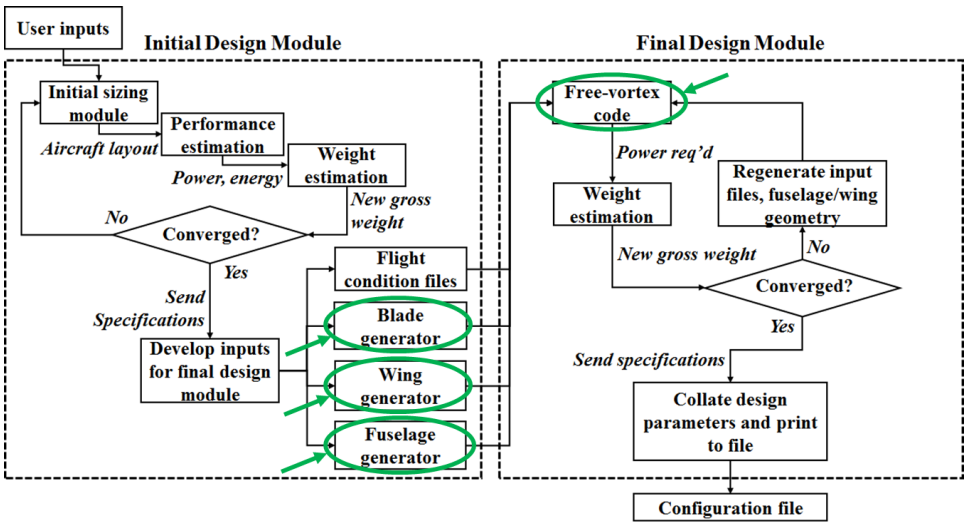

Figure 4.1: Flowchart for the integrated QBT design code

Following the design framework shown in Figure 4.1, the configurations selected by the previous chapter's preliminary design tool are now prepared for higher-order analysis. Specifically, this chapter addresses the highlighted components: the fuselage and wing geometry generators, a rotor blade generator, and a 3D, unsteady, inviscid panel code that will, in future work, be coupled to the free-vortex code specified in the design flowchart. This coupling will provide the designer with a rapid method of estimating interference effects for a complete vehicle.

However, while this incorporation of the free-vortex code into the present

design framework is not an objective of this present work, the groundwork for its implementation is laid here. Also, to ease said implementation, the free-vortex method implemented in the Parallelized Rotorcraft Analysis for Simulation and Design (PrasadUM) tool is specified as the target for this tool. Pertinent details of this tool and considerations for integrating with it will discussed in brief at the conclusion of the chapter.

4.1 Estimating Interference Effects: Unsteady Panel Method

The methodology employed here was originally explicated by Hess and Smith [81] for non-lifting bodies and, in a variant for lifting bodies, by a second publication by Hess [11]. Unlike lifting surface methods, panel methods directly account for the thickness and shape of body geometry by solving the potential flow equations via a distribution of singularity panels on the body surface. As described by Hess in [11], this methodology has significant impact on the pressure distribution for thick or highly cambered airfoils. An example calculation by Hess and Smith that demonstrates the necessity of so-called "panel methods" for these particular airfoils is shown in Figure 4.2. In this computation, a lifting surface method, utilizing a distribution of singularity filaments on the airfoil's camber line, is compared to a body-conforming panel method.

In the aforementioned works by Hess and Smith [11,81], a simplistic, low-order method is considered wherein quadrilaterals panels are assumed to contain piecewise constant singularity distributions. Higher-order formulations are briefly described

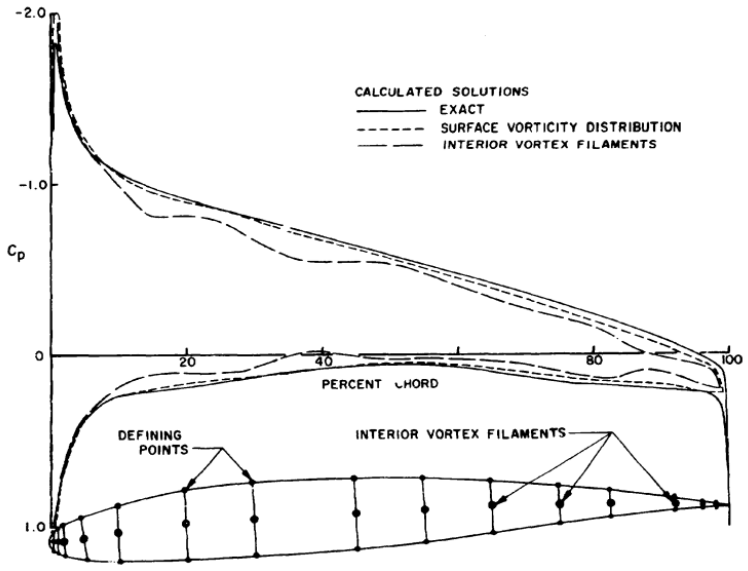

Figure 4.2: Comparison of the chordwise pressure distribution over a conventional, thick airfoil section at $\alpha = -6.9°$ [11]

by Erickson [12] as well as Plotkin and Katz [82] and implemented by Carmichael and Erickson [83] as well as Bristow and Hawk [84]. These higher order methods can vary the singularity distribution (e.g., linear or quadratic distributions instead of constant), as in the methods of Carmichael and Erickson or Bristow and hawk, or panel geometry formulations (e.g., parabolic or hyperboloidial panels instead of planar), as in Morino [85]. This is done to preserve C^0 or C^1 continuity in doublet strengths from panel to panel and so eliminate conceptual errors found in lower-order methods. Similarly, some higher order panel codes, such as described by Drela [86] and Erickson [12] feature corrections to account for laminar separation bubbles, compressibility effects, and even phenomena found in supersonic flows. Modeling flows containing such phenomena is wholly untenable for lower-order methods.

The two primary conceptual errors that are associated with low order panel methods are noted by Hess and Smith [11, 81] as well as Erickson [12]. Both errors

are concerned with the flow properties away from the panel centroid, the location where the local boundary conditions are imposed and the local flow velocity is made tangential to the body surface. While the boundary conditions can be wholly satisfied at this so-called "control point," they are typically not well satisfied away from this point for a constant strength singularity distribution, allowing flow to travel through the body surface. Furthermore, as, in various formulations, panel corners are assumed to lie wholly in-plane with each other (so as to simplify the integration of the panel's singularity distribution). This cannot be fulfilled for certain geometric profiles such as wing tip caps or tapered bodies.

To minimize the error produced by this, an averaged set of corner points is specified by Hess [11] such that the panel lies entirely in one plane near the true surface. However, the resulting geometry does not correctly describe the body contour, and, as in the first issue discussed here, allows for flow normal to the surface at the body surface. A visual of this is provided by Erickson in Figure 4.3. While violation of the no-through flow boundary condition could be an useful feature to describe active flow control if properly designed into a problem, it is not desireable otherwise.

However, as there is motivation for higher order panel formulations, Erickson [12] and Maskew [13] both critique these methods on their increased computational times and sensitivity to panel layout. Both authors suggest that, for subsonic flows, the shortcomings of lower-order methods can be overcome by use of an internal Dirichlet boundary condition and increasing panel density. The first of these items, an internal Dirichlet boundary condition, is in contrast to the external Neu-

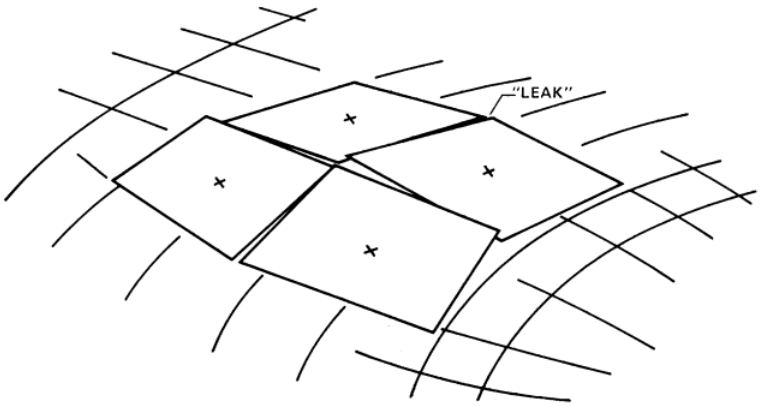

Figure 4.3: Example of flow "leakages" that occur due to poor surface approximation [12]

mann boundary condition utilized by Hess and Smith [81]. The external boundary condition is constituted by imposing a condition on the induced flow velocity at the surface such that the component of the flow velocity normal to the surface is equal to zero, or $\vec{v} \cdot \vec{n} = 0$. The proposed alternative, an internal Dirichlet condition, instead solves for a velocity potential on the body surface such that the induced velocity potential distribution along the inside of the body surface is equal to the surface velocity potential distribution. As a result, this also enforces the no through-flow condition, albeit in terms of a scalar quantity. The implementation and details of this method will be discussed in the following sections.

Also, as opposed to other, higher-order solutions, the inherent simplicity and low computational cost of these lower order methods allows them to be readily applied to highly nonlinear problems that require iterative solutions, such as the resolution of complete aircraft configurations which include high lift devices, powered engine nacelles, and flap and track fairings. An example of this is given in Figure 4.4, where Maskew [13] demonstrates the ability of a low-order method, similar to

what is developed here, here to accurately compute surface properties on a geometry that would, typically, elicit the problems previously described in this part in other low-order solvers. The specific example is an engine nacelle with a NACA 0005 cross section and operating at an angle of attack of $\alpha = 0°$.

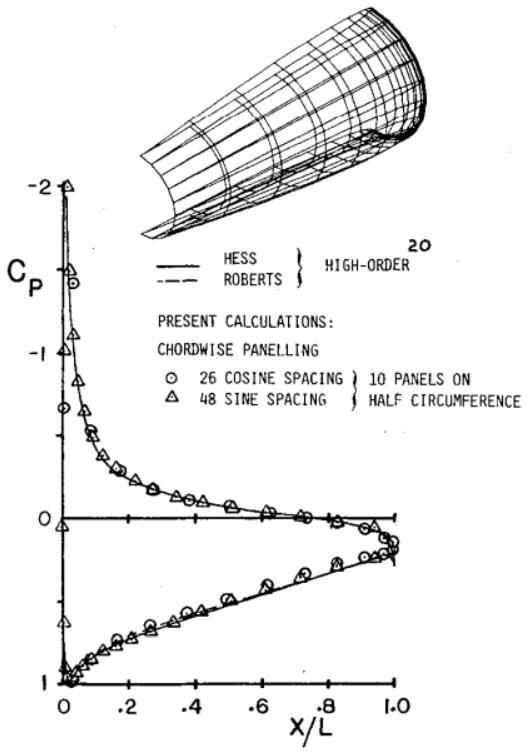

Figure 4.4: Computed pressure distribution over an engine nacelle [13]

Similar formulations have also been recently employed in hydrodynamics to model propellers, ship hulls, propellers operating behind a blockage, propellers operating in front of a rudder, or a body operating near or through a free surface. Examples of these problems are discussed by, Kinnas and Hsin [87], Han et. al. [88], Liu et. al. [89], He and Kinnas [90], and Tarafder [91].

Finally, to alleviate issues caused by the use of warped panels in lower-order methods, Newman [92] proposed a solution to the integral of a singularity distribu-

tion over a curvilinear panel using the Gauss-Bonnet theorem. By this, Newman enables the integral of various singularity distributions over any curvilinear panel surface to be directly evaluated. While Newman specifies that these panel surfaces must be bounded by straight edges and the panels themselves be quadrilateral or triangular, this present no additional difficulty to the implementation of these methods.

In the present usage, wherein the wings will be operating in close proximity to proprotors, and at relatively low Reynolds numbers ($Re < 500,000$, $Ma < 0.2$), it is expected that a low-order method will be sufficient and will yield benefits in terms of the wall-time required to develop a solution. This is further justified as the boundary layer development expected at very low Reynolds numbers (e.g., $Re < 100,000$), flow separation from flight at high angles of attack, and transonic effects are not expected in this present work.

4.1.1 Panel Method Basis and Formulation

With this in mind, the flow is modeled as follows. This solution to Laplace's equation is formulated in terms of Φ_i, the velocity potential inside of the body that is induced by the combined singularity distribution, Φ_∞, the far-field velocity potential, and Φ, the surface velocity potential required to satisfy Equation 4.1. This equation is an expression of the surface boundary condition, or the internal Dirichlet boundary condition from which this method derives it name, and it follows

from this that $\nabla\Phi \cdot \vec{n} = 0$ for $\Phi_\infty = 0$.

$$-\Phi = \Phi_\infty - \Phi_i \tag{4.1}$$

Solving for this boundary condition conveniently yields flow conditions at body surface directly. This solution is derived from Equation 4.2, which uses Greene's identity to solve the Laplace equation [91]. For reference, the vectors $\vec{r}$ and $\vec{n}$ give the displacement vector from the singularity control point (nominally the centroid of the panel associated with the singularity distribution, where the Dirichlet boundary condition is enforced) to a field point and the local surface normal vector, respectively. This formulation also includes the body surface, S_B, and the wake surface, S_W, wherein the latter surface is a no-force interface.

$$\begin{aligned}\Phi(P) = -\frac{1}{4\pi}\int_{S_B}\left\{\left[\frac{1}{\vec{r}}\nabla(\Phi-\Phi_i) - (\Phi-\Phi_i)\nabla\frac{1}{\vec{r}}\right]\cdot\vec{n}\right\}dS \\ + \frac{1}{4\pi}\int_{S_W}\left[\Phi\cdot\vec{n}\cdot\nabla\frac{1}{\vec{r}}\right]dS + \Phi_\infty(P)\end{aligned} \tag{4.2}$$

Furthermore, the singularity strengths must be selected such that they satisfy two additional boundary conditions. The first, a far-field condition, requires that the disturbance created by the body decays and vanishes in the far-field. This condition is automatically satisfied by the use of source and doublet singularities. Also, for lifting bodies with sharp trailing edges from which the flow must depart smoothly, the Kutta-Joukowsky condition (hereafter referred to as the Kutta condition) must also be satisfied. This condition requires the flow velocity to be finite at the trailing edge. While various implementations of the Kutta condition have been implemented by Hess [11], Morino and Kuot [93], Kinnas and Hsin [87], Ashby [94], Liu et. al. [89],

Willis [95], and others, these implementations generally utilize one of two methods. The first is the specification of a velocity vector at the trailing edge, the direction of which is defined by numeric experimentation. The latter method specifies a pressure difference of zero between the upper and lower surfaces of the trailing edge. It is shown by Hess [11] that the latter methodology is the more robust and accurate method, as it does not depend on the arbitrary specification of a velocity vector, allowing the flow to "choose" its own displacement vector. Hence, this method will be implemented here. The details of this condition, particularly for unsteady cases, is nontrivial and will be discussed in more detail in Section 4.1.5.

To summarize, all boundary conditions for this problem are listed as follows:

1. Surface boundary: $-\Phi = \Phi_\infty - \Phi_i$

2. Far-field boundary: $\lim_{\vec{r}\to\infty} \phi_{induced} = 0$

3. Kutta condition: $P_{upperTE} = P_{lowerTE}$

4.1.2 Wake Formation

It is important at this point to distinguish between panels located on wake and body surfaces. While the objective in this derivation is to provide an expression for the on-body velocity potential distribution, the proper formation of the trailed wake is of importance for estimating interference effects. Hence, the wake geometry is typically determined via one of two methods: time-stepping wake formation or wake relaxation. The latter technique, as used by Gaggero and Brizzolara [96] and shown in Figure 4.5, requires some initialized wake surface which is them relaxed

through successive iterations such that each panel lies tangent to the flow velocity at its centroid.

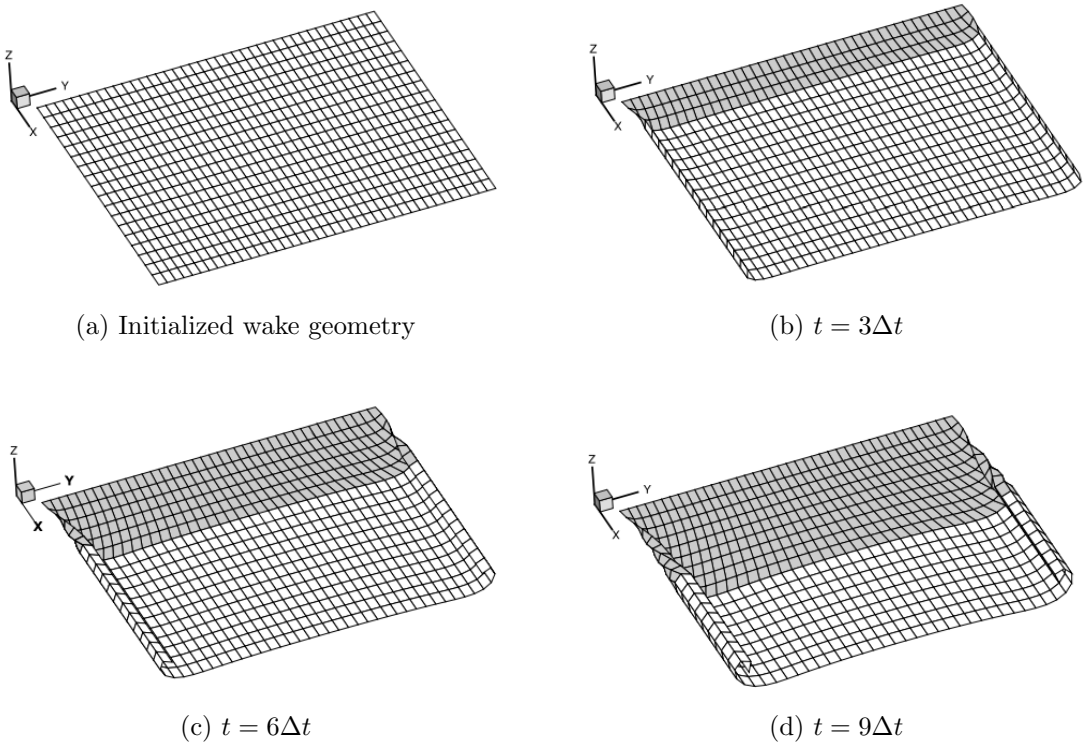

(a) Initialized wake geometry

(b) $t = 3\Delta t$

(c) $t = 6\Delta t$

(d) $t = 9\Delta t$

Figure 4.5: Areas in grey denote where the wake relaxation has been completed

This work instead utilizes a time-stepping wake model, similar to that which is implemented in the PMARC (Panel Method Ames Research Center) code [94]. Instead of requiring an initialized wake geometry, this model allows for a flexible wake sheet to be shed from the trailing edge of a sharp-edged body at each time step. This methodology is convenient for unsteady problems where no assumptions about the wake geometry can be made, although it is more susceptible to instabilities in the time marching process. As this solver is proposed for use in flows behind multiple proprotors, it is anticipated that this time marching methodology will be better suited to the problem at hand. Hence, the wake will shed in a time-accurate

manner and, as a no-force interface, convect with the local flow velocity. Details of this time-accurate wake convection will be described in a later section.

As each wake panel is shed from the surface, their singularity strengths are determined such that the Kutta condition is satisfied. The circulation shed into the wake satisfies Hemholtz theorem, written in Equation 4.3, and, as such, remains constant after its definition.

$$\frac{\delta\Gamma_{body}}{\delta t} = -\frac{\delta\Gamma_{wake}}{\delta t} \tag{4.3}$$

4.1.3 Method of Solution

In this implementation, distributions of both the doublet and source elements are assumed to be constant on a given panel. Hence, by defining the doublet and source strengths, μ and σ, as follows, the solution to the Laplace equation previously given in Equation 4.2 can be recast in terms of the singularity strengths themselves. Note that μ has been defined as the jump in the perturbation velocity potential from the interior of the body that is required to satisfy the no-through-flow boundary condition as specified by $\Phi_i = \Phi + \Phi_\infty = const$, which is equivalent to a more direct expression of the no through-flow condition when: $\nabla(\Phi + \Phi_\infty) \cdot \vec{n} = 0$. Since the value of μ is so defined, it completely defines the wake surface, allowing all source terms in the wake to be set to zero.

$$-\mu = \Phi - \Phi_i \tag{4.4}$$

$$-\sigma = \frac{\delta\Phi}{\delta n} - \frac{\delta\Phi_i}{\delta n} \tag{4.5}$$

Rewriting Equation 4.2 in terms of the boundary condition and the singularity strengths yields the following:

$$\Phi(P) = \frac{1}{4\pi}\int_{S_B+S_W} \mu \frac{\delta}{\delta\vec{n}}\frac{1}{\vec{r}}dS - \frac{1}{4\pi}\int_{S_B} \sigma\frac{1}{\vec{r}}dS + \Phi_\infty \tag{4.6}$$

On the interior of the body, the boundary condition can be rewritten as follows, which provides the basis of the problem's solution.

$$\frac{1}{4\pi}\int_{S_B+S_W} \mu \frac{\delta}{\delta n}\frac{1}{\vec{r}}dS - \frac{1}{4\pi}\int_{S_B} \sigma\frac{1}{\vec{r}}dS + \Phi_\infty = const \tag{4.7}$$

Or, upon application to a system of N_B body panels and N_W wake panels, wherein the integrals in Equation 4.7 are computed over discrete panels:

$$\frac{1}{4\pi}\sum_{j\,=1}^{N_W+N_B}\int_{S_B+S_W} \mu \frac{\delta}{\delta\vec{n}}\frac{1}{\vec{r}}dS - \frac{1}{4\pi}\sum_{j\,=1}^{N_B}\int_{S_B} \sigma\frac{1}{\vec{r}}dS + \Phi_\infty = const \tag{4.8}$$

Expressing the coefficients of σ and μ as matrices A and B, respectively, this equation can be simplified to the following statement.

$$\sum_{j=1}^{N_B} A_j\sigma + \sum_{j=1}^{N_B+N_W} B_j\mu + \Phi_\infty = const \tag{4.9}$$

These coefficient matrices are more commonly known as influence coefficient matrices. The values stored in these matrices correspond to the velocity potential induced at a given point by a source or doublet panel of unit strength. As the singularity influences scale linearly with singularity strength, the induced velocity potential at a given point due to all singularities in the model can be obtained via matrix multiplication. The coefficient matrices are organized as follows, where the matrix stores the influence of a singularity distribution on the kth panel on the control point of the nth panel. The magnitude of these influences, while important,

is not pertinent to the present discussion and will be discussed in Section 4.1.4.

$$A = \begin{bmatrix} A_{11} & ... & A_{1k} \\ ... & ... & ... \\ A_{n1} & ... & A_{nk} \end{bmatrix} \tag{4.10}$$

Hence, the solution to Equation 4.9 is that of a system of linear equations. However, as both σ and μ are undetermined and Φ_∞ is not specified, the solution for μ is not unique. Hence, utilizing the previously enumerated boundary conditions, the value of Φ_i is selected to match Φ_∞. Furthermore, the value of σ is specified as shown in Equation 4.11 [12, 82, 91].

$$\sigma_j = \vec{n} \cdot \vec{v}_\infty \tag{4.11}$$

This allows for a unique solution to be found for the surface doublet distribution via the solution to Equation 4.12. Note that the summations of singularity influences can include multiple bodies and wake regions without logical difficulty, provided that the the contributions of the local singularity distributions to all panels in the system are accounted for.

$$\sum_{j=1}^{N} A_j \sigma + \sum_{j=1}^{N} B_j \mu = 0 \tag{4.12}$$

As the flow is assumed to be inviscid, irrotational, and incompressible, the unsteady Bernoulli equation applies and can be used to solve for the pressure coefficient on a given panel. However, as a consequence of the internal Dirichlet formulation, this expression can be recast in terms of doublet strength instead of the local velocity since $\vec{v}_{local} = \nabla\phi = \nabla\mu$. These derivatives are found via a simple, first order numeric differentiation as suggested by Plotkin and Katz [82] as well as Tarafder [91].

As opposed to the Neumann formulation of this problem, this method saves considerable computational expense as the on-body velocity can be obtained directly from the singularity distribution determined via the solution to Equation 4.12 instead of computing the induced velocities at all on-body control points due to that singularity distribution. Via the unsteady Bernoulli equation, given in Equation 4.13, the following expression of the pressure coefficient, given in Equation 4.14, can be derived. It is assumed that the flow is incompressible and irrotational, leading to its expression in terms of velocity potential Φ, and that the pressure head induced by vertical displacement is small. The local air pressure is given as p and the fluid density as ρ. In the expression for the pressure coefficient, note that $\vec{v}_{\infty t}$ denotes the component of the freestream velocity parallel to a given panel at its control point.

$$\rho\frac{\delta\phi}{\delta t} + \frac{\rho}{2}\nabla\phi\cdot\nabla\phi + p = f(t) \tag{4.13}$$

$$C_p = 1 - \frac{|\vec{v}_{local} + \vec{v}_{\infty t}|^2}{|\vec{v}_\infty|^2} - \frac{2}{|\vec{v}_\infty|^2}\frac{\delta\Phi}{\delta t} \tag{4.14}$$

4.1.4 Singularity Influence Coefficients

To compute the coefficient matrices used in Equation 4.12, Newman [92] presents a method for computing the velocity potential induced by both source and doublet panels of unit strength. The expression the velocity potential induced by a doublet panel is given in Equation 4.15. Computationally, the arctangent function

specified for use in this expression must have the range $[-\pi/2, \pi/2]$.

$$\Phi_{doublet} = \frac{1}{4\pi} \sum_{i=1}^{N_{corners}} \left\{ atan\left[\frac{m_i\left[(x-\zeta_i)^2+z^2\right]-(x-\zeta_i)(y-\eta_i)}{zr_i}\right] - atan\left[\frac{m_i\left[(x-\zeta_{i+1})^2+z^2\right]-(x-\zeta_{i+1})(y-\eta_{i+1})}{zr_{i+1}}\right]\right\} \tag{4.15}$$

Where the coordinates ζ, η refer to the panel corners in a local coordinate system. This coordinate system is shown in greater detail in Figure 4.6. The point at which the velocity potential is induced, $(x, y, z)_{local}$, are relative to the panel reference frame. As shown in the Figure, m_{34} represents the slope of edge $\overline{34}$, d_{12} is the length of edge $\overline{12}$, and r_2 is the straight line distance from the second corner point to the target point at $(x, y, z)_{local}$

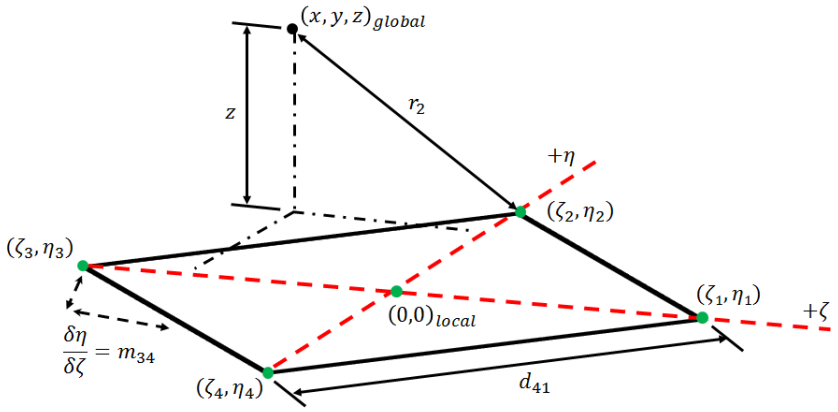

Figure 4.6: The panel coordinate system and the variables associated therewith

The values of m_i, r_i and d_ij, which will be utilized in Equation 4.19, are determined as follows:

$$m_i = \frac{\eta_{i+1} - \eta i}{\zeta_{i+1} - \zeta i} \tag{4.16}$$

$$r_i = \sqrt{(x-\zeta_i)^2 + (y-\eta_i)^2 + z^2} \tag{4.17}$$

$$d_i = \sqrt{(\zeta_{i+1} - \zeta i)^2 + (\eta_{i+1} - \eta_i)^2} \tag{4.18}$$

The velocity potential induced by a source panel is given by both Tarafder and Newman as follows [91, 92]. This statement, shown in Equation 4.19, is valid for an area bounded by straight lines and can be used for both quadrilateral and triangular panels.

$$\Phi_{source} = \frac{1}{4\pi} \sum_{i=1}^{N_sides} \left[\frac{(x-\zeta_i)(\eta_{i+1}-\eta_i) - (y-\eta_i)(\zeta_{i+1}-\zeta_i)}{d_i} ln \left(\frac{r_i + r_{i+1} + d_i}{r_i + r_{i+1} - d_i} \right) \right] \tag{4.19}$$

4.1.5 Implementing the Kutta Condition

While the source strengths are specified as discussed, the addition of a row of wake panels at the trailing edge, whose singularity strengths are, as yet, unknown, makes the system of equations underdetermined. The Kutta condition, which fully determines the system by relating the on-body singularity strengths to the strength of each individual wake panel, is commonly enforced through one of two methods.

The first, an explicit, linear formulation, was developed by Morino and Kuot [93]. Their formulation begins with Hemholtz's theorem, wherein the circulation shed into the wake must be equal and opposite to the circulation around the wing section at that spanwise station. As shown in Equation 4.20, the change in circulation along a chordwise section of a wing can be expressed in terms of the velocity potential distribution across that section. As a result of this, the net vorticity along the trailing edge sums to zero, requiring that the flow leave smoothly from that point.

$$\oint \vec{v} \cdot ds = \oint \nabla\phi \cdot ds = \oint d\phi \tag{4.20}$$

Morino and Kuot [93] then approximate this integral as the difference in doublet strengths between the upper and lower panels of the trailing edge (illustrated in Figure 4.7), allowing the wake panel at the trailing edge to be determined via Equation 4.21.

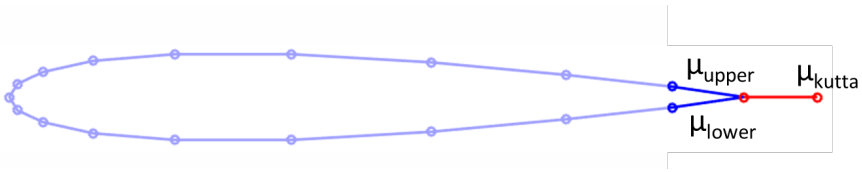

Figure 4.7: Graphical representation of the panels utilized for implementing the linear Kutta condition

$$\mu_{upper} - \mu_{lower} = \mu_{kutta} \tag{4.21}$$

Hence, whereas the solution to Equation 4.12 is a set of $(N+1)$ linear equations, where the $(N+1)$th unknown refers to the wake panels at the trailing edge of the body. In matrix form, this can be shown as follows. In this expression, subscripts of W correspond to the shed wake panels at the trailing edge.

$$\sum_{i=1}^{N+1} C_{ij}\mu_i = \begin{bmatrix} C_{11} & C_{12} & \dots & C_{1N} & C_{1W} & \\ C_{21} & C_{22} & \dots & C_{2N} & C_{2W} & \\ \dots & \dots & \dots & \dots & \dots & \\ C_{N1} & C_{N2} & & \dots & C_{NN} & C_{NW} \\ 1 & 0 & \dots & -1 & 1 & \end{bmatrix} \begin{bmatrix} \mu_1 \\ \mu_2 \\ \dots \\ \mu_N \\ \mu_W \end{bmatrix} \tag{4.22}$$

By replacing μ_W with $\mu_N - \mu_1$, or rewrite the coefficient matrix in Equation 4.22 in terms of d_{ij} as is expressed in Equation 4.23.

$$\begin{aligned} d_{ij} &= C_{ij} & i &\neq 1, N \\ d_{ij} &= C_{ij} - C_{iW} & i &= 1 \\ d_{ij} &= C_{ij} + C_{iW} & i &= N \end{aligned} \tag{4.23}$$

Hence, the $N+1$ equations are rewritten into a fully determined system of N equations. This methodology is also described in detail by Morino and Kuot [93], Plotkin and Katz [82], and Tarafder [91]. While this method is not utilized to compute the solution in this panel method implementation, it is used to initialize the nonlinear Kutta condition discussed in this part. The linear formulation of the Kutta condition has been only been shown applicable for a body undergoing limited motion in a simplified flow field, as noted in a seminal work by Kinnas and Hsin [87].

To provide for more interesting analyses, Kinnas and Hsin [87] instead propose a nonlinear implementation of the Kutta condition. While their motivation was to model propellers with highly skewed geometries that are immersed in nonuniform flow fields, it is expected that this present formulation will be utilized for bodies almost fully immersed in the wake of multiple rotors, providing similar motivation for a nonlinear implementation of this condition. A need for such a formulation in this work has been confirmed through numerical experimentation by the author wherein the Morino and Kuot [93] formulation failed to hold for a wing with a NACA 0012 cross-section (aspect ratio of 10, 40x40 panels) in a freestream oscillating at a relatively benign reduced frequency of 0.1 and an amplitude of 10°.

Various authors, including Willis [95], Liu et. al. [89], and Hess [11] explicate a nonlinear formulation that determines the strength of this trailing edge wake panel such that there is no pressure difference between the upper and lower panels of a given trailing edge station. To do this, the strength of each trailing edge wake panel, $[\mu]$, is adjusted in subiterations until this equal pressure condition is

satisfied. To relate the trailing edge pressure difference at each spanwise station, $[\Delta C_p]$, to the trailing edge wake panel (hereafter referred to as a "Kutta" panel), a Jacobian is utilized as shown in Equation 4.24. This is initialized through use of the linearized Kutta condition given by Morino and Kuot [93] to find the trailing edge pressure differences resulting from small perturbations of each wake panel's singularity strength. In this expression, the subscripts refer to the initialized values, *init*, and those values resulting from the perturbation, p.

$$J = \left[\frac{\delta(\Delta C_p)}{\delta\mu}\right] = \left[\frac{(\Delta C_p)_p - (\Delta C_p)_{init}}{\mu_p - \mu_{init}}\right] \tag{4.24}$$

In Newton-Rhapson iterations, as used by Willis [95] as well as Kinnas and Hsin [87], the inverse of this matrix must be computed at each subiteration prior to computing a doublet strength distribution, thus requiring $O(n^3)$ operations but delivering quadratic convergence as noted by Burden and Faires [97]. As computational expense is of greater concern for this problem than convergence time, Liu et. al. [89] propose the use of Broyden iterations instead. Broyden's method is a quasi-Newton method that requires only $O(n^2)$ operations per subiteration, albeit only delivering so-called "superlinear" convergence (i.e., slower than quadratic convergence, but faster than linear). This computational efficiency is obtained by replacing the Jacobian by an approximation matrix, A, whose inverse can be directly updated by the Sherman-Morrison formula, as given in Equation 4.25.

$$A_n^{-1} = A_{n-1}^{-1} + \frac{(([\mu]_n - [\mu]_{n-1}) - A_{n-1}^{-1}([\Delta C_p]_n - [\Delta C_p]_{n-1}))([\mu]_n - [\mu]_{n-1})^T A_{n-1}^{-1}}{([\mu]_n - [\mu]_{n-1})^T A_{n-1}^{-1}([\Delta C_p]_n - [\Delta C_p]_{n-1})} \tag{4.25}$$

Hence, the subiterations at each time step proceed as follows:

1. Compute trailing edge pressure differences ΔC_p at all spanwise stations

2. Update shed wake doublet strengths via $[\mu]_n = [\mu]_{n-1} - A^{-1}[\Delta C_p]$

3. Compute trailing edge pressure differences ΔC_p at all spanwise stations given the updated shed wake strength

4. If $\frac{1}{K}\sum_{i=1}^{K}|\Delta C_p|_i \leq 0.05$ (criterion suggested by [89]), the subiterations can be considered to have converged. Else, proceed to step 5

5. Update A^{-1} via Equation 4.25 and continue subiterations from step 2

4.1.6 Wake Convection

Once the strength of the shed wake is determined, it is shed in a time-accurate manner from the trailing edge of the body as determined by a boundary condition in the wake region. As the trailed wake represents a no-force surface, the panel corner points convect freely with the local flow velocity. This flow velocity is the summation of the freestream velocity and the velocities at a given panel corner that are induced by the previously determined singularity distributions in all body and wake regions. In order to remove singularities from the computation of the induced velocities, all doublet panels are modeled as vortex rings, a well-known equivalency for constant-strength doublet panels [13]. The vortex filaments comprising these rings are modeled as Lamb-Oseen vortices, yielding a smooth and continuous representation of the induced velocity profile, even near the center of the vortex, as opposed to the singularity or Rankine models. For clarity, a 2D expression of this

velocity profile is given by Figure 4.8.

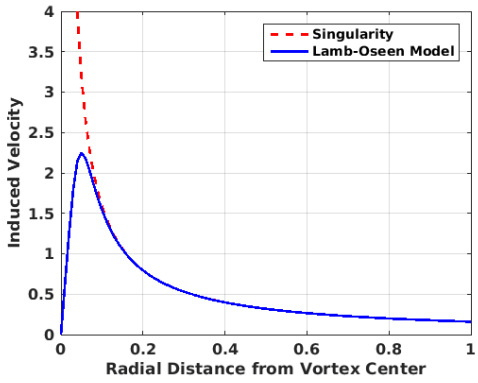

Figure 4.8: Velocity induced by a 2D Lamb-Oseen vortex

This 2D velocity profile, V_θ, is described by Equation 4.26. In this expression, the vortex strength is given as Γ, the distance of the point of interest to the center of the vortex is given as, r, and the radius of the viscous vortex core is r_c. Variations in the core radius with respect to time, t, are modeled using Equation 4.27 where the Lamb-Oseen constant is given as $\alpha = 1.25643$ and ν_∞ in the kinematic viscosity of the working fluid [98].

$$V_\theta = \frac{\Gamma}{2\pi} \frac{r}{(r^4 + r_c^4)^{0.5}} \tag{4.26}$$

$$r_c = \sqrt{4\alpha\nu_\infty t} \tag{4.27}$$

Hence, the induced velocity at a point due to each vortex filament comprising the quadralateral or triangular (for some on-body panels) rings can be determined via application of the Biot-Savart Law, which is given in Equation 4.28.

$$\vec{V} = \int \frac{\Gamma}{4\pi} \frac{dl \times r}{|r|^3} \tag{4.28}$$

The induced velocities due to source panels are derived by Newman [92] using the

Gauss-Bonnet theorem.

$$u_{source} = \frac{1}{4\pi}\sum_{i=1}^{4}\frac{\eta_{i+1}-\eta_i}{d_i} ln\left(\frac{r_i + r_{i+1} - d_i}{r_i + r_{i+1} + d_i}\right) \tag{4.29}$$

$$v_{source} = \frac{1}{4\pi}\sum_{i=1}^{4}\frac{\zeta_{i+1}-\zeta_i}{d_i} ln\left(\frac{r_i + r_{i+1} - d_i}{r_i + r_{i+1} + d_i}\right) \tag{4.30}$$

$$\begin{aligned} w_{source} = \frac{1}{4\pi}\sum_{i=1}^{N_{sides}} \Bigg\{ & atan\left[\frac{m_i\left[(x-\zeta_i)^2 + z^2\right] - (x-\zeta_i)(y-\eta_i)}{z r_i}\right] \\ & - atan\left[\frac{m_i\left[(x-\zeta_{i+1})^2 + z^2\right] - (x-\zeta_{i+1})(y-\eta_{i+1})}{z r_{i+1}}\right]\Bigg\} \end{aligned} \tag{4.31}$$

Singularities in the induced velocities computed by these expressions are avoided by adjusting the input coordinates such that they lie outside of the forcing panel by 5% of the local panel side length, as shown in Figure 4.9. For continuity, however, the coordinates utilized for the position updates in the time marching method discussed next remain unchanged from the physical coordinates of the model.

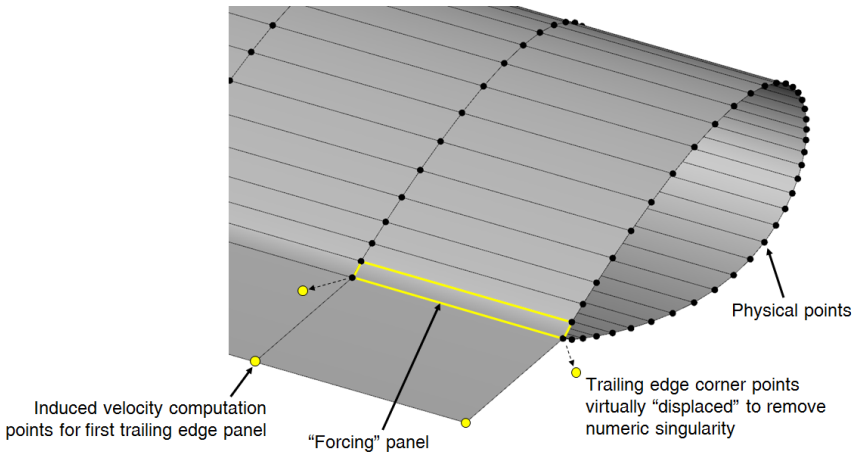

Figure 4.9: Points shown in yellow used for induced velocity computation. Displacements are exaggerated for clarity

The wake panels are then convected according to an explicit, 3rd order Runge-Kutta method. This is given in predictor-corrector form as follows. The interme-

diate velocities, $\widetilde{\vec{v}}$ and $\hat{\vec{v}}$ are determined by computing the induced velocity at the intermediate position vectors with which those velocities are associated.

$$\widetilde{\vec{r}} = \vec{r}_{n-1} + \vec{v}_{induced}\delta t \tag{4.32}$$

$$\hat{\vec{r}} = \vec{r}_{n-1} + \frac{\delta t}{4}(\vec{v}_{induced} + \widetilde{\vec{v}}) \tag{4.33}$$

$$\vec{r}_n = \vec{r}_{n-1} + \frac{\delta t}{6}(\vec{v}_{induced} + 4\widetilde{\vec{v}} + \hat{\vec{v}}) \tag{4.34}$$

Following wake convection, new shed wake panels are formed by connecting the corner points of the newly convected wake panels to the trailing edge of the body from which they convected.

4.1.7 Panel Method Validation

In this section, the panel method is applied to both steady and unsteady flow problems. The results from the first case, a steady state freestream at varied angles of attack, can be seen in Figure 4.10 where the chordwise pressure distribution calculated in the panel code is compared against the pressure solution computed by TURNS2D, a computational solver developed at UMD. This solver, successfully developed for application to transonic and high Reynolds number flows, has also been successfully applied to low Reynolds number problems by Winslow [47] and Yang [99] using a low-Mach preconditioner. In recent work, an alternative low-Mach correction published by Reiper [100], which scales the velocity terms with respect to Mach number, has been incorporated to increase the robustness and accuracy of the solver in these low-speed flow regimes. By way of methodology, this solver utilizes a dual-volume approach to solve the Reynolds Averaged Navier Stokes (RANS)

equations. Inviscid fluxes are computed utilizing a third-order MUSCL scheme, whereas viscous fluxes utilize a second-order central differencing scheme. Turbulence is modeled via an implementation of the Spalart-Allmaras equations. The steady problems posed here are solved via an Euler implicit time marching scheme with matrix inversions performed via the lower-upper symmetric Gauss-Seidel method.

As can be expected for low Reynolds numbers and attached flows, the code shows good agreement with the higher order model for lower angles of attack. While the results from an 80x2 panel case (80 panels in the wrap direction, 2 panels along the span) are shown here for ease of display, it is worth mentioning that cases utilizing 40x5, 40x10, 40x15, and 40x20 panels demonstrated similar results at midspan sections. This reduced scale case has shown good equivalency to the airfoil case in addition to significant savings in computational cost, hence its use here. Through numerical experimentation, a time step of 0.008 was found to be appropriate. For the high angle of attack case ($\alpha = 8°$) in Figure 4.10c, the suction peak was not well resolved by the 80x2 panel model. To better resolve the peak, a 130x2 panel model was utilized for this case. The computed pressure distributions shown here for a NACA 0012 at a Reynolds number of 159,000 are compared to steady-state pressure distributions computed by TURNS2D [101]. All panel solutions were computed over 800 iterations a time step size of 0.008.

While these models do result the lift distribution well, it should be noted that, as can be expected of an inviscid code, they significantly underpredict drag when compared to the RANS solution. Various viscous corrections may be able to account for this if implemented in future work.

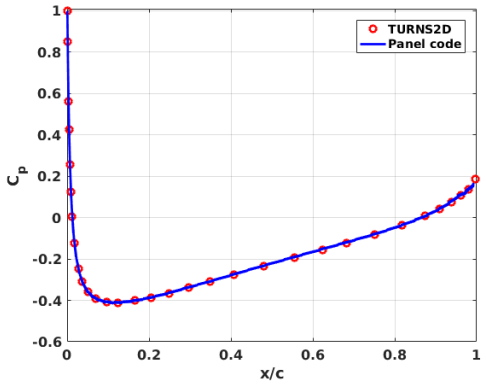

(a) $\alpha = 0°$

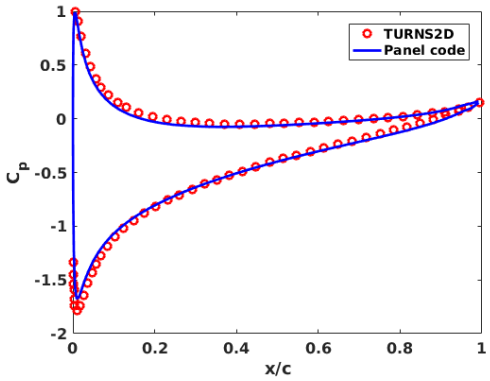

(b) $\alpha = 5°$

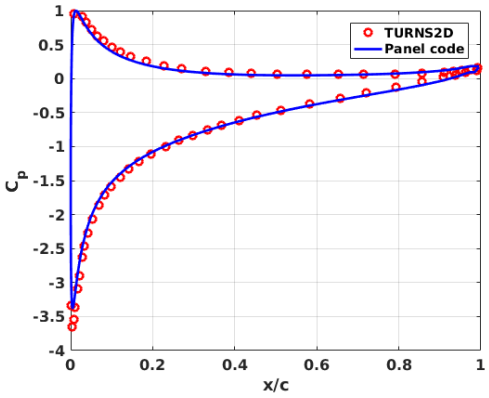

(c) $\alpha = 8°$

Figure 4.10: Comparison of computed steady-state pressure distributions to TURNS2D

To visualize the wake effects modeled by this code, a 40x80 panel wing (with uniform spanwise spacing) is utilized. This wing is specified to have an aspect ratio of 10, and a chord equal to unity. The result of this study are shown in Figure 4.11 after 300 time steps ($\Delta t = 0.001$) for a Reynolds number of 159,000 and an angle of attack of 5°. In the figure, body and wake edges have been highlighted for clarity. As shown, the wingtip and starting vortices have both been modeled by the code. However, while the starting vortex can be adequately resolved with a minimum of wrapwise panels, the resolution of the wingtip vortices varies dramatically with

spanwise panel density, which modifies both the degrees of freedom available for panel rotation as well as the accuracy of the spanwise pressure distribution. In this study, no model with less than 80 spanwise panels was able to capture the tip vortex rollup. This was true of models with stretched (using Vinokur's [102] hyperbolic tangent stretching) and uniform grids in the spanwise direction.

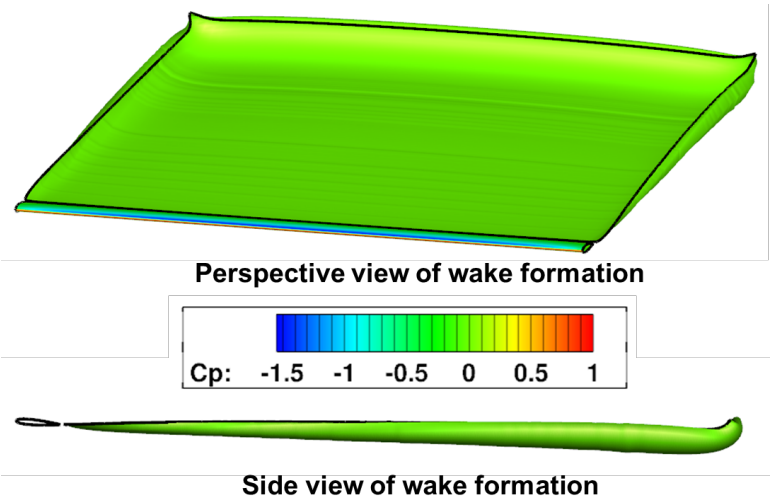

Figure 4.11: Tip and starting vortex rollup

Similarly, to demonstrate the efficacy of the code for unsteady flows, the panel code is utilized to analyze the case of an airfoil in an oscillating freestream. For comparison, empirical results from Plotkin and Katz [82] (lift and pitching moment) as well as Leishman [103] (drag) are utilized, as well as predictions for a flat plate developed by Theodorsen and elucidated by Leishman [70]. In all cases shown, the angle of the freestream relative to the airfoil chord line is varied according to $\alpha = \alpha_{steady} + \theta_{amp} sin(\omega t)$. For the reference case, the oscillatory frequency, ω, is determined by the reduced frequency $k = \omega b / v_\infty$, where b is the semi-chord of the wing, and v_∞ is the freestream velocity.

In the empirical cases shown below, the pitching amplitude is given as $\bar{\alpha}$ and the steady-state angle of attack as α_s. Each case was run for two complete cycles, or until the aerodynamic forces and moments exhibited a periodic variation using a freestream velocity of 25 ft/s and a time step of 0.001. The results of these cases are shown in Figure 4.12.

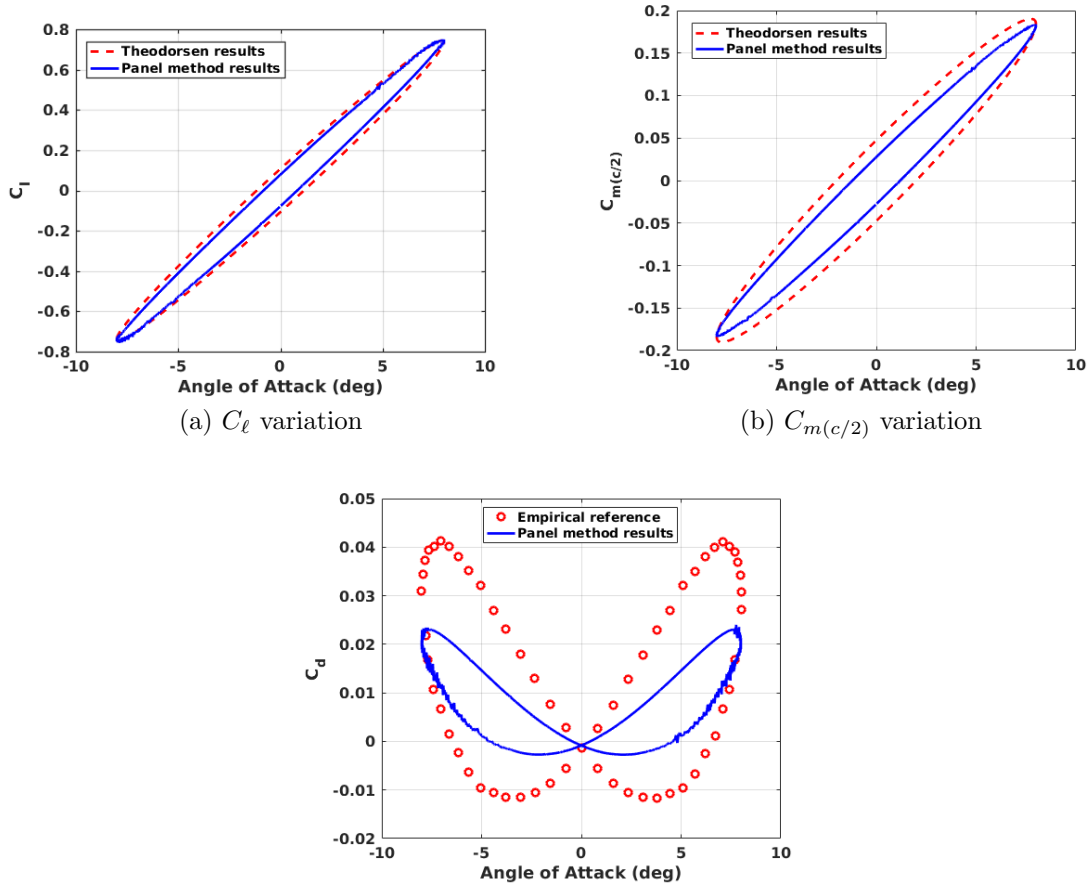

(a) C_ℓ variation

(b) $C_{m(c/2)}$ variation

(c) C_d variation [103]

Figure 4.12: Comparison of unsteady results: $k = 0.0941$, $\alpha_s = 0°$, $\bar{\alpha} = 8°$

While the lift result compares well with the references, the phasing and magnitude of both the pitching moment and pressure drag predictions are noticeably different from the experimental values. To check if this is merely a numerical ar-

tifact (as opposed to a limitation of the method), the effect of time step size was investigated for reduced frequencies of $k = 0.3$ and $k = 1.0$. In the former case, the time step was reduced by a factor of 0.5, and, in the latter case, by a factor of 0.1. As shown in Figures 4.13a and 4.13b, the time step size does not appreciably factor into the differences in magnitude previously shown.

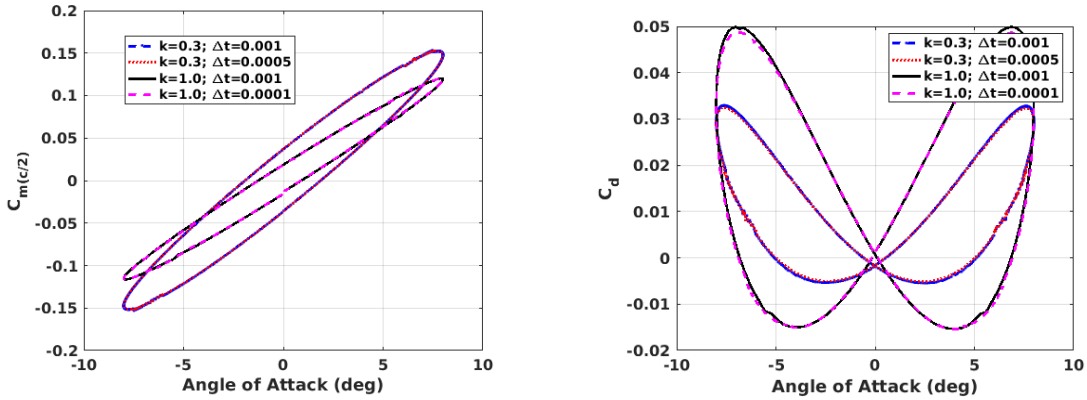

(a) $C_{m(c/2)}$ (b) C_d

Figure 4.13: Effect of Δt on $C_{m(c/2)}$ and C_d

However, in a larger comparison of pitching moment and lift amplitude, encompassing reduced frequencies from $k = 0$ to $k = 1$ are shown in Figures 4.14a and 4.14b, the panel method demonstrates good agreement with predictions made using Theodorsen's approximations for lift and pitching moment (as given by Equations 4.35 and 4.36). These expressions are given by [70] for an airfoil undergoing oscillations in angle of attack. In these expressions, Theodorsen's lift deficiency function is represented by $C(k)$.

$$C_\ell = 2\pi \left[C(k) + i\pi k\right] \bar{\alpha} e^{i\omega t} \tag{4.35}$$

$$C_{m(c/2)} = -i\frac{\pi k}{2}\bar{\alpha}e^{i\omega t} + \frac{C_\ell}{4} \tag{4.36}$$

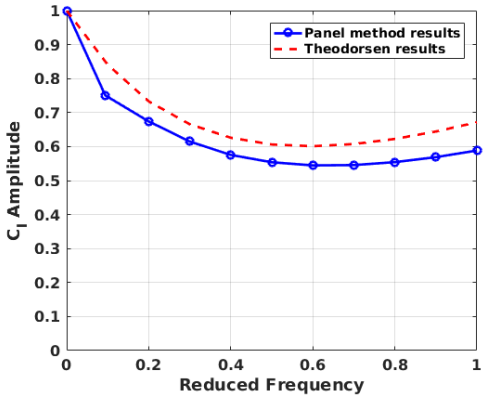

(a) Lift amplitude

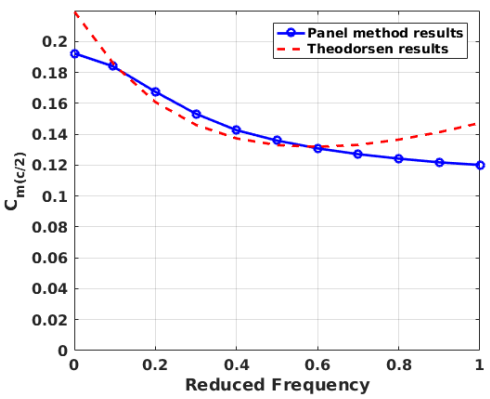

(b) Pitching moment amplitude

Figure 4.14: Comparison of panel method results to Theodorsen predictions

Furthermore, as the panel method utilizes a surface mesh to locate the singularity distributions, it should be able to predict thickness effects that Theodorsen's theory, as it is based upon a flat plate airfoil, cannot. This is evident in Figure 4.15 where, as airfoil thickness is reduced, the pitching moment results recover the pitching moment amplitude and phasing predicted by Theodorsen.

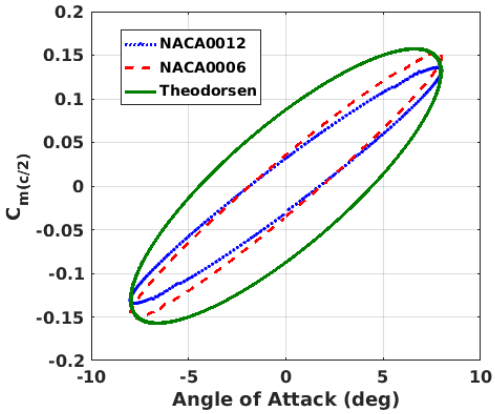

Figure 4.15: Effect of thickness on $C_{m(c/2)}$ at $k = 0.5$

To demonstrate the code's ability to resolve biplane interference effects, the

code was used to compute the lift and drag production from a pair of identical, wings with a NACA 0012 cross section in a biplane configuration. For this study, a 40x20 panel mesh was used for each wing, spaced at a 8 chords from each other in the vertical direction with no decalage or stagger. These results were compared to the results of both an isolated wing of equal span, as shown below in Table 4.1. As expected, the panel code captures the induced drag savings when migrating from a single wing to a biplane configuration with the same total loading and wing planform. It is also worth noting that, as predicted by Munk [45], the panel code predicts that each individual wing of the biplane configuration will have a lift coefficient 93% that of an isolated wing in a similar flow field. While this is greater than the lift reduction predicted by Munk (which is a $< 1\%$ reduction in lift), it does indicate that the panel method is capable of resolving certain trends associated with the biplane configuration.

Table 4.1: Biplane simulation

Configuration	Span	Chord	Gap	Angle of Attack	C_L	C_D
Isolated wing	10 ft	1 ft	N/A	5°	0.439	0.00853
Isolated wing	10 ft	1 ft	N/A	8°	0.820	0.0308
Biplane	10 ft	1 ft	8 chords	5°	0.820	0.0189

4.2 Wing/Body Generators

The fuselage geometry is assumed to be relatively simplistic and is modeled as a cylinder capped on either end by symmetrical surfaces of revolution formed by Bézier splines. This cylinder is sized to fit both payload and batteries, using an

assumed battery volume density and payload size. As the mission aims to provide a means of visual inspection, the payload has been selected to be the Starklite 200, a 2-axis gyro stabilized gimbal containing a high-definition video camera, thermal imaging camera, and rangefinder in a package that is approximately 3.5 inches in diameter [104]. It is assumed that this will be contained within an optics bay at the "nose" of the fuselage (also the top of the fuselage in a hovering frame of reference).

Generation of the wing geometry is more complex. While the user can select a particular airfoil, including any NACA 4-series airfoil, the code will, by default, automatically select the airfoil according to the required cruise lift coefficient computed by the initial design module. To do this, a set of 4 airfoils have been pre-selected for use. Specific profiles are utilized by the code such that, the airfoil selected will be operating within 5° of its maximum lift to drag angle of attack to produce the required lift coefficient. Profiles selected for this include the NACA 2412, 4412, 6412, Wortmann FX-63-137, and Selig 1223.

While coordinate sets for the default airfoils are provided with the code, they are "generic" coordinate sets procured either from the airfoil database maintained by the University of Illinois at Urbana Champaign [105] or from XFLR5, an open-source aircraft configuration analysis tool [106]. As such, these datasets do not necessarily have provisions for certain features desired in this 3D geometry generator. For example, for a smooth wing tip cap, it is desirable that there are an equal number of points on the upper and lower surfaces of the airfoils. To provide for this consideration as well as to ensure a favorable point distribution, the airfoil surfaces given by the initial coordinate sets are re-discretized utilizing piecewise monotonic

cubic interpolation splines constructed from the given coordinates.

The methodology behind using these splines for interpolation is described by Fritsch [107] and are used with a 3rd order weighted slope correction given by Aràndiga [108]. Point distributions are created using Vinokur's [102] hyperbolic tangent stretching function. Spanwise coordinate distribution is handled by either a simple uniform stretching function or Vinokur's hyperbolic tangent stretching. To generate a circular tip cap, it is desirable to use a cubic Bézier spline owing to the simplicity of its implementation in this particular setting as opposed to the splines described by Fritsch [107].

4.3 Blade Design Module

In order to integrate with PrasadUM, a rotor geometry must be specified. To accomplish this task, a rotor design module has been created to specify rotor twist, collective pitch, taper, and tip speeds for a selected aircraft configuration from the preliminary design module.

4.3.1 Rotor Modeling

This module is constructed around the linear inflow model of Pitt and Peters as described by Leishman [70]. This inflow model, while not as desirable as the radially-variant inflow allowed by blade-element momentum theory, allows for edgewise flight conditions, which are expected to be of interest in future studies. The Pitt-Peters model approximates the convected wake angle, χ, at a given vertical and horizontal

advance ratio, μ_z and μ_x, respectively, and provides a correction to the inflow with respect to azimuth, as shown in Equation 4.39.

$$\chi = atan\left(\frac{\mu_x}{\mu_z + \lambda_{hover}}\right) \tag{4.37}$$

$$k_x = \frac{15\pi}{23} tan\left(0.5\chi\right) \tag{4.38}$$

$$\lambda_i = \lambda_0(1 + k_x r\cos(\psi)) \tag{4.39}$$

Once values of the inflow are computed the solver determines the local angle of attack, Reynold's number, and Mach number, referencing airfoil tables for the NACA 23012 airfoil. This cross section will be assumed throughout the remainder of the design process. The expected maximum blade MAC, 2 in, was determined via numeric investigations to typically exceed the chord predicted by the preliminary sizing code. Furthermore, to prevent the formation of shocks and other transonic effects, the maximum tip Mach number is limited to 0.5. Utilizing airfoil tables to compute sectional aerodynamic properties, the code will optimize the rotor twist, taper, collective pitch, and tip speed for minimum energy usage with respect to both of the flight modes considered. As the Pareto frontier emerges from the analysis, the module automatically selects the design point that provides the greatest energy savings for the flight conditions analyzed without exceeding the airfoil's stall boundary.

However, as little data is available for cambered airfoil performance over a range of relatively low Reynolds numbers, the aforementioned airfoil tables have been calculated specifically for this application utilizing TURNS2D [101]. For the cases discussed here, an O-mesh with 141 wrapwise points and 401 wall-normal

points was utilized. In this present work, the range of expected Reynolds numbers is 40,000 to 580,000, as determined by expected rotor blade chords and tip speeds. Furthermore, for axisymmetric flight conditions, it is not expected that, for the desired rotor, the blade sections will be operating in a deep, post-stall region. Hence, for use in the sizing analysis, a CFD solution is only computed over the angle of attack range of -18°$\leq \alpha \leq$ 18°. Beyond this, the CFD solution is linearly blended into the theoretical lift and drag solutions for a flat plate, transitioning completely to the flat plate solution by $\alpha = \pm 25°$. This is anticipated to suffice for the axial flow cases that are of significant interest, however further characterization will be required for cases with significant edgewise flow.

Furthermore, based on the designer's choice, the module can operate in both fixed-pitch and variable-pitch modes, wherein it will generate proprotors optimized for fixed- and variable-pitch blades, respectively. A summary of rotor figure of merit and propulsive efficiencies for various rotor configurations and hub types are shown in Figure 4.16 for a QBT configured aircraft flying an offshore wind inspection mission, as discussed in the previous chapter.

While the benefit of a variable collective is clearly evident in the representative plots shown in Figures 4.16b and 4.16a, it may be precluded by scale and manufacturing limitations. Based upon flight condition, however, it may be impossible to achieve a desirable propulsive efficiency and figure of merit through a fixed pitch blade that is trimmed utilizing tipspeed alone. This consideration, as it reflects a design decision (particularly on this scale) and does not necessarily follow from the development of the design itself, will be left as an input. As noted, however, it is

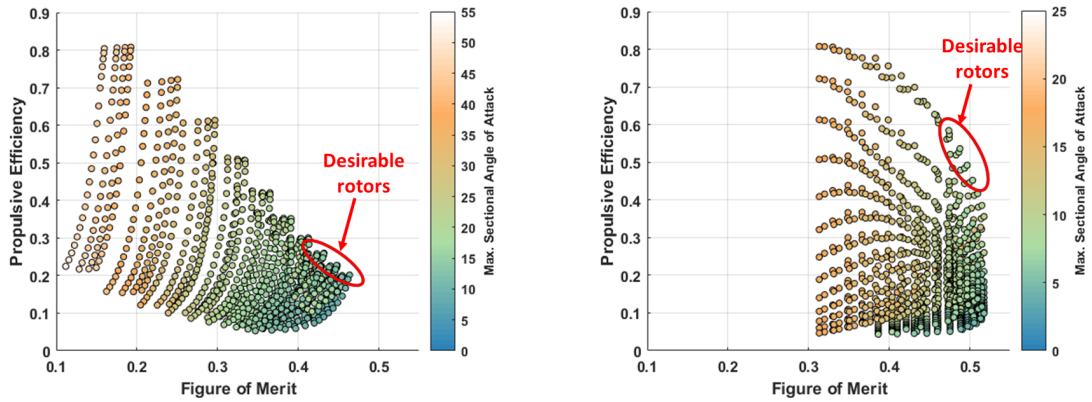

(a) Fixed pitch rotors (b) Variable pitch rotors

Figure 4.16: Output of rotor design tool

much easier to design a high-efficiency rotor for both hover and axial flight if variable collective is allowable. This is especially true in the low Reynolds number flight regime that these rotors will be operating in. Whereas studies of rotors for higher Reynolds numbers performed with this tool and in other studies by Sidle et. al. [9] and Trollinger et. al. [39] have shown that propulsive efficiencies in excess of 60% can be obtained while retaining a figure of merit in excess of 70%, it is difficult to approach those levels of performance with conventional airfoils in this flow regime.

The results of this method are printed to input files for the aforementioned free-vortex method. In the current design framework, this module also returns an updated estimate for both figure of merit and propulsive efficiency to the initial sizing module, enabling further iteration to appropriately pair a rotor with a given aircraft.

4.3.2 PrasadUM Integration

As previously mentioned, the aircraft's proprotors, wings, and body are all necessarily in close proximity, with rotor wake impinging the aircraft in all normal operating modes, aerodynamic interactions must be taken into account in order to properly size the aircraft. To accomplish this, the aformentioned code has been developed with the intent of coupling it to an inviscid, incompressible, time-accurate Lagrangian free-vortex method in future work. This methodology has already been implemented in the Parallelized Rotorcraft Analysis for Simulation and Design tool (PrasadUM) developed at the University of Maryland and previously validated against flight test data for an aircraft both trimmed and maneuvering flight [40].

This tool computes blade loads and power requirements by integrating sectional loads determined by the Weissinger-L lifting line model, utilizing the local inflow angle, ϕ, and a lookup table for sectional airfoil properties. Hence, the integrated thrust and power coefficients are determined as follows:

$$C_T = \frac{1}{2\pi}\int_0^{2\pi}\int_e^1 \frac{\sigma}{2}\left(\frac{U}{\Omega R}\right)^2 (C_\ell cos(\phi) - C_d sin(\phi))\, dr\, d\Psi \tag{4.40}$$

$$C_P = \frac{1}{2\pi}\int_0^{2\pi}\int_e^1 \frac{\sigma}{2}\left(\frac{U}{\Omega R}\right)^2 (C_\ell cos(\phi) - C_d sin(\phi)) r\, dr\, d\Psi \tag{4.41}$$

The local inflow angle is modified not only by blade rotation, induced inflow velocity, and the freestream velocity, but also by the velocities induced by singularities in the tip vortex and on bodies external to the rotor system (e.g., wings, fuselage, etc.). The tip vortices are modeled as a series of Langrangian markers along a continuous

vortex filament emanating from a rotor tip, allowing the tip vortex to be modeled via a piecewise linear reconstruction. Assuming inviscid flow outside of the vortex core, these filament segments convect as material lines under the influence of local flow velocities and, thus, can be tracked via applying the linear advection equation to the Langrangian markers. As this is identical to the methodology outlined in the previous sections for computing wake convection, the addition of velocity contributions from the on-body singularities previously described poses no logical difficulty. Hence, the free-wake method can also be readily coupled with the internal Dirichlet solution previously explicated, providing estimates of on-body interference effects due to to the proprotors.

At present, by placing source terms on a discretized surface, the code also has the capability to compute the induced drag on bluff bodies as shown by Govindarajan [98]. The previously described panel method adds to this tool the capability to also consider lifting bodies.

Chapter 5: Sizing Results and Discussion

The following sections detail the use of the preliminary sizing tool developed in the course of this work. Traditional quadrotor and QBT configured aircraft are then sized for offshore wind turbine inspection missions and compared. Sizing studies are completed for two scenarios: an onshore wind inspection mission, and an offshore wind inspection mission. While the object of each mission, to inspect the blades of a representative 3 MW turbine, remained the same, the mission requirements vary drastically and thus reveal interesting conclusions regarding the configuration's applicability. For reference, the offshore wind inspection mission utilized in this section is given in Figure 5.1.

5.1 Preliminary Sizing

As noted previously, there is significant evidence to postulate the advantages of a QBT configured aircraft in an offshore wind inspection mission. To explore this, the preliminary design tool explicated in prior chapters was utilized to design both a QBT aircraft and a typical quadcopter UAS for the offshore wind turbine inspection mission outlined in Figure 1.10. For purposes of the mission, it was selected that the headwind in the sizing mission would be 95% of the maximum windspeed recorded

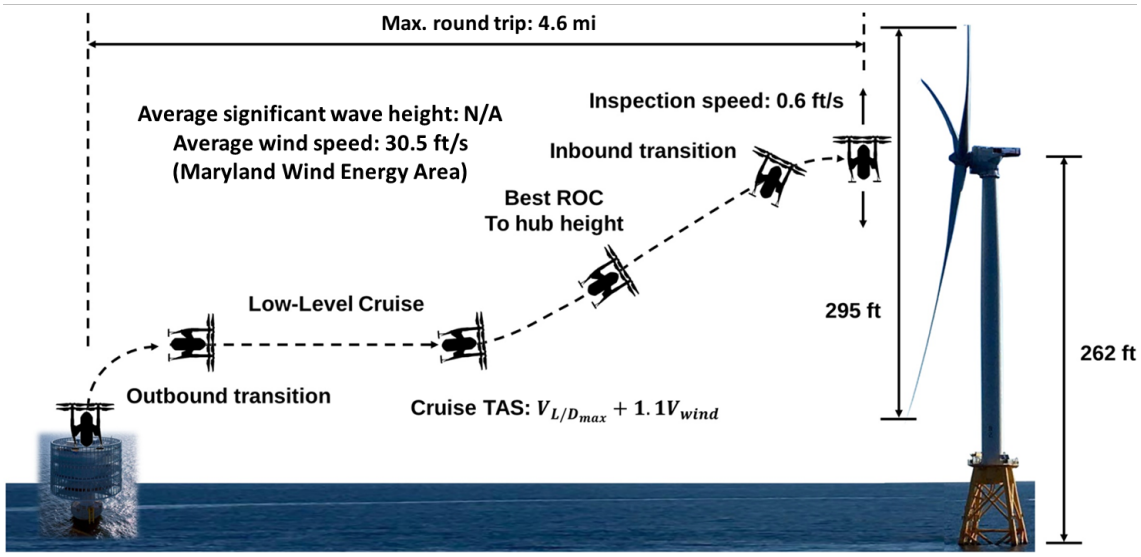

Figure 5.1: QBT inspection mission concept

in the collected weather data. This resulted in a cruise-level wind speed of 60.6 ft/s. Utilizing a power law transformation, this yields a hub height wind speed of 76.9 ft/s. Also, whereas the average deviation from ISA conditions for the Maryland offshore wind energy area is approximately $-1°$C, it is selected, for the sake of design robustness, that the ambient conditions for the mission correspond to a deviation of ISA+15.

Based on this, over 14,000 potential QBT designs were surveyed based on combinations of wing aspect ratio, wing loading, disc loading, and rotor solidity. The ranges of the survey are given in Table 5.3. Multicopter UAS designs were considered based on the same selections of disc loading and rotor solidity. The bounds of the parameter sweep were defined via a survey of existing rotorcraft on the desired scale as well as numeric experimentation.

Table 5.1: Offshore mission sizing: parameter sweep definition

Parameter	Lower bound	Upper bound	Increment
Wing aspect ratio	4	7	1
Wing loading	2 lbf/ft^2	18 lbf/ft^2	1 lbf/ft^2
Disc loading	1.0 lbf/ft^2	3.6 lbf/ft^2	0.2 lbf/ft^2
Rotor solidity	0.08	0.15	0.005

5.1.1 Downselect Methodology and Trade Study

Designs evolved by the sizing tool are ranked based on a design performance parameter (DP), defined here as the product of battery weight, $W_{batteries}$, and empty weight, W_{empty}, which is defined as the takeoff weight less batteries and payload: $DP = W_{empty} \cdot W_{batteries}$. As the primary difference between a quadcopter and a QBT-configured aircraft is the addition of a pair of wings, this metric will reflect the trade between energy storage capacity and wing weight. A minimization of this parameter would reflect the design that best manages this trade and, as powerplant and power transmission weights factor into the empty weight as well, requires a minimum of installed power.

Similarly, while GTOW is not explicitly a factor in this parameter, it is expected (and has been borne out in numerical experiments) that the selected design will have a low gross weight relative to the other designs of the same configuration. While minimizing GTOW is desirable from the standpoint of ground handling and material cost, the use of this design parameter allows for comparisons to be made across configurations that reflects the anticipated trade of structural weight and battery weight. With this in mind, the output of the parameter sweep can be seen

in Figure 5.2. All designs with a GTOW over 85 lbf have been omitted from the figure for clarity.

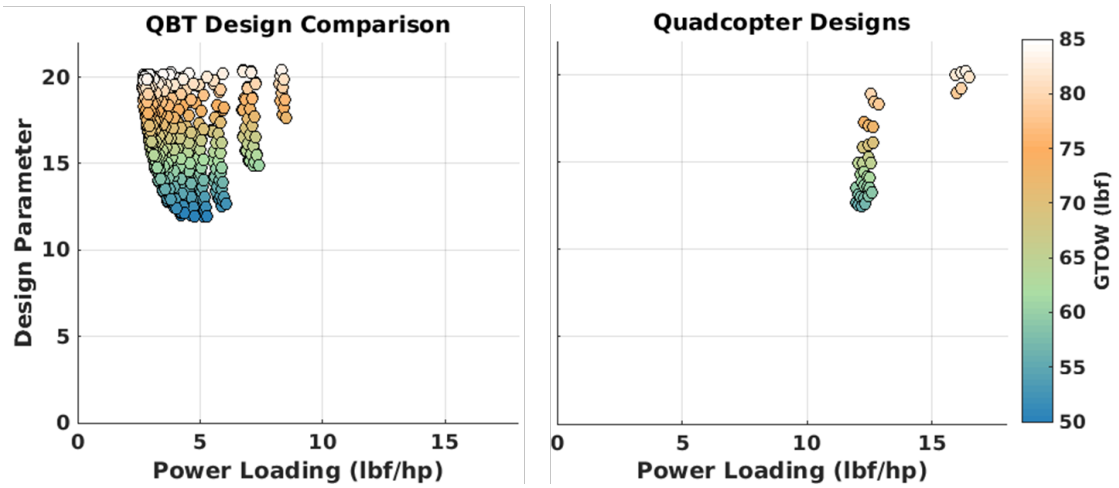

Figure 5.2: Offshore mission: design comparison

As shown by the design parameter, the trade between structural weight and energy storage is beneficial for this mission, allowing for a lighter, more energy-efficient aircraft to be sized for the task. However, this does come at the cost of hovering efficiency as, in hover, the wings yield no performance benefit: only additional weight, leading to the decrease in power loading between the quadcopter and QBT configurations. Hence, while the hover endurance requirement for this mission is significant, it does not appear to be more demanding than the cruising flight requirements in this case.

To better understand the trades made in this design study, a sensitivity analysis was performed using the independent parameters selected in the design space survey: wing aspect ratio, wing loading, disc loading, and rotor solidity. The results of these studies are shown below in Figure 5.3. Note that the designs represented above represent designs that have successfully passed the blade load and aspect ratio

thresholds discussed in Section 3.2.

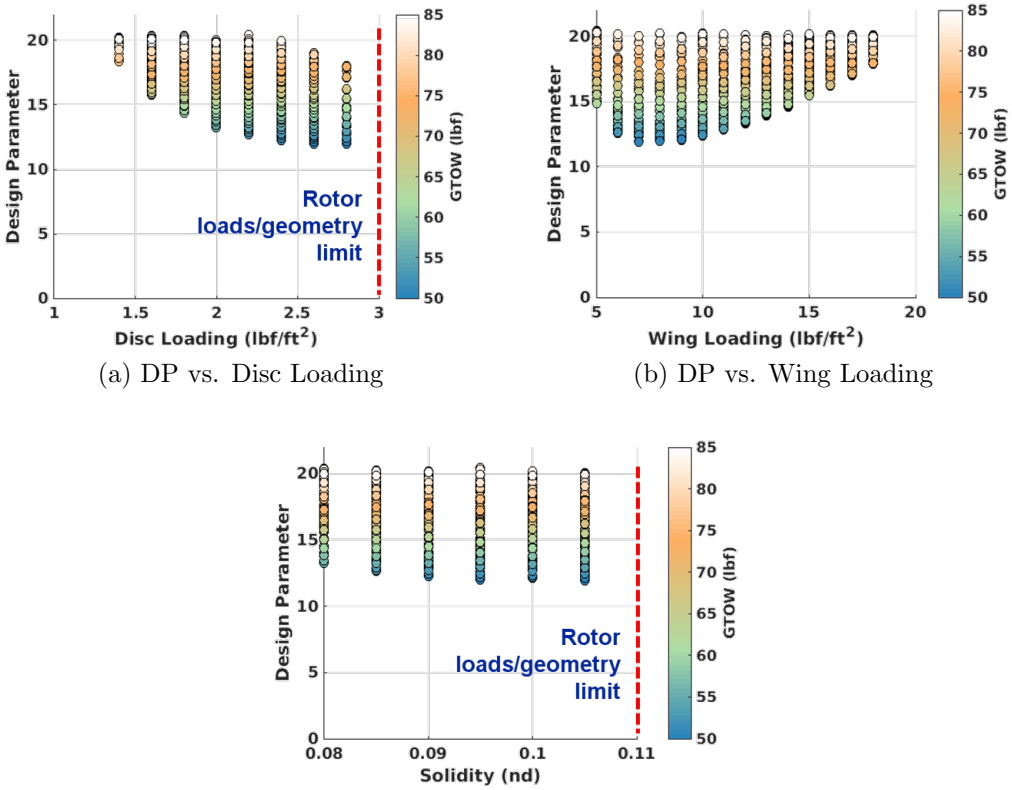

(a) DP vs. Disc Loading

(b) DP vs. Wing Loading

(c) DP vs. σ

Figure 5.3: Variation in the design parameter for the QBT configuration with respect to the survey variables

While there is little variation in the design parameter with respect to wing aspect ratio, disc loading, wing loading, and rotor solidity are quite significant. Each parameter represents a trade in weight and power efficiency. In terms of wing loading, this trade is between a induced drag and structural weight, where a lower wing loading corresponds to a larger, heavier wing, but a decreased induced drag. Similarly, an increase in solidity corresponds blades that are, perhaps, capable of carrying flight loads, but also an increase in the rotor's profile power. Increases in disc loading also contribute positively to this trade, albeit secondarily, and is

limited by blade loading limits, as disc loading is related to blade loading. Increases in rotor size also lead to a marginally increased gross weight due to the extra material required to maintain rotor/rotor separation as well as extra blade material.

Something that bears emphasis in the interpretation of the sizing results is the demanding nature of the mission. As shown in Table **??**, the weight fractions of the aircraft sized for this mission are dramatically unlike a typical rotorcraft, specifically with regard to the proportion of the aircraft's mass that is utilized for energy storage. For example, the current world record holder for model electric helicopter flight duration [109] is alleged to have used a Logo 600 SE V2 helicopter, which typically operates at a battery fraction of 0.28 [110]. For the world record flight, the typical power source (a 4,500 mAh LiPo battery) was replaced by a 32,000 mAh LiPo battery, increasing the battery fraction to over 0.6. This, and other modifications, resulted in a flight lasting 2 hours, 58 minutes, and 17 seconds. By this hermaneutic, it is not out of the ordinary that an endurance-centric mission with aggressive cruise requirements would result in a similar weight distribution wherein the energy storage media dominates the weight buildup. As a consequence, this also results in an atypically low payload fraction, in this case 0.02, for either design evolved by the preliminary design code.

5.1.2 Design Selection

Moving on to an analysis of the entire design space, a brief overview of the two designs selected via minimizing the design parameter over this space (as shown

in Figure 5.2) is given in Table 5.2. An immediate realization from this result is the difference in structural weight and battery weight between the two configurations. To convert from the "optimal" quadcopter design to the "optimal" QBT design for this mission, the aircraft gained 2 lbf of weight in wing structure, but lost 10 lbf of battery weight (not including fuselage weight savings due to this decreased battery weight). In essence, structural weight was traded for cruise efficiency. For a long range mission such as this, this trade can be performed favorably, ultimately leading to a decreased takeoff weight. However, as can be inferred by the disparity in power loading shown in Figure 5.2, this trade will have negative outcomes for hover-dominated missions and the quadcopter will be the favored design, as is expected. This will be shown in more detail in the following section for a shorter-range mission.

Furthermore the dominance of the QBT design is demonstrated in the mission time. Not only does the aircraft provide a favorable flight efficiency trade, but it also inherently enables higher-speed forward flight modes. This enables the "optimal" QBT design to complete the inspection mission in nearly half the time required by the quadcopter design.

5.1.3 Extension to Onshore Inspection Mission

To further explore the QBT design space, the following scenario is considered: an onshore wind turbine inspection. Using present inspection methodologies, the various methods of inspection do not vary from the offshore wind case save in the difficulty of transport to the turbine itself, which is greatly reduced. Hence, the value

Table 5.2: Offshore mission: "optimal" design outputs

Parameter	Quadcopter	QBT
Takeoff Weight	55.79 lbf	49.73 lbf
Empty Weight	20.10 lbf	24.07 lbf
Battery weight	34.68 lbf	24.66 lbf
Payload weight	1.00 lbf	1.00 lbf
—	—	—
Fuselage weight	9.18 lbf	5.84 lbf
Strut weight/each	0.25 lbf	0.31 lbf
Landing gear weight/each	0.16 lbf	0.32 lbf
Wing weight/each	N/A	1.05 lbf
ESC weight/each	0.14 lbf	0.19 lbf
Motor weight/each	0.74 lbf	1.50 lbf
Rotor weight/each	0.46 lbf	0.42 lbf
Power transmission weight	2.20 lbf	3.34 lbf
Systems weight	1.80 lbf	1.80 lbf
—	—	—
Aspect ratio	N/A	7
Wing loading	N/A	7 lbf/ft^2
Disc loading	2.4 lbf/ft^2	2.8 lbf/ft^2
Solidity	0.090	0.105 nd
Rotor diameter	2.72 ft	2.38 ft
Cruise speed	65.9 ft/s	92.5 ft/s
L/D ratio (cruise)	0.04	12.3
Mission time	65.2 min	35.7 min

added by a QBT configured aircraft lies in its ability to fly ahead of an inspection team and begin inspections without requiring personnel to be immediately on-site, thus decreasing the time spent waiting for an inspection to be completed. Hence, the following mission concept, shown in Figure 5.4 is proposed. Wind speeds for this mission are derived from NREL estimates for of average wind speeds in Maryland at a height of 80 m [111]. Inter-array distance derived from typical row-to-row spacing noted in wind projects to avoid wake interference effects.

In this concept, the inspection team readies the aircraft and launches it for an

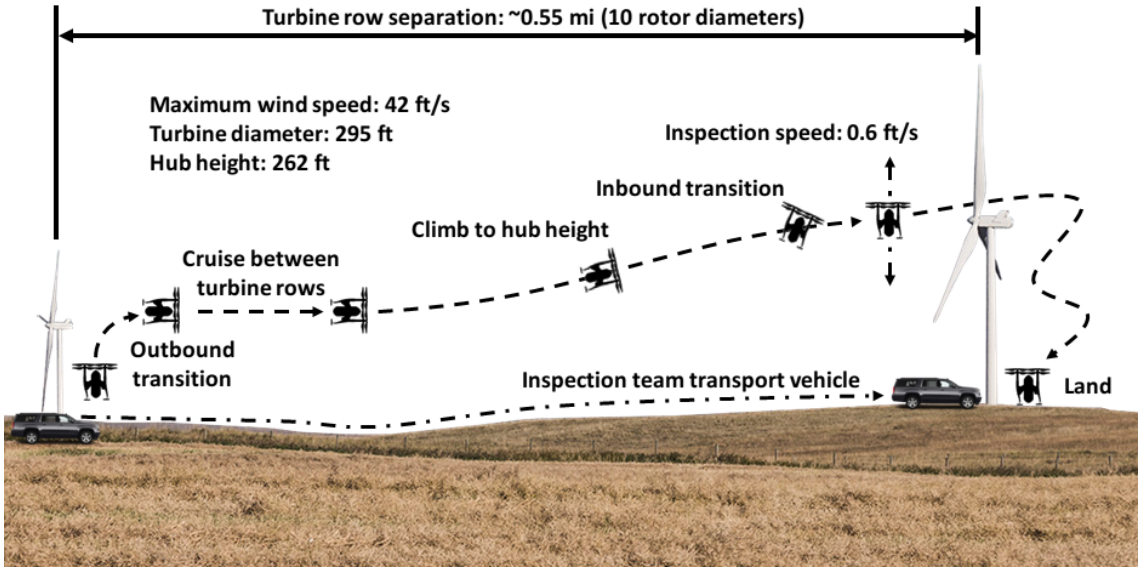

Figure 5.4: QBT inspection mission concept (onshore)

inspection mission in the next row of turbines. This mission is completed while the inspection team is en route to the turbine of interest. Once complete, the aircraft lands, is recovered by the inspection team, and prepared for its next use. Note, however, that while the expected range and wind speeds are significantly lower than those expected in the offshore case, the hover requirement remains the same. To reflect this, the parameter sweep shown in Table **??** has been determined to be sufficient, encompassing over 17,000 configurations.

Table 5.3: Onshore mission sizing: parameter sweep definition

Parameter	Lower bound	Upper bound	Increment
Wing aspect ratio	4	7	1
Wing loading	2 lbf/ft^2	14 lbf/ft^2	1 lbf/ft^2
Disc loading	0.2 lbf/ft^2	2.0 lbf/ft^2	0.2 lbf/ft^2
Rotor solidity	0.02	0.2	0.005

As might be expected with the relaxed cruise requirements, the trade between

structure and energy storage is not as beneficial in this case. This can be clearly seen in Figure 5.5, where the quadcopter designs easily outmatch the QBT designs by this metric. As previously noted, this was to be expected as cruise requirements were relaxed. All designs with a GTOW over 20 lbf have been omitted from the figure for clarity.

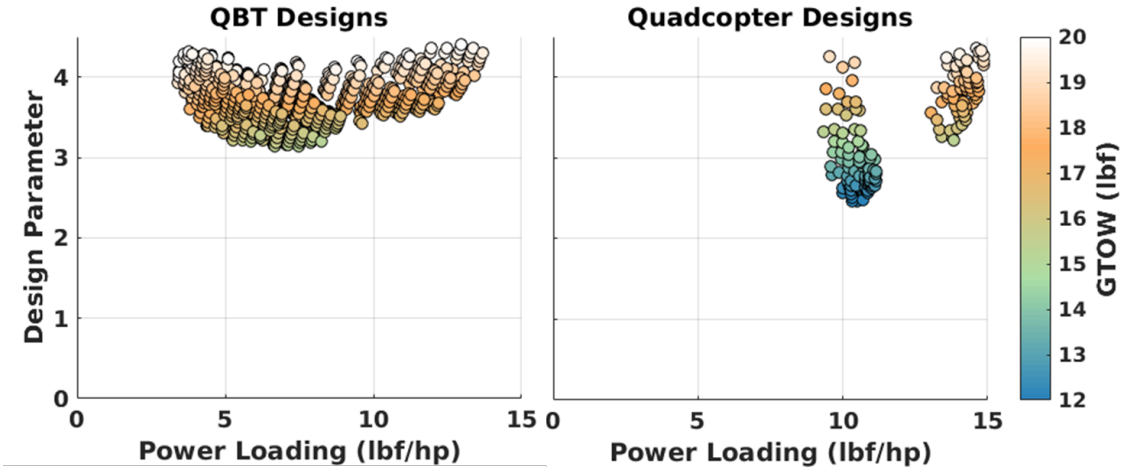

Figure 5.5: Onshore mission: design comparison

Hence, as shown in Table 5.4, while the QBT design has decreased in magnitude to meet the decreased cruise requirements, it suffers a significant penalty in this mission by the requirement of wings. While the use of wings to enable a high-speed forward flight mode does ultimately decrease battery weight, the battery weight traded for structural weight is relatively small, resulting in 28% increase in takeoff weight. This weight gain also biases the design towards marginally higher solidities and disc loadings to accommodate the added weight, resulting in less efficient rotor systems.

Table 5.4: Onshore mission: "optimal" design outputs

Parameter	Quadcopter	QBT
Takeoff Weight	11.78 lbf	15.03 lbf
Empty weight fraction	0.46	0.56
Battery fraction	0.45	0.37
Wing weight fraction	N/A	0.05
Payload fraction	0.08	0.07
Disc loading	1.2 lbf/ft^2	1.6 lbf/ft^2
Rotor solidity	0.045	0.060
Wing loading	N/A	3 lbf/ft^2
Wing aspect ratio	N/A	7

Chapter 6: Summary and Recommendations

This work began with the objective of developing a toolset for use in the design of QBT configured aircraft, as well as to provide a motivation for the use of QBT configured aircraft in the offshore wind industry. To this end, the following progress has been made.

6.1 Conclusions

Corresponding the objectives of this thesis, the work detailed in previous chapters has led the author to conclude the following.

6.1.1 QBT Aircraft for Wind Turbine Inspections

Thanks to its ability to remain insulated from ocean conditions, the QBT configuration shows great promise for future application in the offshore wind industry. For a hypothetical wind farm in the Maryland offshore wind energy area, a QBT-configured aircraft is able to access a turbine for over 97% of the year, an increase of over 100% from any traditional inspection methodology. Even without the ability or legal clearance to fly under nighttime conditions, the aircraft demonstrably increases an operator's accessibility to a given turbine for routine maintenance inspections by

23% over methods utilizing traditional UAS supported by CTVs.

Analysis of a full-farm inspection mission yielded similar results, underscoring the ability of a QBT-configured aircraft to perform inspections with twice the consistency of a CTV supported UAS, as measured by the standard deviation in inspection mission times. Similarly, during periods of more extreme weather, the QBT delivers faster mission times, on average, relative to CTV-supported UAS. This can be further increased by nearly 30% by enabling the QBT to fly and inspect turbines even during the night. These capabilities are facilitated by the QBT's capability to operate independently from manned vessels and a high wind tolerance.

However, this aircraft is not a panacea. Its advantages over a traditional multicopter are limited to missions with aggressive cruise requirements, such as the offshore wind inspection mission detailed here, where the trade of energy storage weight for wing weight is a positive one (i.e., leading to an overall decrease in aircraft weight and, potentially, cost). For missions with a greater focus on hovering flight endurance, the traditional multicopter eclipses the QBT configuration in performance and simplicity. Insofar as design is concerned, this may be motivation to incorporate modularity into the QBT configuration such that the wings can be removed as needed, further increasing the mission flexibility of the aircraft. However, this does give significant motivation for the continued development of this aircraft for applications in offshore wind energy maintenance missions.

6.1.2 Preliminary Sizing Tool

In sizing studies for on- and offshore wind turbine inspection missions, this tool demonstrates the primary trade between traditional quadcopters and QBT aircraft: the exchange of weight in the form of energy storage media for wing weight. These studies have identified that aggressive, long range missions, such as the offshore wind turbine inspection mission considered here, make this a positive trade wherein the aircraft can decrease its energy storage weight for a relatively small gain in structural weight. In the case investigated here, the QBT allowed for a 10 lbf decrease in battery weight, a decrease of 29% relative to a traditional quadcopter sized for the same mission. This was enabled by the addition of a relatively small 2.1 lbf of wing weight.

However, for shorter-range missions with less aggressive cruise requirements, such as the onshore wind turbine inspection mission also considered, the QBT incurs a significant weight penalty as opposed to conventional quadcopters, a net increase in structural weight, battery weight, and gross takeoff weight for a given mission.

6.1.3 Vehicle Sizing Tools

As indicated by investigations of various rotor geometries for both fixed- and variable-pitch rotors for a QBT flying an offshore wind mission, it was found that the addition of a variable collective pitch grants a propulsive efficiency benefit of nearly 100% when compared to fixed-pitch rotors. While even fixed-pitch rotors operating at high-Reynolds numbers (in excess of 1 million) can provide propulsive

efficiencies and a figure of merit in excess of 50%, the relatively low Reynolds number regime seen here (under 580,000) leads to significant aerodynamic inefficiencies for traditional airfoils. Hence, the maximum propulsive efficiency for the over 2,000 rotor configurations considered, even for a rotor with variable collective pitch, is only 43%, with a figure of merit of 66%.

6.2 Key Contributions

In addition to the various conclusions previously outlined, this work also contributes the following tools to the continued developed of the QBT configuration.

1. **Offshore Wind Turbine Inspection Mission Analysis Tool:** this model includes a statistical weather model and basic aerodynamic modeling, enabling the comparison of different inspection vehicles in an offshore wind inspection mission. Historical weather data was compiled for the Maryland offshore wind energy area for use, encompassing the last 15 years of NOAA weather buoy operations in that area.

2. **Weight Model Development:** the weight model developed here is purpose-built for small scale QBTs used in the offshore wind mission, although an upper limit for its use has yet to be determined. As noted in Chapter 3, the gross weight estimate evolved by this tool resulted in a 10% difference from measured value for the prototype aircraft. Breaking this difference into its various components, the empirical weight models developed showed fair agreement with the prototype aircraft: the powerplant weight estimates matching to 1.6%, al-

though the battery weight estimations differed by 9%. The structural weight model differed significantly from the prototype aircraft, although, based on the assumptions made in its creation to suit an aircraft in a maritime environment, this model is not expected to match the prototype aircraft. Development will, naturally, be required in order to further generalize the model and increase the size and detail of the database from which it is derived. This will need to take place in parallel with the development of the design itself to account for QBT-specific design opportunities and challenges. In the meantime, the model suffices to provide initial weight estimations for new vehicles.

3. **Preliminary Design Tool:** a preliminary sizing framework has been established, enabling the rapid sizing of QBT configured aircraft for a wind turbine inspection mission. The tools developed as part of this framework include: preliminary aerodynamic models, a weight model, a rotor design module, and various geometry generation codes for future, more detailed analysis. Some flexibility has been incorporated to enable user selection of more general mission segments as well in order to support development of the configuration for other purposes. This design framework, while its output has not yet been realized in a physical vehicle, has laid the groundwork for future development of the configuration.

4. **3D, Unsteady Panel Method**: to enable more accurate sizing predictions in future design studies, an unsteady, 3D panel method has been developed, using a nonlinear implementation of the Kutta condition. This methodology,

when coupled to a free-vortex solver (such as PrasadUM [40]), has the potential to enable designers to more accurately, intelligently, and quickly estimate the aerodynamic interference effects central to the design of QBT aircraft.

5. **Geometry Generation Tools:** in this work, geometry generation tools for rotors, wings, and bodies were developed, enabling the use of the panel method developed in this part in conjunction with rotor analysis tools, such as PrasadUM, for full-vehicle performance investigation. These tools include a rotor geometry generator, capable of estimating rotor geometries best suited for specific mission profiles, as well as wing and fuselage geometry generators.

6.3 Recommendations for Future Work

As the work completed here is brought to fulfillment and integrated into future design studies, the following recommendations are given.

1. **Refine concept of operations and explore different missions for this vehicle:** as noted, this aircraft has significant application in offshore wind energy, but the missions considered for the design in this work have been relatively few in number. A greater understanding of the configuration's capabilities on the present scale will be useful not only for commercialization but also as a guide for the further development of the configuration.

2. **Create physical designs to refine the design tools produced in this work:** this especially applies to the preliminary sizing tool, where early ap-

proximations should be replaced by empirical or semi-empirical expressions derived from design and analysis studies, the latter being enabled by the panel method also developed here. Alternative manufacturing methodologies and appropriate structural modeling techniques, as opposed to the methods and materials chosen here, should also be explored.

3. **Integrate the unsteady panel code into a free-vortex code, such as PrasadUM:** as noted, the panel method developed here, while a valid tool, is not useful for the analysis of this configuration in and of itself. Its use in this design requires that it be coupled to a rotor aerodynamic solver, such as PrasadUM. This should be considered as the next step in the continued development of these design tools so as to better understand the physical phenomena influencing the configuration and refine designs evolved from the tools stemming from this work and others.

4. **Develop an accelerated panel method to enable rapid design analysis:** the panel method created here is rapidly slowed by large cases, particularly those of over 25,000 panels. While still faster than higher-order computational methods for a 3D model in steady flow, unsteady wake convection from multiple bodies could rapidly generate an excess of panels that will delay a design investigation potentially for days. Thus, the implementation of parallel processing or an accelerated numerical method (such as so-called fast multipole methods) that could be incorporated into the method are recommended for future investigation.

5. **Quantify the need for gust-rejection capabilities:** an oft-repeated question concerning the suitability for the QBT configuration for offshore wind inspection missions is this: will the QBT configuration be overly susceptible to wind gusts? While not a topic for the present work, this question does need to be answered, especially with an eye towards applying the aircraft to offshore wind inspection mission presented here. This may also lead to a reformulation of the design parameter introduced in this work.

Appendix A: Weight Model Detail

In this section, specific details concerning weight model components are given, including the formulation of the empirical weight models developed and the candidate material selected for the design studies described in this work.

A.1 Empirical Weight Model Formulation

The empirical weight models discussed in Section 3.3.1 were developed from a database of commercially available components, including: 244 brushless DC motors, 175 electronic speed controllers (for brushless DC motors), and 161 lithium polymer batteries. The empirical relations derived between various design parameters and component specifications are given in the following expressions. The correlation coefficients corresponding to each curve fit are listed with their respective equation.

$$W_{motor} = 0.00084659(P_{reqd}^{0.98831}) \qquad (R^2 = 0.989) \tag{A.1}$$

$$I_{max_{motor}} = 0.069163[log(W_{motor})]^{0.98831}) \qquad (R^2 = 0.899) \tag{A.2}$$

$$W_{ESC} = 0.0030939(I_{max_{ESC}}^{0.91428}) \qquad (R^2 = 0.899) \tag{A.3}$$

$$W_{battery} = 0.000014842(E_{reqd}^{0.91566}) \qquad (R^2 = 0.991) \tag{A.4}$$

$$I_{max_{battery}} = 0.000043159(mAh^{1.7971}) \qquad (R^2 = 0.864) \tag{A.5}$$

In these expressions, the following nomenclature is used:

- W_{motor}: motor weight (pounds)
- P_{reqd}: power requirement determined by the sizing mission (foot pounds per second)
- $I_{max_{motor}}$: motor maximum current specification (amperes)
- W_{ESC}: weight of the ESC (pounds)
- $I_{max_{ESC}}$: ESC current rating (equivalent to the motor current specification)
- $W_{battery}$: battery weight (pounds)
- E_{reqd}: energy storage requirement determined by the sizing mission (foot pounds)
- mAh: capacity of an individual battery pack (milliamp hours)
- $I_{max_{battery}}$: maximum current rating for an individual battery pack (amperes)

A.2 Material Properties

The material selected for this study, an isotropic 20% carbon filled polycarbonate formulated and manufactured by Prime Manufacturing Technologies Inc., is specified by the mechanical properties listed in Table A.1.

Table A.1: Material specification

Parameter	Value
Density	0.0325 lbf/in^3
Modulus of elasticity	800 ksi
Shear modulus	666.7 ksi
Tensile strength	20 ksi

Bibliography

[1] Smith, A., Stehly, T., and Musial, W., "2014-2015 Offshore Wind Technologies Market Report," NREL/TP 5000-64283, September 2015.

[2] Carroll, J., McDonald, A., and McMillan, D., "Failure rate, repair time and unscheduled O&M cost analysis of offshore wind turbines," *Wind Energy*, 2015.
doi: 10.1002/we.1887

[3] "National Oceanic and Atmospheric Administration's National Buoy Data Center: Station 44009," http://www.ndbc.noaa.gov/station_page.php?station=44009.

[4] Reuder, J., Brisset, P., Jonassen, M., Müller, M., and Mayer, S., "The Small Unmanned Meteorological Observer SUMO: A new tool for atmospheric boundary layer research," *Meteorologische Zeitschrift*, Vol. 18, (2), April 2009, pp. 141–147.

[5] Phillips, B., Hrishikeshavan, V., Yeo, D., Chopra, I., and Rand, O., "Flight Performance of a Package Delivery Quadrotor Biplane," 7th AHS Technical Meeting on VTOL Unmanned Aircraft Systems, Phoenix, AZ, January 2017.

[6] Ramasamy, M., "Measurements Comparing Hover Performance of Single, Coaxial, Tandem, and Tilt-Rotor Configurations," 69th Annual Forum of the American Helicopter Society, Phoenix, AZ, May 2013.

[7] Luo, J., Zhu, L., and Yan, G., "Novel Quadrotor Forward-Flight Model Based on Wake Interference," *AIAA Journal*, Vol. 52, (12), December 2015, pp. 3522–3533.

[8] Veldhuis, L. L. M., *Propeller Wing Aerodynamic Interference*, Ph.D. thesis, Delft University of Technology, 2005.

[9] Sidle, S., Bogdanowicz, C., Gudenius, B., Shishika, D., Wang, X., and Winslow, J., "AirEZ," http://www.ahs.umd.edu/assets/downloads/2015_airez.pdf.

[10] Prandtl, L., "Induced Drag of Multiplanes," NACA TR 182, February 1924.

[11] Hess, J., "Calculation of Potential Flow About Arbitrary Three-Dimensional Lifting Bodies," Technical Report MDC J5679-01, October 1972.

[12] Erickson, L., "Panel Methods: An Introduction," NASA Technical Paper 2995, 1990.

[13] Maskew, B., "Prediction of Subsonic Aerodynamic Characteristics: A Case for Low-Order Panel Methods," *Journal of Aircraft*, Vol. 19, (2), 1982, pp. 157–163.

[14] Administration, U. S. E. I., "Levelized Cost and Levelized Avoided Cost of New Generation Resources in the Annual Energy Outlook 2017," https://www.eia.gov/outlooks/aeo/pdf/electricity˙generation.pdf.

[15] Musial, W. and Ram, B., "Large-Scale Offshore Wind Power in the United States: Assessment of Opportunities and Barriers," NREL/TP 500-40745, September 2010.

[16] Shafiee, M., Finkelstein, M., and Bérenguer, C., "An opportunistic condition-based maintenance policy for offshore wind turbine blades subjected to degradation and environmental shocks," *Reliability Engineering & System Safety*, Vol. 142, Oct 2015, pp. 463–471.

[17] Dinwoodie, I. and McMillan, D., "Sensitivity of Offshore Wind Turbine Operation & Maintenance Costs to Operational Parameters," 42nd ESReDA Seminar on Risk and Reliability for Wind Energy and other Renewable Sources, Glasgow, UK, May 2012.

[18] Lei, X., Sandborn, P., Bakhshi, R., Kashani-Pour, A., and Goudarzi, N., "PHM based predictive maintenance optimization for offshore wind farms," IEEE Conference on Prognostics and Health Management, Austin, TX, 2015.

[19] Sarker, B. and Fiaz, T., "Minimizing maintenance cost for offshore wind turbines following multi-level opportunistic preventive strategy," *Renewable Energy*, Vol. 85, 2016, pp. 104–113.

[20] Kandukuri, S., Klausen, A., Karimi, H., and Robbersmyr, K., "A review of diagnostics and prognostics of low-speed machinery towards wind turbine farm-level health management," *Renewable and Sustainable Energy Reviews*, Vol. 53, Jan 2016, pp. 697–708.

[21] Takoutsing, P., Wamkeue, R., Ouhrouche, M., Slaoui-Hasnaoui, F., Tameghe, T., and Ekemb, G., "Wind Turbine Condition Monitoring: State-of-the-Art Review, New Trends, and Future Challenges," *Energies*, Vol. 7, (4), April 2014, pp. 2595–2630.

[22] "Robin Rigg Offshore Wind Farm (Navigation and Fishing) (Scotland) Bill," , 2003.

[23] Maples, B., Saur, G., Hand, M., van de Pietermen, R., and Obdam, T., "Installation, Operation, and Maintenance Strategies to Reduce the Cost of Offshore Wind Energy," NREL/TP 5000-57403, July 2013.

[24] "Drones for Wing Turbine Inspection ," https://www.navigantresearch.com/research/drones-for-wind-turbine-inspection.

[25] "Installation and Maintenance of Wind Generator Blades," http://skyproff.com/wind-turbine-operation-and-maintenance-services/, March 2017.

[26] "Brisk Business for UAV Wind Turbine Inspection," http://www.dji.com/newsroom/news/blog-brisk-business-for-uav-wind-turbine-inspection.

[27] "Bluesky & Cyberhawk Partnership for Aerial Mapping & Survey," http://www.asctec.de/en/bluesky-cyberhawk-partnership-for-aerial-mapping-survey/, March 2017.

[28] "Aeolus Energy Servicing: Drones ," http://www.aeolusenergyservicing.com/drones.html, March 2017.

[29] "Aibotix X6," https://www.aibotix.com/products/aibot-x6, March 2017.

[30] "AscTec Professional Line Catalogue ," http://www.asctec.de/downloads/public/AscTec-Professional-Line˙Catalogue.pdf, March 2017.

[31] "Inspire 1 - Specs," http://www.dji.com/inspire-1/info, March 2017.

[32] "Spreading Wings S1000," http://www.dji.com/spreading-wings-s1000/spec, March 2017.

[33] "DEME Looking Into Drones," http://www.offshorewind.biz/2017/06/15/deme-looking-into-drones/.

[34] Reuder, J. and Jonassen, M., "First results of turbulence measurements in a wind park with the Small Unmanned Meteorological Observer SUMO," *Energy Procedia*, Vol. 24, 2012, pp. 176–185.

[35] Båserud, L., Flügge, M., Bhandari, A., and Reuder, J., "Characterization of the SUMO turbulence measurement system for wind turbine wake assessment," *Energy Procedia*, Vol. 53, 2014, pp. 173–183.

[36] Reuder, J., Båserud, L., Krala, S., Kumera, V., Wagenaarc, J. W., and Knauerd, A., "Proof of concept for wind turbine wake investigations with the RPAS SUMO," 13th Deep Sea Offshore Wind R&D Conference, EERA DeepWind 2016, Trondheim, Norway, January 2016.

[37] Hrishikeshavan, V., Bogdanowicz, C., and Inderjit, C., "Experimental Investigation of Performance of a Wing-Propeller System for a Quad-Rotor-Biplane Micro Air Vehicle," 54th Structures, Structural Dynamics, and Materials Conference, Boston, MA, April 2013.

[38] Hrishikeshavan, V., Bogdanowicz, C., and Inderjit, C., "Design, Performance and Testing of a Quad Rotor Biplane Micro Air Vehicle for Multi Role Missions," *International Journal of Micro Air Vehicles*, Vol. 6, (3), September 2014, pp. 155–173.

[39] Trollinger, L., Kreutzfeldt, T., Strom, M., Jung, Y. S., Smith, L., Gonzalez, O., Perez-Sanchez, E., and Quinones, R., "Halcyon," http://www.ahs.umd.edu/assets/downloads/2016˙halcyon.pdf.

[40] Rubenstein, G., Moy, D. M., Sridharan, A., and Chopra, I., "A Python-based Framework for Real-time Simulation using Comprehensive Analysis," 72nd Annual Forum of the American Helicopter Society, West Palm Beach, FL, May 2016.

[41] Witkowski, D. P., Johnston, R. T., and Sullivan, J. P., "Propeller/Wing Interaction," Paper AIAA-89-0535, 27th AIAA Aerospace Sciences Meeting, Reno, NV, January 1989.

[42] Ananda, G. K., Deters, R. W., and Selig, M. S., "Propeller-Induced Flow Effects on Wings of Varying Aspect Ratio at Low Reynolds Numbers," 32nd AIAA Applied Aerodynamics Conference, Atlanta, GA, June 2014.

[43] Maqsood, A., Chang, C. W. T., and Go, T. H., "Experimental Investigation of a Biplane Micro Air Vehicle," 28th International Congress of the Aeronautical Sciences, 2012.

[44] Moschetta, J.-M. and Thipyopas, C., "Aerodynamic Performance of a Biplane Micro Air Vehicle," *Journal of Aircraft*, Vol. 44, (1), January 2007, pp. 291–299.

[45] Munk, M. M., "General Biplane Theory," NACA TR 151, January 1923.

[46] Stepniewski, W. Z. and Shinn, R. A., "A Comparative Study of Soviet vs. Western Helicopters: Part 2 - Evaluation of Weight, Maintainability, and Design Aspects of Major Component," Technical Report 82-A-10, 1983.

[47] Winslow, J., *Understanding of Low Reynolds Number Aerodynamics and Design of Micro Rotary-Wing Air Vehicles*, Master's thesis, University of Maryland, College Park, Maryland, 2016.

[48] Chambers, M. C., Ardema, M. D., Patron, A. P., Hahn, A. S., Miura, H., and Moore, M. D., "Analytical Fuselage and Wing Weight Estimation of Transport Aircraft," NASA TM 110392, 1996.

[49] Yeo, D., Hrishikeshavan, V., and Inderjit, C., "Gust Detection and Mitigation for a Quad Rotor Biplane," Paper AIAA 2016-1531, AIAA Atmospheric Flight Mechanics Conference, San Diego, CA, January 2016.

[50] Hrishikeshavan, V. and Inderjit, C., "Refined Lightweight Inertial Navigation System for Micro Air Vehicle Applications," Specialists Meeting on Unmanned Rotorcraft and Network Centric Operations of the American Helicopter Society, Pheonix, AZ, January 2015.

[51] "Jumpship," https://transition-robotics.com/pages/jumpship, March 2017.

[52] "Parrot Swing," https://www.parrot.com/us/minidrones/parrot-Swing#parrot-swing, March 2017.

[53] Hogge, J. V., *Development of a Miniature VTOL Tail-Sitter Unmanned Aerial Vehicle*, Master's thesis, Brigham Young University, Provo, Utah, 2008.

[54] Stone, R. H., Anderson, P., Hutchison, C., Tsai, A., Gibbens, P., and Wong, K. C., "Flight Testing of the T-Wing Tail-Sitter Unmanned Air Vehicle," *Journal of Aircraft*, Vol. 45, (2), 2008, pp. 673–685.

[55] Kubo, D. and Suzuki, S., "Tail-Sitter Vertical Takeoff and Landing Unmanned Aerial Vehicle: Transitional Flight Analysis," *Journal of Aircraft*, Vol. 45, (1), 2008, pp. 292–297.

[56] Bapst, R., Ritz, R., Meier, L., and Pollefeys, M., "Design and Implementation of an Unmanned Tail-sitter," 2015 IEEE/RSJ International Conference on Intelligent Robots and Systems, Hamburg, Germany, Sep 2015.

[57] Hochstenbach, M., Notteboom, C., Theys, B., and Schutter, J. D., "Design and Control of an Unmanned Aerial Vehicle for Autonomous Parcel Delivery with Transition from Vertical Take-off to Forward Flight - VertiKUL, a Quadcopter Tailsitter," *International Journal of Micro Air Vehicles*, Vol. 7, (4), 2015.

[58] Oosedo, A., Konno, A., Matsumoto, T., Go, K., Masuko, K., and Uchiyama, M., "Design and Attitude Control of a Quad-Rotor Tail-Sitter Vertical Takeoff and Landing Unmanned Aerial Vehicle," *Advanced Robotics*, Vol. 26, 2012, pp. 307–326.

[59] Bramlette, R. B., Johnston, T. A., and Barrett, R. M., "Design, Construction, and Flight Testing of the Worlds Fastest Micro-Scale Quadcopter," 55th AIAA Aerospace Sciences Meeting, Grapevine, TX, January 2017.

[60] "ATMOS UAV," http://www.atmosuav.com/content.

[61] "Joby Energy Virtual Lab," http://www.jobyenergy.com/tech/visit.

[62] "Aerial Robotics: Remote Piloted Aircraft Systems (RPAS) Design and Autonomous Control," https://www.mech.kuleuven.be/en/pma/research /robotics/research/applications/aerialrobots.

[63] Drury, J., "Belgian drone mixes plane and quadcopter technology," http://www.reuters.com/article/us-belgium-drones-idUSKCN0UW18G.

[64] "Sun or Moon Rise/Set Tables for One Year," http://aa.usno.navy.mil/data/docs/RS_OneYear.php.

[65] "V90-3.0 MW® at a Glance ," https://www.vestas.com/en/products/turbines/v90%203˙0˙mw.

[66] "Fleet - Windea Offshore," http://windea.de/fleet/.

[67] Dinwoodie, I., Endrerud, O.-E., Hofmann, M., Martin, R., and Sperstad, I., "Reference Cases for Verification of Operation and Maintenance Simulation Models for Offshore Wind Farms," *Wind Engineering*, Vol. 39, (1), 2015, pp. 1–14.

[68] "CM160 Gimbals ," http://www.uavvision.com/products/gimbals/cm160.

[69] Feng, J. and Shen, W., "Modeling Wind for Wind Farm Layout Optimization Using Joint Distribution of Wind Speed and Wind Direction," *Energies*, Vol. 8, (4), Apr 2015, pp. 3075–3092.

[70] Leishman, J. G., *Principles of Helicopter Aerodynamics*, Cambridge University Press, New York, NY, 2006.

[71] Anderson, J., *Fundamentals of Aerodynamics*, McGraw-Hill Education, New York, NY, 2011.

[72] Raymer, D. P., *Aircraft Design: A Conceptual Approach*, American Institute of Aeronautics and Astronautics, 2011.

[73] Hoerner, D. F., *Fluid-Dynamic Drag*, New York, NY, 1965.

[74] FAA, "Acceptable Methods, Techniques, and Practices - Aircraft Inspection and Repair," Technical Report AC 43.13-1B, 1998.

[75] Scanlan, R. G. and Rosenbaum, R. A., *Introduction to the Study of Aircraft Vibration and Flutter*, MacMillan, New York, NY, 1951.

[76] Hodges, D. H. and Pierce, A. G., *Introduction to Structural Dynamics and Aeroelasticity*, Cambridge University Press, New York, NY, 2011.

[77] Patil, M. J. and Hodges, D. H., "Incorrectness of the k Method for Flutter Calculations," *Journal of Aircraft*, Vol. 41, (2), 2004, pp. 402–405.

[78] McVicar, J., DeLong, C., and Gutschmidt, S., "Flutter Dynamics of a Biplane: A Mathematical Model," 2012 World Conference on Advances in Civil, Environmental, and Materials Research, Seoul, South Korea, August 2012.

[79] Pons, A. and Gutschmidt, S., "Lower-wing structural dynamics and flutter in V-strut biplanes," 17th U.S. National Congress on Theoretical and Applied Mechanics, Lansing, MI, June 2014.

[80] Bauchau, O. A., , and Craig, J. I., *Structural Analysis*, Springer, New York, NY, 2009.

[81] Hess, J. and Smith, A. M. O., "Calculation of Non-Lifting Potential Flow About Arbitrary Three-Dimensional Bodies," Technical Report E.S. 40622, March 1962.

[82] Katz, J. and Plotkin, A., *Low Speed Aerodynamics*, Cambridge University Press, New York, NY, 2001.

[83] Carmichael, R. L. and Erickson, L. L., "PAN AIR–A Higher Order Panel Method for Predicting Subsonic or Supersonic Linear Potential Flows about Arbitrary Configurations," Technical Report AIAA Paper 81-1255, June 1981.

[84] Bristow, D. R. and Hawk, J. D., "Subsonic Panel Method for Designing Wing Surfaces from Pressure Distribution," Technical Report NASA CR-3713, 1983.

[85] Morino, L., "Steady, Oscillatory, and Unsteady Subsonic and Supersonic Aerodynamics—Production Version (SOUSSA-P.I,1)," Technical Report NASA CR-159130, 1980.

[86] Drela, M., *XFOIL: An Analysis and Design System for Low Reynolds Number Airfoils*, Springer Berlin Heidelberg, Berlin, Heidelberg, 1989, pp. 1–12. doi: 10.1007/978-3-642-84010-4˙1

[87] Kinnas, S. A. and Hsin, C.-Y., "Boundary Element Method for the Analysis of the Unsteady Flow Around Extreme Propeller Geometries," *AIAA Journal*, Vol. 30, (3), March 1992, pp. 688–696.

[88] Han, J., Kong, D., Song, I., and Lee, C., "Analysis of the cavitating flow around the horn-type rudder in the race of a propeller," Fourth International Symposium on Cavitation, California, United States of America, 2001.

[89] Liu, P., Bose, N., and Colbourne, B., "A Broyden Numerical Kutta Condition for an Unsteady Panel Method," *International Shipbuilding Progress*, Vol. 49, (4), January 2002, pp. 263–273.

[90] He, L. and Kinnas, S. A., "Numerical simulation of unsteady propeller/rudder interaction," *International Journal of Naval Architecture and Ocean Engineering*, 2017.

[91] Tarafder, M. S., Saha, G. K., and Mehedi, S. T., "Analysis of Potential Flow around 3-Dimensional Hydrofoils by Combined Source and Dipole Based Panel Method," *Journal of Marine Science and Technology*, Vol. 18, (3), 2010, pp. 376–384.

[92] Newman, J. N., "Distributions of sources and normal dipoles over a quadrilateral panel," *Journal of Engineering Mathematics*, Vol. 20, 1986, pp. 113–126.

[93] Morino, L. and Kuot, C.-C., "Subsonic Potential Aerodynamics for Complex Configurations: A General Theory," *AIAA Journal*, Vol. 12, (2), February 1974, pp. 191–197.

[94] Ashby, D., "Potential Flow Theory and Operation Guide for the Panel Code PMARC_14," NASA TM 209582, 1999.

[95] Willis, D., *An Unsteady, Accelerated, High Order Panel Method with Vortex Particle Wakes*, Ph.D. thesis, Dept. of Aeronautics and Astronautics, Massachusetts Institute of Technology, 2006.

[96] Gaggero, S. and Brizzolara, S., "Exact Modeling of Trailing Vorticity in Panel Method for Marine Propeller," 2nd International Conference on Marine Research and Transportation, Ischia, Naples, Italy, June 2007.

[97] Burden, R. and Faires, J. D., *Numerical Analysis*, Brooks/Cole, Cengage Learning, 9th edition, 2011.

[98] Govindarajan, B., *Contributions Toward Understanding the Effects of Rotor and Airframe Configurations on Brownout Dust Clouds*, Ph.D. thesis, Dept. of Aero. Eng., University of Maryland, 2014.

[99] Yang, K., *Aerodynamic Analysis of an MAV-Scale Cycloidal Rotor System Using a Structure Overset RANS Solver*, Master's thesis, University of Maryland, College Park, Maryland, 2010.

[100] Rieper, F., "A Low-Mach Number Fix for Roe's Approximate Riemann Solver," *Journal of Computational Physics*, 2011.

[101] Srinivasan, G. R. and Baeder, J. D., "TURNS: A Free-Wake Euler/Navier-Stokes Numerical Method for Helicopter Rotors," *AIAA Journal*, Vol. 31, (5), 1993, pp. 959–962.

[102] Vinokur, M., "On One-Dimensional Stretching Functions for Finite Difference Calculations," NASA CR 3133, 1980.

[103] Leishman, J. G., "Two-Dimensional Model for Airfoil Unsteady Drag Below Stall," *Journal of Aircraft*, Vol. 25, (7), July 1988, pp. 665–666.

[104] "StarkLite 200: Three Sensor Stabilized Electro-Optic Micro Payload," https://starkaerospace.com/wp-content/uploads/2015/09/StarkLite.pdf.

[105] "UIUC Airfoil Coordinates Database," http://m-selig.ae.illinois.edu/ads/coord˙database.html.

[106] "XFLR5," http://www.xflr5.com/xflr5.htm.

[107] Fritsch, F. N. and Carlson, R. E., "Monotone Piecewise Cubic Interpolation," *Society for Industrial and Applied Mathematics*, Vol. 17, (2), 1980, pp. 238–246.

[108] Aràndiga, F., "On the Order of Nonuniform Monotone Cubic Hermite Interpolants," *Society for Industrial and Applied Mathematics*, Vol. 51, (5), 2013, pp. 2613–2633.

[109] "FAI Record ID 17302," http://www.fai.org/fai-record-file/?recordId=17302, 2014.

[110] "2105 Logo 600 SE V2," http://shop.mikadousa.com/02105-LOGO-600-SE-V2_p_1501.html.

[111] "Maryland Wind Resource Map and Potential Wind Capacity," https://apps2.eere.energy.gov/wind/windexchange/wind˙resource˙maps.asp?stateab=md, 2010.